

First Chile-Korea-Gemini Workshop on Stellar Astrophysics

**Accretion Processes in Symbiotic Stars and
Related Objects**

La Serena, Chile, December 4-7, 2016

Edited by Hee-Won Lee
Department of Physics and Astronomy, Sejong University

Conference Program

Invited Talks

1

- 3 On the Mass Transfer and Accretion in Symbiotic Binaries
Augustin Skopal
- 15 Raman O VI Spectroscopy and Polarimetry of Asymmetric Accretion Flows in Symbiotic Stars
Hee-Won Lee
- 27 Circumstellar Spirals/Shells/Arcs: the Message from Binary Stars
Hyosun Kim
- 37 Jets and Other Signs of Accretion in Planetary Nebulae
Romano L.M. Corradi
- 47 GHOST: The Gemini High- Resolution Optical Spectrograph
Steve J. Margheim

Oral Session

49

- 51 The Accretion Column of AE Aqr
Claudia V. Rodrigues, Karleyne M. G. Silva, G. Juan M. Luna, Jaziel G. Coelho, Isabel J. Lima, Joaquim E. R. Costa, & J. Carlos N. de Araujo
- 57 Raman O VI Profile Analysis of Accretion and Bipolar Outflows in Sanduleak's Star
Jeong-Eun Heo, Rodolfo Angeloni, Francesco Di Mille, Tali Palma, & Hee-Won Lee
- 65 Hunting Stellar-mass Black Holes in X-ray Binaries
Jesús M. Corral-Santana
- 71 Investigating Scattering Processes in the Symbiotic Nova V1016 Cyg
Matej Sekeráš, & Augustin Skopal
- 77 Properties of the Wind Outflow from the Cool Components in Symbiotic Binaries
Natalia Shagatova, & Augustin Skopal
- 83 Reclassifying Symbiotic Stars with 2MASS and WISE: An Atlas of Spectral Energy Distribution
Akras Stavros, Guzman-Ramirez Lizette, Leal-Ferreira Marcelo & Ramos-Larios Gerardo
- 89 Accretion in Young and Evolved stars
W.J. de Wit, A. Caratti o Garatti, & S. Kraus

Poster Session

95

- 97 SDSS J122339.61-005631.1: a Short Period Eclipsing Binary with a White Dwarf Component
Saker, L., Lovos, F., Petrucci, R.P., Jofré, J.E., & Gómez, M.
- 103 OVI 6830Å Imaging Polarimetry of Symbiotic Stars
Akras Stavros
- 107 Flux Ratios of Raman Scattered O VI Features in Symbiotic Stars
Young-Min Lee, & Hee-Won Lee
- 115 Polarization of far UV Radiation near Ly α Rayleigh Scattered in Active Galactic Nuclei
Seok-Jun Chang, & Hee-Won Lee

Participant List

119

Preface

Mass loss is the single most important process that characterizes the late stage of stellar evolution. Being wide binary systems of a hot white dwarf and a mass losing giant, symbiotic stars are ideal objects to study the mass loss process and also provide a rare opportunity to investigate the mass transfer process through gravitational capture of a slow stellar wind. Unique spectral features are known in symbiotic stars and related objects, which are formed through Raman scattering by atomic hydrogen. These Raman features with broad and multiple peak profiles can be used to probe the geometry and the kinematics of the thick neutral region vividly revealing the mass loss and transfer processes.

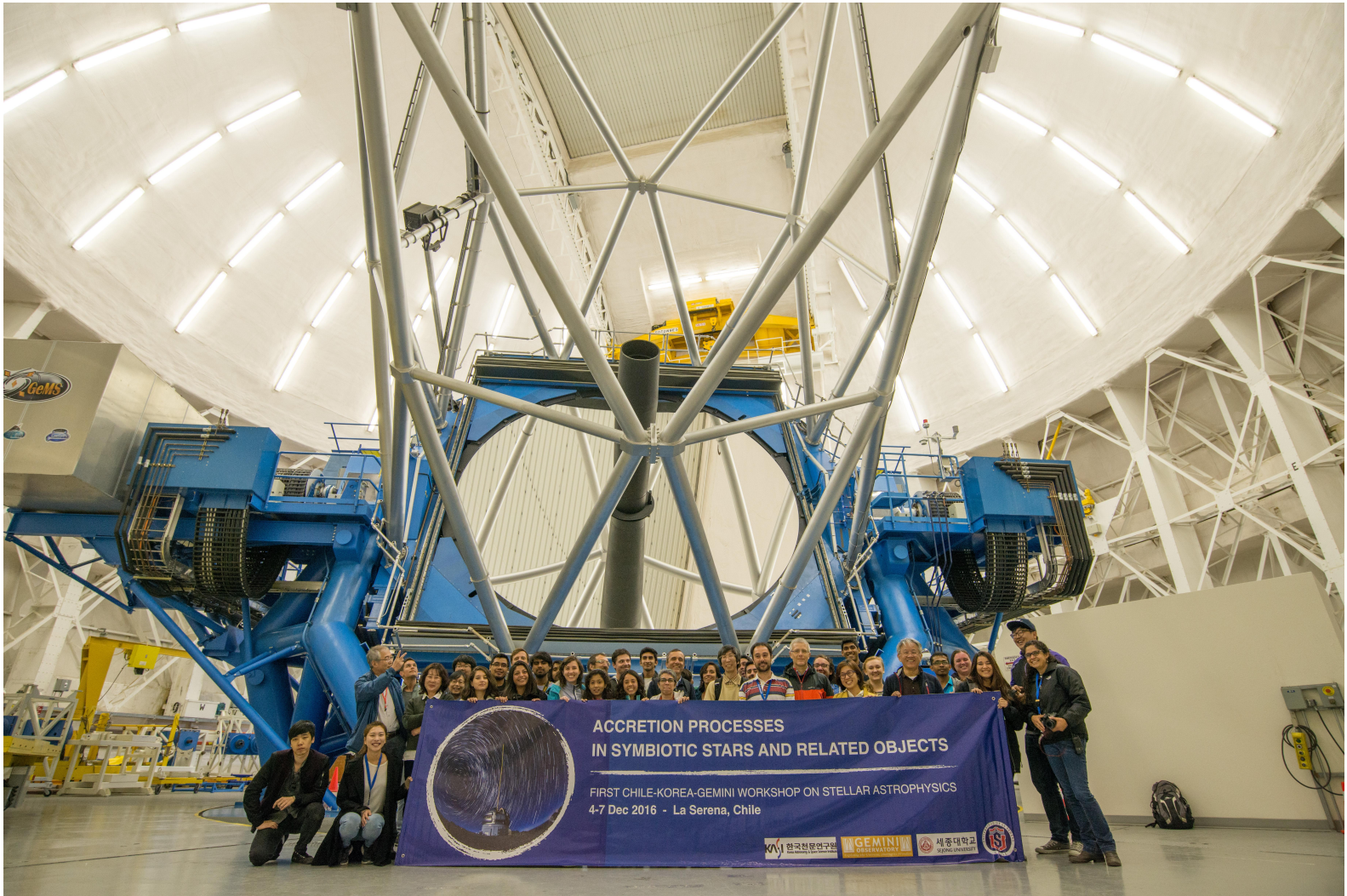
This workshop has been organized to discuss various research activities on symbiotic stars and related objects, encompassing both theoretical and observational studies. The advent of 30-m class telescopes will open a new window showing a totally unexpected universe and forcing us to focus on more fundamental astrophysical principles that interconnect the variety of observed phenomena. In particular, G-Clef, one of the first generation instruments for GMT, will lead us to a new world of high resolution spectroscopy. Korean and Chilean astronomers are seeking close collaboration despite their maximal physical distances on Earth. This workshop will be one aspect toward strengthening such collaborative relation between the two communities. With this workshop it is sincerely hoped that symbiotic stars and related objects will draw significant attention appropriate for their importance in astronomy.

Science Organizing Committee

Rodolfo Angeloni (Chair, Gemini Observatory, University of La Serena, Chile)
Hee-Won Lee (Co-Chair, Sejong University, Korea)
Tali Palma (UNAB, Chile)
Rodolfo Barba (University of La Serena, Chile)

Local Organizing Committee

John Michael Plaza (Chair, Gemini Obs.)
Veronica Firpo (ULS & Gemini Obs.)
Jeong-Eun Heo (Sejong Univ. & Gemini Obs.)
Lucia Medina (Gemini Obs.)
Erich Wenderoth (ULS)
Manuel Paredes (Gemini Obs.)
Amelia Ramírez (ULS)



Invited Talks

On the Mass Transfer and Accretion in Symbiotic Binaries

Augustin Skopal

Astronomical Institute of the Slovak Academy of Sciences,
059 60 Tatranská Lomnica, Slovakia

This contribution is focused to the principal interaction between the binary components of symbiotic stars - the mass transfer via the wind, which is responsible for the appearance of the symbiotic phenomenon. I will briefly introduce the way how to estimate the mass-loss rate from the giant, and point the long-standing problem between the high luminosity of the burning white dwarf and its deficient fueling by the giant in the canonical Bondi-Hoyle accretion mechanism. Possible solution of this mass-transfer problem by focusing the wind from the giant towards the orbital plane will be discussed.

Key Words: symbiotic stars - mass loss - mass transfer - accretion

1 Introduction

Symbiotic stars are the widest interacting binaries, whose orbital periods are typically between 1 and 3 years, but can be significantly larger. They consist of a red giant (RG) as the donor and a white dwarf (WD) as the accretor. Based on a strong correlation between the spectral type of the cool giant and the orbital period, Mürset & Schmid (1999) suggested that symbiotic stars are well detached binary systems. Thus the symbiotic activity on the WD companion is triggered via the wind mass transfer.

There are two principal processes of interaction that are responsible for appearance of the symbiotic phenomenon: (i) Mass loss from the RG in the form of a wind, and (ii) accretion of its fraction by the compact companion. The accretion process heats up the WD to $> 10^5$ K and increases its luminosity to $\sim 10^1 - 10^4 L_{\odot}$, which by return ionizes a portion of the neutral wind from the giant giving rise to the nebular emission. As a result the spectrum of symbiotic stars consists of three basic components of radiation – two stellar from the binary components and one nebular. The simplest ionization model of this composition for a stationary binary, spherically-symmetric wind from the giant with a constant velocity consisting of hydrogen was suggested by Seaquist et al. (1984) (hereafter STB). Individual components of radiation can be obtained by disentangling the measured spectrum (see Skopal, 2005, in detail). Figure 1 shows example of the spectral energy distribution (SED)

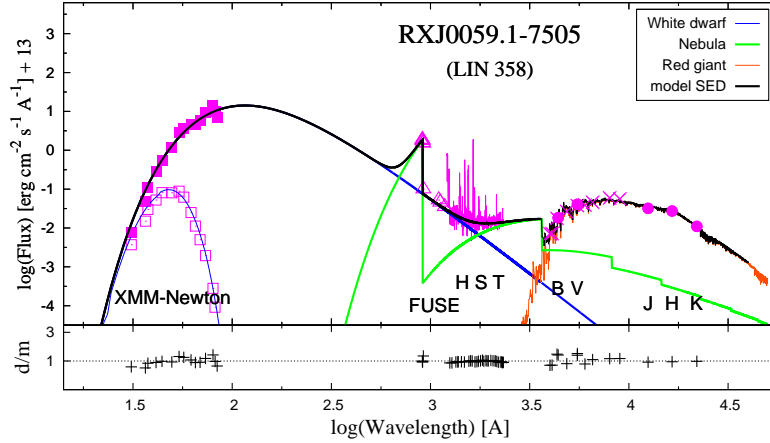


Figure 1: Basic components of radiation in the continuum (see the legend) of the symbiotic binary RX J0059.1-7505 (LIN 358). Solid black line represents their superposition. Bottom panel shows the corresponding data-to-model ratios (d/m). Observations are plotted in magenta. Open and filled squares are the measured and unabsorbed X-ray fluxes (adapted from Skopal, 2015).

for the symbiotic binary RX J0059.1-7505 (LIN 358) in the SMC, whose supersoft X-rays to near-IR spectrum can be disentangled into the three basic components of radiation. The radiation from the WD is characterized with the temperature $T_h \sim 250 \text{ kK}$ and the luminosity $L_h \sim 10^{38} \text{ erg s}^{-1}$, the nebula is fitted with the electron temperature $T_e \sim 18000 \text{ K}$ and the emission measure $EM \sim 2.4 \times 10^{60} \text{ cm}^{-3}$ and the giant radiates at $T_{\text{eff}} \sim 4000 \text{ K}$ producing the luminosity of $\sim 7300 L_\odot$ for the distance to SMC of 60 kpc (see Skopal, 2015).

On the basis of the infrared SED of symbiotic stars, we distinguish between S-type (Stellar) and D-type (Dusty) symbiotic stars (Webster & Allen, 1975). The former is represented by a stellar type of the IR continuum from a normal giant, whereas the latter contains additional strong emission from the dust produced by a Mira-type variable. Therefore, D-type symbiotic stars are also called as symbiotic Miras.

If the processes of the mass-loss, accretion and ionization are in a mutual equilibrium, then symbiotic system releases its energy approximately at a constant SED. This stage is called as the *quiescent phase*. Once this equilibrium is disturbed, symbiotic system changes its radiation significantly, brightens up in the optical by a few magnitudes and shows signatures of a mass-outflow. We name this stage as the *active phase*.

The energy output from the accretor during quiescent phase can be caused by two different mechanisms. In rare cases, the hot star luminosity of $\sim 10^0 - 10^2 L_\odot$ can be powered solely by the accretion process onto a WD (e.g. EG And and 4 Dra), while in most cases, the observed luminosities of a few times $10^3 L_\odot$ (e.g. Mürset et al., 1991; Skopal, 2005) are believed to be caused by stable hydrogen nuclear burning on the WD surface (e.g.

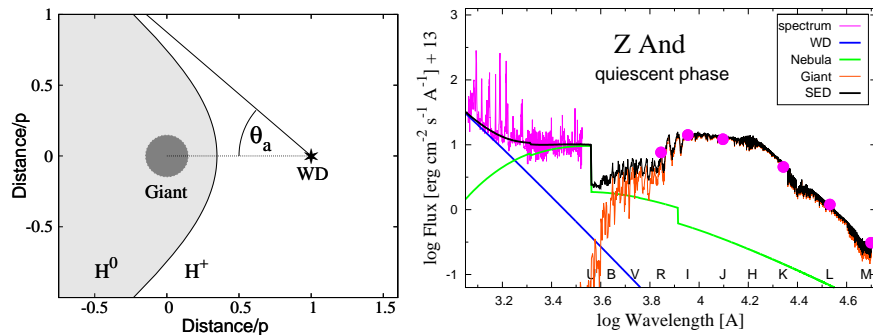


Figure 2: The STB ionization structure (left) and corresponding SED for Z And (right). Extension of the neutral zone is determined by the parameter X or by the asymptotic angle θ_a (see Sects. 2.1 and 2.3). Distances are in units of the binary components separation, p .

Paczynski & Żytkow, 1978; Shen & Bildsten, 2007). The latter requires accretion onto a low mass WD at $10^{-8} - 10^{-7} M_{\odot} \text{yr}^{-1}$. Since the only fuel for this energy is the wind from the RG, we need to know its mass-loss rate and the way how the wind is transferred to the WD and accreted at the required rate. Therefore, first I will introduce principle of methods to estimate the mass-loss rate from RGs in symbiotic stars, \dot{M}_{RG} .

2 Mass-loss rate from RGs in symbiotic stars

Mass-loss rates from giants in symbiotic binaries can be estimated in the context of the STB model. Usually, by measuring the nebular emission, because the nebula during quiescent phase represents the ionized fraction of the wind from the RG. Or, by probing the neutral part of the wind via Raman scattering of a specific line transition that allows us to determine the extent of the neutral part of the wind. In both cases the geometry of the H^0/H^+ interface in the binary is needed to know.

2.1 STB ionization model

Ionization structure of a symbiotic binary within the STB model is given by the H^0/H^+ boundary that is represented by the locus of points at which ionizing photons are completely consumed by neutral atoms of hydrogen along paths outward from the ionizing source. The shape of the boundary is described in the WD-centered polar coordinate system (u, θ) by the parametric equation,

$$f(u, \theta) - X = 0, \quad (1)$$

which solution defines the boundary at the orbital plane. The parameter X is given by the binary properties and the wind parameters, \dot{M}_{RG} and terminal velocity, v_{∞} (see STB). Density distribution is given by the wind

velocity function. For a constant wind ($v = v_\infty$), the function $f(u, \theta)$ can be expressed analytically (STB; Nussbaumer & Vogel, 1987). Figure 2 depicts the STB ionization structure for the so-called β -law wind, $v(r) = v_\infty(1 - R_{\text{RG}}/r)^\beta$ with the accelerating parameter $\beta = 2.5$ and $X = 7$ (left). The shape of the boundary can also be determined by the asymptotic angle θ_a (Sect. 2.3). The right panel shows the corresponding typical UV/near-IR SED for the prototype of symbiotic stars Z And during quiescent phase.

2.2 \dot{M}_{RG} from the ionized part of the wind

Assuming spherically symmetric mass-loss from a star (the ionizing source) ejected at a uniform rate with constant velocity v_∞ , Wright & Barlow (1975) (WB) derived the radio flux density, S_ν , generated by the ionized wind in the form of the bremsstrahlung radiation. Since the measured free-free emission from the ionized wind dominates the radio, i.e., the stellar component of the continuum is negligible here, the authors derived a relation for the mass-loss rate as,

$$\dot{M}_{\text{RG}} = 0.095 \frac{\mu v_\infty S_\nu^{3/4} d^{3/2}}{Z \gamma^{1/2} g^{1/2} \nu^{1/2}} M_\odot \text{yr}^{-1} \quad (2)$$

where μ is the mean atomic weight, v_∞ is in km s^{-1} , S_ν is in Jy, the distance to the star d is in kpc, ν is in Hz, γ is the ratio of the electron number density to the ion number density, g is the Gaunt factor and Z is the atomic number. Equation (2) is valid provided that the radio flux distribution obeys the $S_\nu \propto \nu^{2/3}$ relation.

Measuring the radio emission at 3.6 cm for a sample of 99 symbiotic stars and using the WB formula, Seaquist et al. (1993) estimated mass-loss rates for around 65 stellar type symbiotic stars (see their Table 2). Since the WB formula measures the mass-loss associated with the ionized gas only, its application to symbiotic stars underestimates the true \dot{M}_{RG} , because the giant's wind in symbiotic stars is only partially ionized (see Fig. 2). Therefore, Seaquist et al. (1993) introduced a correction factor $f = \dot{M}_{\text{WB}}/\dot{M}_{\text{RG}}$, i.e. the ratio of the mass-loss rate from the WB relation (2) to the true mass-loss rate, and estimated its values as a function of the parameter X as follows: $f = 0.46, 0.68, 0.80$ and 0.87 for $X = 0.5, 1, 2$ and 5 , respectively. In this way, Seaquist et al. (1993) derived $\dot{M}_{\text{RG}} \approx 10^{-7} M_\odot \text{yr}^{-1}$ for S-type symbiotic stars.

In the UV/optical/near-IR, the nebular emission is produced by free-bound and free-free transitions in thermal plasma of a dense symbiotic nebula (e.g. Brown & Mathews, 1970). Its amount has to be determined by modelling the SED, because other components of radiation cannot be neglected within this region (see Figs. 1 and 2). Amount of the nebular radiation is characterized by the emission measure, EM , that is defined as $\int n_+ n_e dV$ throughout the volume of the fully ionized zone. For number density satisfying spherically symmetric equation of continuity and the β -law

wind with $\beta = 2.5$, the EM can be approximated by (see Skopal, 2005),

$$EM = \frac{-1}{16\pi(\mu m_{\text{H}})^2} \left(\frac{\dot{M}_{\text{RG}}}{v_{\infty}} \right)^2 \frac{1}{R_{\text{RG}}} \left[1 - \left(1 - \frac{R_{\text{RG}}}{Q} \right)^{-4} \right], \quad (3)$$

which corresponds to the upper limit of the EM assuming the sphere around the RG to be fully ionized from $r = Q$ to $r = \infty$. Parameter Q is the location of the H^0/H^+ boundary on the binary axis and the wind starts at the giant's surface $r = R_{\text{RG}}$. Comparing the measured EM from models SED to Eq. (3) for 15 S-type symbiotic stars, Skopal (2005) determined \dot{M}_{RG} to a few $\times 10^{-7} M_{\odot} \text{yr}^{-1}$ for $v_{\infty} = 20 \text{ km s}^{-1}$ and $Q/p \sim 0.3 - 0.4$.

2.3 \dot{M}_{RG} from the neutral part of the wind

\dot{M}_{RG} can also be determined by probing directly the neutral fraction of the RG wind in symbiotic stars. Here, Raman scattering of the far-UV line photons on atomic hydrogen in the wind is investigated. The key parameter is the efficiency of this process, defined as the ratio between the Raman scattered and the original line photons. The Raman scattering efficiency defines the so-called 'covering factor' C_{S} , which represents a fraction of the sky covered by the Raman scattering region for the original line photons. Assuming that the region emitting initial line photons is located near the hot component and the geometry of the H^0 region is given by the STB model, we can express C_{S} via a solid angle Ω , under which the initial line photons can 'see' the scattering region, i.e.,

$$C_{\text{S}} = \frac{\Omega}{4\pi} = \frac{1 - \cos \theta_{\text{R}}}{2}, \quad (4)$$

where θ_{R} is the opening angle of the Raman scattering region. In general, the angle $\theta_{\text{R}} < \theta_{\text{a}}$, (Fig. 2 left), because there is always a fraction of H^0 zone, where the Raman conversion can be neglected (i.e. $\tau_{\text{Ram}} < 1$). Therefore, it is convenient to use Raman conversion with a high cross-section for which $\theta_{\text{R}} \sim \theta_{\text{a}}$ that allows us to determine the parameter X more easily. Example is given by Sekeráš & Skopal (2015), who used the Raman $\text{He II } \lambda 1025 \rightarrow \lambda 6545$ conversion that has cross-section $\sigma_{\text{Ram}} = 8.05 \times 10^{-22} \text{ cm}^2$ (Lee, 2009). Otherwise, one has to reconstruct θ_{a} from θ_{R} taking into account optically thick conditions for the investigated Raman scattering conversion. Finally, having the parameter X from θ_{R} and the fundamental parameters of the hot component, one can derive \dot{M}_{RG} . Using Raman $\text{He II } \lambda 1025 \rightarrow \lambda 6545$ conversion, Sekeráš & Skopal (2015) determined $\dot{M}_{\text{RG}} = 2 - 3 \times 10^{-6} M_{\odot} \text{yr}^{-1}$ for the mira-type variable in V1016 Cyg. These values are in agreement with those inferred by Seaquist et al. (1993) using the radio emission produced by D-type symbiotic stars.

We can conclude this section that \dot{M}_{RG} is in order of 10^{-7} and $10^{-6} M_{\odot} \text{yr}^{-1}$ for S-type and D-type symbiotic stars, respectively.

3 On the mass accretion rate onto the WD

To know the rate of accretion from the RG wind onto the WD, \dot{M}_{acc} , that is required to power its high luminosity, $L_{\text{WD}} \approx 10^3 L_{\odot}$, first, I will briefly introduce how the WD can generate the energy from accretion process.

3.1 Energy output from the accreting WD

In spite that WDs in symbiotic stars accrete from the wind (Sect. 1), a large accretion disk is still formed around the accretor (e.g. Theuns & Jorissen, 1993). The accreted material is thus transported onto the accretor's surface through a disk. As a result the total luminosity of the accreting WD can be generated by two main sources, (i) hydrogen nuclear burning on the WD surface (L_{nuc}), and (ii) gravitational potential energy of the accretor, converted into the radiation by the disk (L_{disk} ; Pringle (1981)), i.e.,

$$L_{\text{WD}} = L_{\text{nuc}} + L_{\text{disk}} = \eta X \dot{M}_{\text{acc}} + \frac{GM_{\text{WD}} \dot{M}_{\text{acc}}}{2R_{\text{WD}}}, \quad (5)$$

where $\eta = 6.3 \times 10^{18}$ erg/g is the energy production of 1 gram of hydrogen due to the nuclear fusion of 4 protons, and $X \equiv 0.7$ is the hydrogen mass fraction in the accreted matter. M_{WD} and R_{WD} are the WD mass and radius. If \dot{M}_{acc} is in the range of the stable H-burning for given M_{WD} then $L_{\text{nuc}} \gg L_{\text{disk}}$. For a typical M_{WD} in symbiotic stars of $\sim 0.6 M_{\odot}$ the stable H-burning arises for \dot{M}_{acc} in the range of a few times 10^{-8} to $\sim 10^{-7} M_{\odot} \text{ yr}^{-1}$ (see Fig. 2 of Shen & Bildsten, 2007). According to Eq. (5) such the high \dot{M}_{acc} generates L_{nuc} of a few times $10^3 L_{\odot}$, whereas L_{disk} is only of a few times $10^1 L_{\odot}$. Thus the observed high L_{WD} of $10^3 L_{\odot}$ or more can be achieved by stable nuclear burning of hydrogen on the WD accreting at the rate nearly of $10^{-7} M_{\odot} \text{ yr}^{-1}$.

Knowing that $\dot{M}_{\text{RG}} \approx 10^{-7} M_{\odot} \text{ yr}^{-1}$ and the required \dot{M}_{acc} is only, to say, of a few times lower, implies a very high mass-transfer efficiency between the binary components in symbiotic stars.

4 On the mass-transfer ratio

4.1 A mass-transfer problem

Pioneering studies on accretion from interstellar material was elaborated by Hoyle & Lyttleton (1939) and Bondi & Hoyle (1944). Livio & Warner (1984) adapted the Bondi-Hoyle picture of accretion to a wide binary system, consisting of a late-type giant emitting a strong stellar wind and a WD accreting matter from the wind. According to this study, typical parameters of S-type symbiotic system yield the mass-transfer ratio ($= \dot{M}_{\text{acc}}/\dot{M}_{\text{RG}}$, i.e., the mass-transfer efficiency) of a few percents. Similar results were obtained by even more sophisticated simulations of wind accretion in well separated binaries. Depending on the binary configuration, the mass-transfer ratio was found to be in the range of 0.6–10% (e.g. Theuns et al., 1996; Walder, 1997; Nagae et al., 2004; Walder et al., 2008; Hadrava & Čechura, 2012).

However, the large energetic output from hot components, which requires accretion in the range of a few times 10^{-8} to $\sim 10^{-7} M_{\odot} \text{ yr}^{-1}$ (Sect. 3.1), and mass-loss rates from RGs of $\approx 10^{-7} M_{\odot} \text{ yr}^{-1}$ (Sect. 2.2) in symbiotic binaries, suggest a more effective mass-transfer mode than can be achieved by a standard Bondi-Hoyle wind accretion. This problem of the wind mass-transfer between the components of symbiotic binaries arose already during 70s and 80s decades of the last century, when the *International Ultraviolet Explorer* confirmed unambiguously the binary nature of these objects and revealed a very high luminosity of majority of their hot components. Kenyon & Gallagher (1983) pointed this problem by the question: ‘How do red giants, well within their Roche lobes, lose sufficient mass to produce the symbiotic phenomenon?’ Recently, a solution of this problem for both, D-type and S-type symbiotic stars, was suggested.

4.2 Wind Roche-lobe overflow

An efficient wind-mass-transfer was suggested for slow and dense winds as are typical for AGB stars. Therefore, it can be applied for Mira-type interacting binaries, i.e., for D-type symbiotic stars. In this mass transfer mode, called wind Roche-lobe overflow (WRLOF, Mohamed & Podsiadlowski, 2007, 2012) or gravitational focusing (de Val-Borro et al., 2009), the wind of the evolved star is filling the Roche lobe ($v_{\text{wind}} < v_{\text{escape}}$) instead the star itself, and thus can be effectively transferred into the potential of the companion via the L_1 point, similarly to standard RLOF. The WRLOF can occur in systems where the acceleration zone of the wind extends to, or is a significant fraction of, the Roche lobe radius (see Fig. 1 of Abate et al., 2013). Then the wind is focused towards the orbital plane and in particular to the WD. Corresponding mass transfer efficiencies are at least an order of magnitude larger than the analogous Bondi-Hoyle values (Mohamed & Podsiadlowski, 2012).

An efficient mass transfer was evidenced also observationally for the symbiotic stars Mira AB (Karovska et al., 2005).

4.3 Focusing by the wind compression model

Skopal & Cariková (2015) suggested that the wind from normal giants in S-type symbiotic stars can be focused by their rotation according to the wind compression disk (WCD) model elaborated by Bjorkman & Cassinelli (1993). This possibility insists on the fact that normal giants in these systems rotate slowly. Zamanov et al. (2007) found a typical rotational velocity of the K and M giants in S-type symbiotic stars to be $4.5 < v_{\text{rot}} \sin(i) < 11.7 \text{ km s}^{-1}$. Applicability of the model to such slowly rotating giants was justified by Cariková & Skopal (2014). To demonstrate focusing of the giant’s wind to the equatorial plane due to its rotation, Skopal & Cariková (2015) introduced the mass-loss ratio,

$$f(r, \theta) = \frac{\dot{M}^c(r, \theta)}{\dot{M}_{\text{RG}}} = \frac{\rho^c(r, \theta)}{\rho(r)}, \quad (6)$$

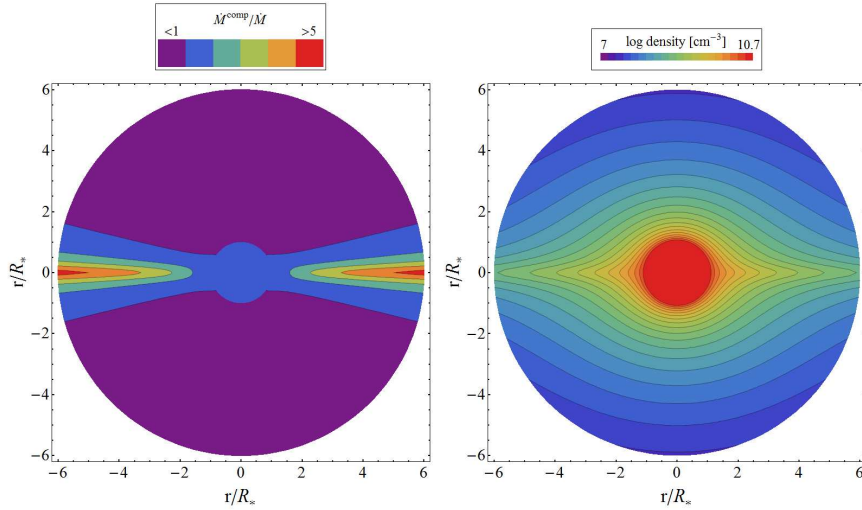


Figure 3: Focusing of the wind to the equatorial plane according to the wind compression model. Left panel shows the mass-loss ratio $f(r, \theta)$ for $r < 6 R_{\text{RG}}$ and all θ (Eq. (6)). Right panel depicts the corresponding density distribution. Both calculated according to the WCD model for giant’s rotation of 6 km s^{-1} , wind terminal velocity of 20 km s^{-1} , $\dot{M}_{\text{RG}} = 10^{-7} M_{\odot} \text{ yr}^{-1}$ and $R_{\text{RG}} = 100 R_{\odot}$ (see Skopal & Cariková, 2015).

where $\dot{M}^c(r, \theta)$ is the spherical equivalent of the mass-loss rate calculated from the local density $\rho^c(r, \theta)$ given by the WCD model and $\rho(r)$ is the mass density distribution of spherically symmetric wind. Figure 3 shows example of the parameter f and the corresponding density distribution for the distance $r < 6 R_{\text{RG}}$. Compression of the wind to the equatorial plane is fairly significant: $f > 1$ for $\theta > 75^\circ$ and $f \sim 5 - 10$ for $\theta = 90^\circ$ at $r = 5 - 6 R_{\text{RG}}$. This suggests a relevant increase of the accretion rate,

$$\dot{M}_{\text{acc}} \approx f \times \xi \times \dot{M}_{\text{RG}}, \quad (7)$$

where $f \sim 5 - 10$ and ξ is the mass transfer ratio of a few times 0.01 for spherically symmetric wind in the canonical Bondi-Hoyle accretion regime (Sect. 4.1). Thus, $\dot{M}_{\text{RG}} = \text{a few} \times 10^{-7} M_{\odot} \text{ yr}^{-1}$ yields $\dot{M}_{\text{acc}} \sim 10^{-8} - 10^{-7} M_{\odot} \text{ yr}^{-1}$, which is sufficient to power the observed WD luminosity by a stable hydrogen-burning for $M_{\text{WD}} < 1 M_{\odot}$ (Sect. 1 and 3.1).

4.4 Indication of the wind focusing

A wind-focusing effect was constrained by observations for the symbiotic star SS Lep in an effort to explain the abnormal luminosity of its accretor. Using the data obtained with the VLTI instruments AMBER and PIONIER in the H and K bands, Blind et al. (2011) learned that the mass-transfer ratio in SS Lep is expected to be much higher than 10%, perhaps in the

range of 80–90%. Having indication of an accretion disk, they explained the required high accretion rate in the WRLOF scenario, because most of the matter goes through the L_1 point (Sect. 4.2).

Modelling the observed column densities of hydrogen around the RGs in the eclipsing S-type symbiotic binaries EG And and SY Mus, Shagatova et al. (2016) suggested that the wind from their RGs is enhanced at the orbital plane. Their analysis revealed that the spherical equivalent of the mass-loss rate from the giants is a factor of > 10 higher than rates determined by methods that do not depend on the line of sight. As the mass-loss rates were derived from near-orbital-plane column densities (eclipsing binaries), the corresponding high spherical equivalents of the mass-loss rates can be a result of focusing the wind towards the binary orbital plane.

5 Summary and concluding remarks

The mass-transfer via the wind in symbiotic binaries represents the fundamental process that is responsible for the observed symbiotic phenomenon. The stellar wind from RGs is the only fuel feeding hot companions – the luminous WDs. Current methods suggest that the mass-loss rates from RGs in symbiotic stars are in the order of 10^{-7} and $10^{-6} M_{\odot} \text{yr}^{-1}$ for S-type and D-type systems, respectively (Sect. 2). The high luminosities of nuclear burning WDs require an efficient wind mass-transfer mode (Sect. 4.1). For D-type symbiotic stars, the WRLOF mode can be considered (Sect. 4.2), whereas for S-type systems, focusing by the WCD model can be in the effect (Sect. 4.3).

However, the above mentioned suggestions on how the wind can be effectively transferred from the RG to its WD companion, being focused to the binary orbital plane, represent simple ways on how to get enough wind from the RG to the vicinity of the WD in symbiotic binaries. Therefore, more sophisticated calculations together with mainly interferometric observations of a high precision are needed to improve our current knowledge on the mass-transfer and accretion in symbiotic stars. In this respect, the recent launch of the ESA GAIA satellite offers great prospects (see Boffin et al., 2014, and references therein). To obtain more information on the mass-transfer in mainly S-type symbiotics, it is needed to include the idea of the WCD model into 3-D hydrodynamic models (e.g., as cited in Sect. 1) to find out the structure of the wind from the rotating giant in these systems and to understand the process of its accretion. From this point of view, the approach to solving the problem of a high wind mass transfer efficiency in S-type symbiotic binaries (Sect. 4.3) represents a direction for future theoretical modelling.

Acknowledgements The author acknowledges the conference organizers for facilitating my attendance at such a splendid meeting. This research was supported by a grant of the Slovak Academy of Sciences, VEGA No. 2/0008/17 and by the Slovak Research and Development Agency under the contract No. APVV-15-0458.

References

- Abate, C., Pols, O. R., Izzard, R. G., Mohamed, S. S., & de Mink, S. E. 2013, *A&A* 552, A26
- Bjorkman, J. E., Cassinelli, J.P. 1993, *ApJ*, 409, 429
- Blind, N., Boffin, H. M. J., Berger, J.-P., et al. 2011, *A&A*, 536, A55
- Boffin, H. M. J., Hillen, M., Berger, J. P. et al. 2014, *A&A*, 564, A1
- Bondi, H., & Hoyle, F. 1944, *MNRAS*, 114, 195
- Brown, R. L., & Mathews, W. G. 1970, *ApJ*, 160, 939
- Cariková, Z., Skopal, A. 2014, *A&A*, 570, A4
- de Val-Borro, M., Karovska, M., & Sasselov, D. 2009, *ApJ*, 700, 1148
- Hadrava, P., & Čechura, J. 2012, *A&A*, 542, A42
- Hoyle, H., & Lyttleton, R. A. 1939, *Proc. Cam. Phil. Soc.*, 35, 405
- Karovska, M., Schlegel, E., Hack, W., Raymond, J. C., & Wood, B. E. 2005, *ApJ*, 623, L137
- Kenyon, S. J., & Gallagher, J. S. 1983, *AJ*, 88, 666
- Lee, H-W., 2009, *MNRAS*, 400, 2153
- Livio, M., & Warner, B. 1984, *The Observatory*, 104, 152
- Mohamed, S., & Podsiadlowski, Ph. 2007, in 15th European Workshop on White Dwarfs, R. Napiwotzki and Burleigh M. R. eds., *ASP Conf. Ser.* Vol. 372, p. 397
- Mohamed, S., & Podsiadlowski, Ph. 2012, *Baltic Astronomy* 21, 88
- Mürset, U., Nussbaumer, H., Schmid, H. M., & Vogel, M. 1991, *A&A* 248, 458
- Mürset, U., & Schmid, H. M. 1999, *A&AS*, 137, 473
- Nagae, T., Oka, K., Matsuda, T., Fujiwara, H., Hachisu, I., & Boffin, H. M. J. 2004, *A&A*, 419, 335
- Nussbaumer, H., & Vogel, M., 1987, *A&A*, 182, 51
- Paczynski B., & Żytkow, A. N. 1978, *ApJ*, 222, 604
- Pringle, J. E. 1981, *Ann. Rev. Astron. Astrophys.*, 19, 137
- Seaquist, E. R., Taylor, A. R. & Button, S. 1984, *ApJ*, 284, 202 (STB)
- Seaquist, E.R., Krogulec, M., & Taylor, A.R. 1993, *ApJ*, 410, 260

- Sekeráš, M., & Skopal, A. 2015, ApJ, 812, 162
- Shagatova, N., Skopal, A., Cariková, Z. 2016, A&A, 588, A83
- Shen, K. J., & Bildsten, L. 2007, ApJ, 660, 1444
- Skopal, A.: 2005, A&A, 440, 995
- Skopal, A. 2015, New Astron., 36, 116
- Skopal, A., & Cariková, Z. 2015, A&A, 573, A8
- Theuns, T., & Jorissen, A. 1993, MNRAS, 265, 946
- Theuns, T., Boffin, H. M. J., & Jorissen, A. 1996, MNRAS, 280, 1264
- Walder, R. 1997, in Accretion phenomena and related outflows, ed. D. T. Wichramasinghe, L. Ferrario, & G. V. Bicknell, IAU Coll., 163, ASP Conf. Ser., 121, 822
- Walder, R., Folini, D., & Shore, S. N. 2008, A&A, 484, L9
- Webster, B. L. & Allen, D. A. 1975, MNRAS, 171, 171
- Wright, A. E. & Barlow, M. J. 1975, ApJ, 170, 41 (WB)
- Zamanov, R. K., Bode, M. F., Melo, C. H. F. et al. 2007, MNRAS, 380, 1053

Raman O VI Spectroscopy and Polarimetry of Asymmetric Accretion Flows in Symbiotic Stars

Hee-Won Lee

Department of Physics and Astronomy, Sejong University,
Seoul, Korea
hwlee@sejong.ac.kr

Being binary systems of a mass losing giant and a hot white dwarf, symbiotic stars are unique objects to exhibit various activities linked to the accretion of some fraction of the slow stellar wind from the giant companion. About a half of symbiotic stars are known to exhibit broad emission features at 6825 and 7082 formed through inelastic or Raman scattering of far UV O VI 1032 and 1038 with atomic hydrogen. In this presentation, we point out that the flux ratio F_{6825}/F_{7082} is a good indicator of the representative HI column density around the giant component. The slow stellar wind accretion around the white dwarf is expected to be asymmetric where the entering side is denser than the opposite side, resulting in red-enhanced Raman OVI profile. Furthermore, the density inhomogeneity leads to higher ratio of blue peak to red peak for Raman 7082 than for Raman 6825. Polarization flip often observed in the red wing in Raman OVI is consistent with the bipolar flow structure, where an additional OVI emission component or an HI region is receding from the accretion disk around the white dwarf. In this respect high resolution spectroscopy and polarimetry of Raman scattered O VI features can be a highly useful tool to probe the mass transfer processes that take place in symbiotic stars.

Key Words: symbiotic star - radiative transfer - line profile - polarization - accretion - mass loss

1 Introduction

Accreting white dwarfs are found in cataclysmic variables and symbiotic stars, where the mass donor is a red dwarf filling its Roche lobe in the former case and a mass-losing evolved giant in the latter case. CVs are known to form a geometrically thin and optically thick accretion disk around the white dwarf from the Roche lobe overflow. As opposed to CVs, mass accretion in symbiotic stars appears more complicated and our understanding is less

clearly established. Fig.1 shows a schematic illustration of wind accretion in symbiotic stars.

Symbiotic stars are classified into ‘S’ type and ‘D’ type depending on the presence of IR excess. D type symbiotic stars exhibit clear IR excess attributed to a warm dust component with temperature $\sim 10^3$ K, whereas no such component is present in stellar or ‘S’ type symbiotics. The dust component in D type symbiotics appears to be related with the fact that the giant component is mostly a Mira type variable. The orbital periods of S type symbiotics are found in the range of several years whereas those for D type symbiotics are poorly constrained and appear to exceed several decades.

Various activities associated with symbiotic stars may be attributed to accretion onto a white dwarf component through gravitational capture of a fraction of slow stellar wind from the giant component. A typical mass accretion rate may range between $10^{-8} - 10^{-7} M_{\odot}\text{yr}^{-1}$, which is, in turn, about 10 percent of the mass lost by the cool component. One excellent and unique probe is provided by Raman scattered O VI features at 6825 Å and 7082 Å identified by Schmid (1989) who proposed that these are formed through inelastic scattering of far UV O VI 1032 and 1038 photons with a hydrogen atom in the ground state finally de-excite to the excited $2s$ state.

These Raman scattered O VI features are found so far exclusively in symbiotic stars. They exhibit complicated multiple peak profiles and strongly linearly polarized. The profiles are asymmetric, where the red peak is often stronger than the blue counterpart. Furthermore, the profiles of Raman OVI 6825 and 7082 features differ in such a way that the blue peak of the 6825 feature is relatively more suppressed than that of the 7082 feature when the red peaks are normalized to be of the same strength. Invoking the asymmetry in the accretion flow around the white dwarf, the asymmetric profiles and disparity in the two profiles can be understood (e.g., Lee & Park, 1999).

Without being mixed with the unpolarized emission component, Raman scattered O VI features exhibit strong linear polarization. One particularly notable phenomenon is that the polarization direction in the red wing part is often perpendicular to that along which the blue and central parts are polarized. If the blue and central parts are formed in an accretion flow, then the red wing part polarized in the opposite direction can be formed in a component moving away from the accretion disk in the bipolar directions.

2 Cross Section and Branching Ratio

The scattering process of a photon with an atomic electron is described by the time-dependent second order perturbation theory, where the electron initially in the state $|i\rangle$ makes a transition to a final state $|f\rangle$ via an intermediate state $|I\rangle$ and accordingly the incident photon is annihilated and a new outgoing photon is created. In the case where the initial and final electron states are the same, then the incident and outgoing photons are of

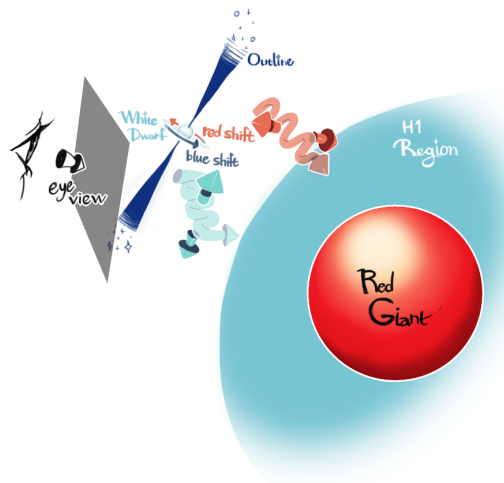


Figure 1: A cartoonistic illustration for Raman OVI line formation in symbiotic stars.

the same energy, which we call Rayleigh scattering. If the electron's final state differs from its initial state, then the scattered photon has a frequency different from that of the incident photon. This inelastic scattering is called Raman scattering,

The cross section is obtained by summing contributions from all the possible intermediate states $|I\rangle$. In the electric dipole interaction case for which the interaction Hamiltonian is proportional to the electric dipole operator $\vec{d} = e\vec{r}$. Non-zero contribution is made by all p states if the electron of a hydrogen atom is in the ground state $1s$, because the interaction Hamiltonian is a rank-1 tensor operator linking two states differing by unit angular momentum \hbar , which is none other than the selection rule for E-1 transitions. Relevant matrix elements that enter in the computation of the scattering cross section include

$$M_{fI,1} = \frac{\langle f|\hat{p}|I\rangle\langle I|\hat{p}|1s\rangle}{\omega - \omega_I}, \quad M_{fI,2} = \frac{\langle f|\hat{p}|I\rangle\langle I|\hat{p}|1s\rangle}{\omega + \omega_I}, \quad (1)$$

where \hat{p} is the momentum operator. The first matrix element is associated with the process of annihilation of the incident photon and excitation into I followed by creation of an outgoing photon and de-excitation into $|f\rangle$. The second matrix element delineates the process of creation of an outgoing photon and excitation into I followed by annihilation of the incident photon and de-excitation into $|f\rangle$. These two processes appear to break the energy conservation law in classical physics. However, in fact the uncertainty principle $\Delta E\Delta t > \hbar$ is respected by these processes, because no measurement is performed which intermediate state is excited during the interaction. The denominator in $M_{fI,1}$ shows that resonance behavior is expected when

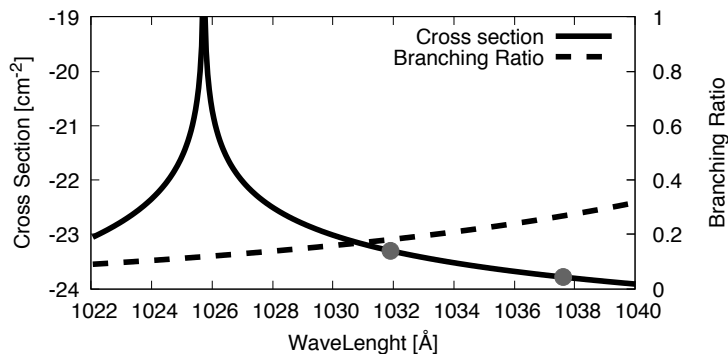


Figure 2: Cross section of total scattering (Rayleigh + Raman) and branching ratio into $2s$ state.

$\omega \simeq \omega_I$ with $I = |np\rangle$ for some n . In this case, the $|np\rangle$ contribution simply dominates so that the cross section is well approximated by a Lorentzian function. Here, ω_I is regarded as a complex quantity where the imaginary part corresponds to the uncertainty of the energy level of I leading to decay or radiation damping.

The cross sections for Rayleigh and Raman scattering are provided from the Kramers-Heisenberg formula. The total scattering cross section and the branching ratio into $2s$ state are shown in Fig. 2. According to Lee & Lee (1997), the cross sections for O VI 1032 and 1038 are

$$\begin{aligned} \sigma_{tot,1032} &= 41.5\sigma_T, & \sigma_{Ram,1032} &= 7.5\sigma_T, \\ \sigma_{tot,1038} &= 9.1\sigma_T, & \sigma_{Ram,1038} &= 2.5\sigma_T, \end{aligned} \quad (2)$$

where $\sigma_T = 0.665 \times 10^{-23} \text{ cm}^2$ is the Thomson scattering cross section. This suggests that one essential requirement for formation of Raman O VI is the presence of a thick H I region with $N_{HI} \geq 10^{22} \text{ cm}^{-2}$ illuminated by an intense far OVI emitting source. This condition is hardly met in other celestial objects than symbiotic stars. Recently Dopita et al. (2016) reported their discovery of Raman scattering involving O I and Si II lines in H II regions including the Orion Nebula (M42) and other H II regions in the Large and Small Magellanic Clouds.

3 Flux Ratios and Representative H I Column Density

The first fundamental properties of Raman O VI features may include their Raman conversion efficiency, which is defined as the ratio of numbers of injected far UV OVI photons and emergent Raman optical photons. The representative H I column density along a line of sight from the white dwarf

toward the H I region formed by material lost as a result of mass loss from the giant is written as

$$N_{HI} \simeq n_{HI,c} R_{HI} \quad (3)$$

where $n_{HI,c}$ and R_{HI} are representative H I number density and size of the H I region. Considering that the line of sight from the white dwarf is characterized by the impact parameter made by the giant, we may set the representative quantities as those measured at positions of impact, or the nearest position on the line of sight with respect to the giant. The amount of H I depends on the mass loss rate

$$\dot{M} = 4\pi r^2 \mu m_H n_H v_r. \quad (4)$$

Since a sizable Raman flux requires a non-negligible covering factor of the H I region with respect to the white dwarf, the impact parameter b should be comparable to the binary separation a of the hot and cool components. Furthermore, the wind velocity v_r at a radial distance r from the cool component is approximated by the wind terminal velocity v_∞ , which is, in turn, of order $\simeq 10 \text{ km s}^{-1}$. Using these values a representative H I column density can be written in terms of the mass loss rate and binary separation as

$$N_{HI} \simeq 3 \times 10^{21} \text{ cm}^{-2} \left(\frac{\dot{M}}{10^{-7} \text{ M}_\odot \text{ yr}^{-1}} \right) \left(\frac{10^{14} \text{ cm}}{a} \right) \left(\frac{10 \text{ km s}^{-1}}{v_\infty} \right). \quad (5)$$

The H I column density increases as the impact parameter b decreases so that Rayleigh-Raman scattering optical depth is very high as the line of sight grazes the giant surface.

We note that the total scattering optical depth of unity for O VI 1038 is achieved for $N_{HI} \simeq 1.6 \times 10^{22} \text{ cm}^{-2}$, at which the scattering optical depth for O VI 1032 is about 4.5. In the case where the scattering H I region is characterized by a H I column density $N_{HI} < 10^{22} \text{ cm}^{-2}$, O VI doublet line photons are optically thin. Most Raman optical photons are formed through single scattering, which results in the Raman conversion efficiency determined by the Raman scattering cross section. Under the assumption that the same number of O VI 1032 and 1038 photons are injected to a scattering region with $N_{HI} < 10^{22} \text{ cm}^{-2}$ we get a high value of $F_{6825}/F_{7082} \sim 3$.

In the opposite case of $N_{HI} > 10^{23} \text{ cm}^{-2}$, the scattering optical depth exceeds 6 for O VI 1038 photons, so that escape is made through Raman conversion as optical photons. Complete Raman conversion is achieved when the scattering region fully covers the O VI emission region, in which case the resultant flux ratio of $F_{6825}/F_{7082} = 1$. Because no far UV photons escape, the number of Rayleigh scatterings is set by the branching ratio into the Raman channels.

When the O VI emission region is partially covered by the neutral scattering region, then Rayleigh reflection becomes important near the illuminated side, causing an incomplete Raman conversion and lowering the flux ratio F_{6825}/F_{7082} . In particular, the branching ratio into the Raman channel is higher for O VI 1038 than O VI 1032, the higher Raman conversion efficiency is obtained for O VI 1038 lowering the flux ratio F_{6825}/F_{7082} below unity.

In the range $10^{22} \text{ cm}^{-2} < N_{HI} < 10^{23} \text{ cm}^{-2}$, the flux ratio F_{6825}/F_{7082} tends to decrease as N_{HI} increases. However, the behavior of the flux ratio is not strictly monotonic due to deviation from single scattering approximation near scattering optical depth of unity. Lee et al. (2016) presented Monte Carlo simulations to compute the flux ratio F_{6825}/F_{7082} in a neutral scattering region taking a simple geometric shape including sphere, cylinder and slab. In particular, a flux ratio in excess of 3.3 was obtained in a spherical neutral region with a characteristic HI column density $\sim 10^{22} \text{ cm}^{-2}$. The flux ratio F_{6825}/F_{7082} in the case of spherical geometry is shown in Fig. 5. Lee et al. (2016) showed that the flux ratio F_{6825}/F_{7082} is significantly larger for a D type symbiotic star HM Sge than an S type AG Dra. This is understandable if we consider that the representative H I column density of an S type symbiotic star is higher than that of a D type due to smaller binary separation.

4 Profile Formation in Asymmetric Accretion Flows

One aspect that makes Raman O VI features special is their broad line profiles, which stems from inelasticity of scattering. The energy conservation dictates that the frequency ν_o of an outgoing Raman optical photon is related to that ν_i of the incident far UV photon by

$$\nu_i = \nu_o + \nu_\alpha, \quad (6)$$

where ν_α is the frequency of Ly α . This leads to

$$\frac{\Delta\nu_o}{\nu_o} = \left(\frac{\nu_i}{\nu_o}\right) \frac{\Delta\nu_i}{\nu_i}, \quad (7)$$

which says that the Raman profile is broadened by a factor ν_i/ν_o . In the case of Raman O VI features this factor amounts ~ 6 , forming very broad profiles.

One can look at the phenomenon of profile broadening by imagining a hypothetical observer moving away relativistically from the O VI emission source with a speed $\beta = v/c = 35/37 = [(1+z)^1 - 1]/[(1+z)^2 + 1]$ where $z = 5$. This observer measures the wavelength of an O VI line photon with a redshift of $z = 5$ so that the O VI line photon is observed as an optical photon with a wavelength exceeding 6000 Å. Not only the center wavelength is increased, the whole profile gets broadened, which can also be attributed to the time dilation effect of relativity. To this observer, the O VI emitters are moving quite slowly by a factor $(1+z)$. An analogous situation may be found when one considers observations of high z universe, where time is ticking slowly by the inverse of the scale factor $a = (1+z)^{-1}$. Considering Raman scattering converting a far UV photon into an optical photon as a wavelength stretching process we may regard it as an extreme Doppler effect, allowing us to probe the emission and scattering region with time flowing slowly.

Another aspect of the wavelength stretch effect is that the profiles of Raman O VI features are mainly determined by the relative motion of the far UV emission region with respect to the H I region and mostly independent of the observer's line of sight. Borrowing the analogy of the observer receding relativistically from the emitter-scatterer region, the motion of O VI and H I atoms is negligible and therefore the wavelength measured by the observer is determined by the relative motion between the line emitting O VI ion and the scattering H I atom. This special property allows one to take an edge-on view of the accretion stream from the vantage point in front of the mass donor. In other words one may state that the Raman O VI features are an ideal mirror located on the binary orbital plane in front of the giant.

Raman O VI features usually exhibit double or triple peak profiles with much more enhanced red peak than the blue counterpart. A natural interpretation is provided by invoking asymmetry in the accretion flow around the white dwarf, where the O VI density is higher on the entering side than on the opposite side. Moving away from the giant, the entrance side is responsible for the formation of the red part. This expectation is corroborated from a number of hydrodynamic computations including Mastrodemos & Morris (1998). Based on this idea, Lee & Kang (2007) showed that the double peak profiles of Raman 6825 features of D type symbiotic stars V1016 Cyg and HM Sge are consistent with the O VI emission region in Keplerian motion around the white dwarf with one side enhanced than the other. This idea is extended to explain the triple peak profiles of Raman 6825 and 7082 features in Sanduleak's star by Heo et al. (2016).

Heo et al. (2016) noted that the 6825 and 7082 features exhibit different profiles even though they originate from the same O VI ions. The disparity of the two profiles has been noted in early research works including Schmid et al. (1999). Resonance doublet lines from C IV 1548, 1551, N V 1238, 1243 and O VI 1032, 1038 having an isoelectronic configuration with Li are major coolants in various astrophysical plasma including the broad line region of active galactic nuclei. The doublet structure arises from transitions $S_{1/2} - P_{3/2,1/2}$, where the upper state is split into two fine structures due to spin-orbit coupling. The twice more sublevels of $P_{3/2}$ than $P_{1/2}$ lead to twice stronger O VI 1032 than O VI 1038. However, far UV spectroscopic observations show that the flux ratio F_{1032}/F_{1038} often deviates from two and exhibit various values between 1 and 2. As optical depth increases, thermalization operates to relax the flux ratio from 2 to 1.

As the accretion flow tends to be asymmetric in such a way that the flow on the entering side is convergent and divergent on the opposite side, the entrance side is characterized by a larger emission measure and a smaller flux ratio F_{1032}/F_{1038} than on the opposite side. The entrance side, moving away from the point of view of the giant, is responsible for the red part of the Raman O VI features. Therefore, if we normalize to a fixed flux of O VI 1032, relatively more 1038 photons are generated on this side than on the opposite side responsible for the blue part. This leads to relatively enhanced blue part of Raman 6825 compared with that of Raman 7082. The double peak profiles of V1016 Cyg exhibit this characteristic, consistent with their red enhanced

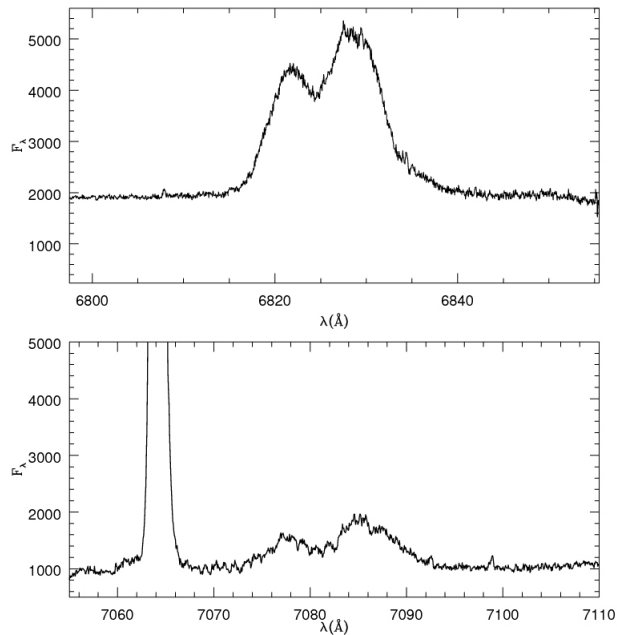


Figure 3: BOES spectrum of Raman OVI in the symbiotic nova V1016 Cyg.

profiles. In the case of Sanduleak’s star, the profile of the Raman 6825 feature has a single peak with an additional structures in the red shoulder region. In contrast, the Raman 7082 feature has a clear triple peak structure. By comparing these two profiles, Heo et al. (2016) proposed that the O VI emission region can be decomposed into 5 components including a disk and a bipolar outflowing component, which is consistent its huge jets discovered by Angeloni et al. (2012). Heo et al. (2016) assigned different flux ratios F_{1032}/F_{1038} to these components to successfully explain the profile difference of the two Raman O VI features in Sanduleak’s star. The difference in profiles of the two Raman features in a symbiotic star can be an extremely useful probe of the density distribution of the accretion flow around the white dwarf.

5 Polarization Flip and Bipolar Structure

It can be easily shown that both Rayleigh and Raman scattering processes are characterized by the scattering phase function the same as that of Thomson scattering. Composed of purely scattered photons, Raman O VI features are known to exhibit strong linear polarization with highly complicated structures. Harries & Howarth (1996) performed spectropolarimetric survey of symbiotic stars to show that they are linearly polarized with a typical degree of polarization of 10 percent. Usually the degree of polariza-

tion decreases as the number of scattering increases. Because of the smaller scattering optical depth of O VI 1038 than O I 1032, Raman 7082 features are generally more strongly polarized than Raman 6825 counterpart.

In the case of Raman O VI features, the scattering number is limited by the inverse of the branching ratio into $2s$ state, as is pointed out by Lee et al. (2016). The degree of polarization ~ 10 per cent is consistent with a few scattering number expected in a neutral region with $N_{HI} < 10^{23} \text{ cm}^{-2}$. In addition, in order to obtain sizable Raman flux the H I column density may exceed 10^{22} cm^{-2} to guarantee a couple of Rayleigh scatterings. This indicates an interesting range of H I column density considered in the work by Lee et al. (2016).

One of the most interesting phenomena that can be found in spectropolarimetry of Raman O VI features in symbiotic stars is the polarization flip often exhibited in the red wing part representing a receding speed of $\sim 50 - 100 \text{ km s}^{-1}$ with respect to the line center. In other words, the position angle of polarization differs by almost 90 degrees in the red wing part with respect to the blue and central parts of Raman O VI features. One explanation of this phenomenon invokes the bipolar structure that is associated with the accretion disk in symbiotic stars. The red wing part polarized in the opposite direction requires an additional component moving away from the accretion disk in the direction normal to the disk. Lee & Park (1999) proposed that clumpy neutral blobs may be blown away in the bipolar directions that may contribute to the red wing part with opposite polarization. These neutral blobs are suggested to be formed through Rayleigh-Taylor instability such as those found in the butterfly planetary nebula NGC6302 (e.g., Balick & Frank, 1997; Akashi & Soker, 2013).

Another interesting possibility is that the additional component moving along the polar direction is an O VI emission region that may be a part of a jet or a collimated outflow, such as the one found in Sanduleak's star. If there is another O VI emission region along the bipolar outflows, then the line of sight from this O VI region toward the H I region around the giant forms a scattering plane with the observer's line of sight different from that spanned by the line of sight connecting the giant and the white dwarf and the observer's line of sight. Polarization develops in the direction normal to the scattering plane so that the two scattering planes should differ by an angle $\geq 45^\circ$. Considering the size of $\sim 1 \text{ AU}$ of a giant, the additional O VI emission from this additional region should be mainly formed at a distance $\geq 1 \text{ AU}$ from the white dwarf.

Based on these ideas, a Monte Carlo approach for polarization development will be highly useful to put meaningful constraints on the theoretical models. Comparisons of future simulations of radiative transfer and spectropolarimetric observations will shed more light on the polarization structure that is closely related with the bipolar outflows in symbiotic stars.

6 Summary and Concluding Remarks

Raman scattered O VI features are so far unique spectral emission lines that are found exclusively in symbiotic stars. Their existence can be a good criterion for a symbiotic star. As is discussed in this conference, significantly more symbiotic stars will be discovered through imaging surveys on nearby external galaxies using a narrow band filter centered at Raman O VI 6825. The profiles characterized by red-enhanced multiple peaks are consistent with an asymmetric accretion flow around the white dwarf. The asymmetry in the accretion flow induces a local variation in the flux ratio F_{1032}/F_{1038} leading to disparity in the profiles of Raman O VI 6825 and 7082 features.

Strong linear polarization exhibited by Raman O VI features in symbiotic stars which indicates that these features are formed through a small number of Rayleigh scattering. This is, in turn, compatible with the characteristic H I column density $N_{HI} \sim 10^{22-23} \text{ cm}^{-2}$, which is typically obtained from a mass losing giant with mass loss rate $\sim 10^{-6} - 10^{-7} M_{\odot} \text{ yr}^{-1}$. Furthermore, the polarization flip in the red wing part can be explained by invoking either an additional H I region or an O VI emission region in the direction perpendicular to the accretion disk. This additional component should be moving away from the binary system with a speed $\sim 50 - 100 \text{ km s}^{-1}$. As is illustrated in symbiotic stars such as Sanduleak's star and the Southern Crab, bipolar morphology prevails, which is associated with the wind accretion in these systems. The polarization flip is an important key to understanding the bipolar morphology in symbiotic stars.

The orbital parameters of D type symbiotic stars are poorly known and one method to find the orbital period is polarimetric monitoring. This polarimetric monitoring has been successfully and more easily applied to S type symbiotics with orbital periods of several hundred days. However, for example, in the case of V1016 Cyg for which the orbital period is proposed to be of order one century, spectropolarimetry for several years is insufficient to clearly detect the change in position angle (e.g., Schild & Schmid, 1996). It will be exciting that spectropolarimetric observation with a time gap of a couple decades may reveal the binary orbital parameters of these mysterious objects.

References

- Akashi, M., & Soker, N., 2013, MNRAS, 436, 1961
- Angeloni, R., Di Mille, F., Ferreira Lopes, C. E., & Masetti, N., 2012, ApJL, 756, L21
- Balick, B., Frank, A., 1997, IAUS (Editors: Habing & Lamers), 180, 190
- Chang, S.-J., Lee, H.-W., & Yang, Y., 2017, MNRAS, 464, 5018
- Dopita, M. A., Nicholls, D. C., Sutherland, R. S., Kewley, L. J., & Groves, B. A., 2016, ApJL, 824, L13

- Harries, T. J., & Howarth, I. D., 1996, A&AS, 119, 61
- Heo, J.-E., Angeloni, R., Di Mille, F., Palma, T., & Lee, H.-W., 2016, ApJ, 833, 286
- Lee, H.-W., & Lee, K. W., 1997, MNRAS, 287, 211
- Lee, H.-W., & Park, M.-G., 1999, ApJL, 515, L89
- Lee, Y.-M., Lee, D.-S., Chang, S.-J. Heo, J.-E., Lee, H.-W. Hwang, N., Park, B.-G., & Lee. H.-G., 2016, ApJ, 833, 75
- Mastrodemos, N., & Morris, M., 1998, ApJ, 497, 303
- Schild, H. & Schmid, H. M., 1996, A&A, 310, 211
- Schmid, H. M., 1989, A&A, 211, L31
- Schmid, H. M., et al., 1999, A&A, 348, 950

Circumstellar Spirals/Shells/Arcs: the Message from Binary Stars*

Hyosun Kim¹

¹Academia Sinica Institute of Astronomy and Astrophysics, P.O. Box 23-141, Taipei 10617, Taiwan (hkim@asiaa.sinica.edu.tw)

²EACOA fellow

A consensus has grown in the past few decades that binarity is key in understanding the morphological diversities of the circumstellar envelopes (CSEs) surrounding stars in the Asymptotic Giant Branch (AGB) to Planetary Nebula (PN) phase. The possible roles of binaries in their shaping have, however, yet to be confirmed. Meanwhile, recurrent patterns are often found in the CSEs of AGB stars and the outer halos of PNe, providing a fossil record of the mass loss during the AGB phase. In this regard, recent molecular line observations using interferometric facilities have revealed the spatio-kinematics of such patterns. Numerical simulations of binary interactions producing spiral-shells have been extensively developed, revealing new probes for extracting the stellar and orbital properties from these patterns. I review recent theoretical and observational investigations on the circumstellar spiral-shell patterns and discuss their implications in linking binary properties to the asymmetric ejection events in the post-AGB phase.

Key Words: AGB and post-AGB - binaries - circumstellar matter - mass loss - wind and outflow

1 Introduction

Since the launch of the Hubble Space Telescope (HST) in 1990, there have been many unexpected discoveries. One major finding among those is the recurrent patterns in the CSEs of sources in late stellar evolutionary phases (see Fig. 1), with AFGL 2688 being the archetypical target (Sahai et al., 1998). The HST image revealed its nearly concentric rings, which are interpreted as the limb-brightened surfaces of probable spherical shell-like structures. The pattern appear disconnected near the equatorial plane and brightest along the polar axis of the nebula due to the nonuniform illumination by

*This paper's copyright is on Kim et al. 2017, in Planetary nebulae: Multiwavelength probes of stellar and galactic evolution, International Astronomical Union Symp. No. 323 (ed. X. Liu et al.), *in press*.

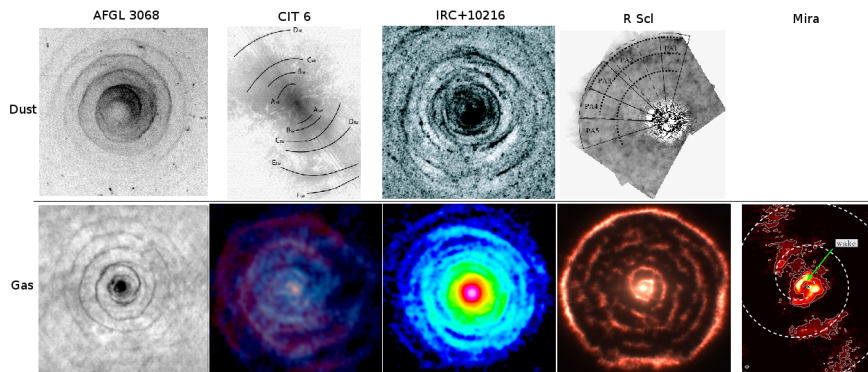


Figure 1: **Upper panels:** dust scattered light images of AFGL 3068 (Morris et al., in prep.), CIT 6 (Schmidt et al., 2002), IRC+10216 (Leão et al., 2006), and R Scl (Olofsson et al., 2010). **Lower panels:** CO center-frequency images of AFGL 3068 (Kim et al., 2017), CIT 6 (Kim et al., 2015), IRC+10216 (Cernicharo et al., 2015), R Scl (Maercker et al., 2012), and Mira (Ramstedt et al., 2014). The sets of upper and lower panels are scaled in size.

direct starlight.

Su (2004) first summarized the properties of 10 sources showing the ring/arc patterns. Corradi et al. (2004) and Ramos-Larios et al. (2016) searched for the faint patterns in a systematic way by processing the HST and Spitzer archival imaging data, increasing the accumulated number of objects possessing the recurrent patterns to ~ 60 . Recent molecular line observations using e.g., Atacama Large Millimeter/submillimeter Array (ALMA) and Karl G. Jansky Very Large Array (JVLA) have been discovering the previously unknown spirals and shells. Table 1 shows some notable works in observations and theories on the recurrent patterns.

The kinematic timescales of the pattern intervals ($10^2 - 10^3$ years) are inconsistent with either stellar pulsation or thermal pulsation. Su (2004) showed that the timescales show no distinguishable trend along the evolutionary phase, implying that the ring/arc patterns are not a transient phenomenon. This is in conflict with one-dimensional time-dependent hydrodynamics calculations with ionization taken into account, resulting in the patterns disappearing within ~ 3000 years after ionization starts (Meijerink et al., 2003). With the relevant model development (see Section 2) and the timescales consistent with the orbital periods of wide binaries, it is now commonly accepted that binary companions are responsible in modulating the mass distribution of CSEs in the recurrent form.

A remaining puzzle is their coexistence with bipolar structures in many pre-PNe (pPNe) and PNe. More than 80% of PNe are not spherical, but show a variety of morphologies including highly bipolar or multipolar structures, and many of them also have outer faint ring-like patterns. The recurrent patterns have timescales of the order of a few hundred years, which




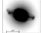
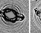


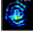
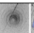
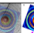
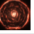

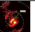
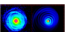
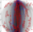
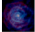
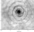
1994		Soker – spiral due to wide binary motion	
1997		Harpaz et al. – tidal interaction at periastron.	
1998	Sahai (AFGL 2688) 	... and many more from HST	long-term modulation of stellar pulsation
1999		Mastrodemos & Morris – binary	
2004	Corrai et al. (search for faint patterns)	  	
2006	Mauron & Huggins (AFGL 3068 spiral, HST)		
2011	Claussen (CIT6 rings, VLA)		
2012		Kim & Taam (a, b=parameter study, c=AFGL3068 spiral)	 
		Maercker et al. (R Scl spiral)	
2013		Kim et al. (CIT6 spiral, VLA)	
2014	Ramstedt et al. (Mira, ALMA)		
		Cernicharo et al. (IRC+10216 rose-window, IRAM)	
2015		Decin et al. (IRC+10216 spiral, ALMA)	
	Kim et al. (CIT6 spiral, SMA)		
2016		Kim et al. (AFGL 3068 spiral, ALMA)	

Table 1: Research highlights on the concentric ring-/arc-like patterns in the circumstellar envelopes of AGB stars and pPNe/PNe. In 1990s and 2000s, the HST observations and theories were rather independently investigated. In the current decade, thanks to the operations of high-sensitivity millimeter/submillimeter telescopes (e.g., ALMA, JVLA), the new detection of such patterns and their theoretical understanding have led to significant and synergistic progress.

correspond to the periods of *wide* binary stars. In contrast, the bipolar structures are the expected results of *close* binary interactions. I propose that a model involving a binary star system in an eccentric orbit can provide a plausible interpretation for the coexistence of these two geometrically distinct structures.

2 Binary-induced spiral-shell model

In a binary system, the orbital motion of the mass losing AGB star introduces an anisotropy in the actual speeds of wind gusts (Soker, 1994). The faster and slower wind gusts ejected over the orbit meet each other in the circumstellar space, forming a spiral pattern in the direction following the orbit. Mastrodemos & Morris (1999) showed, through smoothed-particle hydrodynamics simulations, the three dimensional spiral-shell nature of the circumstellar pattern induced by the binary orbital motion. The detailed structures are described in separate theoretical investigations for the patterns driven by the orbital motion of substellar-mass (e.g., planetary) companions (Kim & Taam, 2012a) and by the reflex motion of a mass-losing star in a comparable-mass binary system (Kim & Taam, 2012b). It is shown that

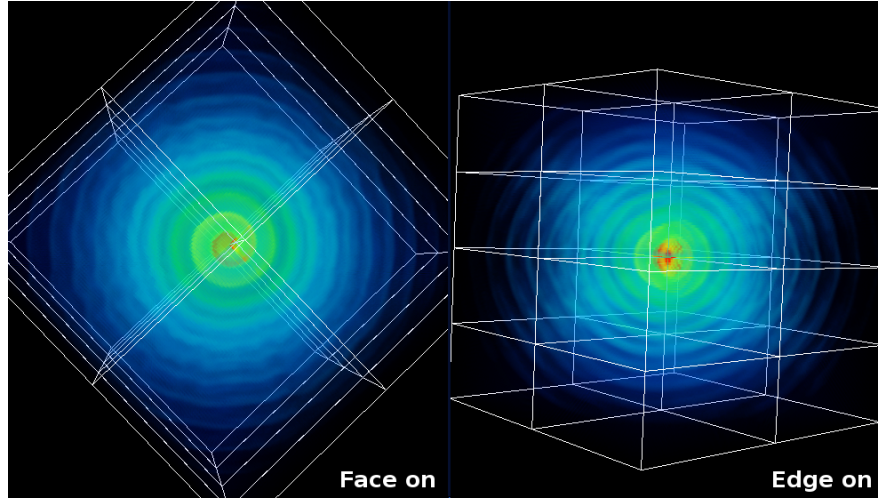


Figure 2: Circumstellar spiral-shell pattern induced by a binary in a circular orbit viewed at (*left*) face-on and (*right*) edge-on. The hydrodynamic simulation is performed using FLASH3.0 code. The density levels from blue (low) to red (high). Notice that the edge-on pattern consists of bicentric half-circles. Also notice the overall flattened morphology. Credit: Hsieh, Kim, & Liu.

the resulting geometrical details can be used to constrain the stellar masses and orbital properties (Kim & Taam, 2012c; Kim et al., 2013).

The spiral-shell model provides a framework for understanding the various recurrent patterns, which include not only a perfect spiral but also circular rings depending on the orbit inclination angle (face-on vs. edge-on). In the edge-on view, the pattern shape is bicentric half-circles, in general; but when the orbital speed is sufficiently low compared to the wind speed, it takes the form of nearly concentric rings (see e.g., Fig. 2). The projected shape becomes an elongated spiral at intermediate inclination angles, from which the inclination angle can be derived (Fig. 3; see Kim & Taam, 2012c, for details).

Using a simple geometric model, which is completely defined by five equations in Kim & Taam (2012c), a parameter space analysis for a projected spiral image can be performed. With four observables, mostly measured from the pattern shape, all binary orbital parameters can be derived. Once the parameter space is constrained, hydrodynamic models can be explored to fine tune the binary properties. Because the hydrodynamic modeling is expensive and time consuming, this pre-simulation analysis is very useful.

When an elongated spiral is projected onto a two-dimensional image, it could indicate an oblate ellipsoid halo viewed with a small inclination angle or an almost spherical halo with a very large inclination angle. This degeneracy is inherent in two-dimensional images such as that obtained from the HST. In the current era, high-resolution high-sensitivity interferometric

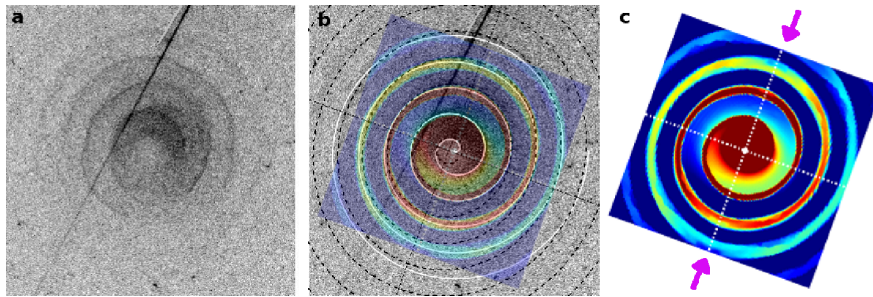


Figure 3: (a–b) AFGL 3068’s HST image ($25''.6 \times 25''.6$) is compared with (b–c) the density distribution in a hydrodynamic model (Kim & Taam, 2012c). The arrows in (c) denotes the line of nodes of the binary orbital plane with the plane of the sky. The orbital period is almost free from the projection effect, and in this case, it’s about 800 years.

data of molecular line emissions can be obtained providing kinematic information and, thus, the three-dimensional distribution of the pattern, lifting the degeneracy (see e.g., Kim et al., 2013, for details).

3 Eccentric long-period binaries

ALMA observations now reveal the detailed three-dimensional structure of the unambiguous and complete spiral pattern in AFGL 3068. In particular, the molecular line emission shows the innermost winding of the spiral pattern, which was absent in the HST dust scattered light image. It indicates that the innermost region of the CSE of AFGL 3068 is indeed extremely dense, thus, the penetration of interstellar UV photons required for scattering by the circumstellar dust is prohibited (see Fig. 1, leftmost panels). For the remaining windings, the dust and gas are well coupled.

The most exciting finding from the ALMA map of AFGL 3068 is the bifurcation of the spiral pattern, which is well reproduced by a highly eccentric-orbit binary model and cannot be mimicked by a circular-orbit model with any inclination (Fig. 4; Kim et al., 2017). This is the first solid piece of evidence for the existence of an eccentric binary system from a spiral pattern. We note that it is surprising that even the nearly perfect spiral source is not a circular-orbit binary. The similar and different patterns of various molecular line emissions are subject to detailed study of the radiative transfer and chemical compositional considerations to understand the physical conditions across the spiral shock.

An eccentric binary has also been suggested for another carbon star, CIT 6, based on the Submillimeter Array (SMA) observation (Fig. 5; Kim et al., 2015): 1) the one-sided gaps of interarm emission, which can be reproduced by an eccentric binary model (e.g. He, 2007; Raga et al., 2011); 2) inner double spiral feature, which can be found in a relatively slow wind outflow (e.g., Mohamed & Podsiadlowski, 2012) – the speculation is that

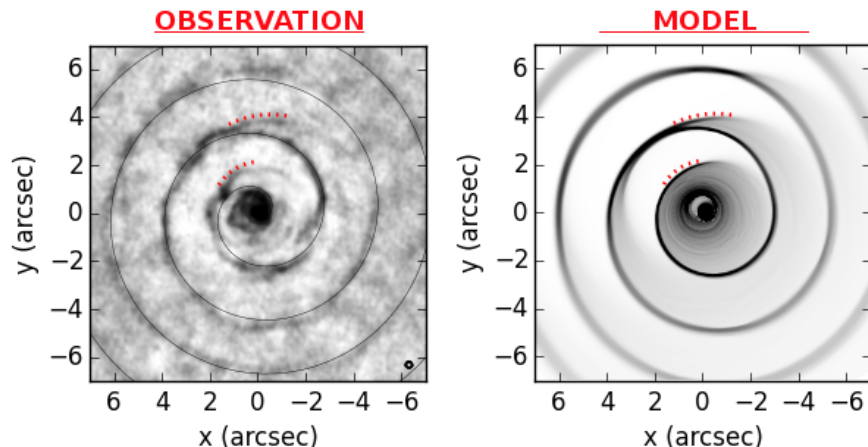


Figure 4: Bifurcation of the spiral pattern in AFGL 3068 revealing the eccentric binary nature. (*left*) ALMA observation versus (*right*) a hydrodynamic model of a binary with a large eccentricity of 0.8. The bifurcation is a distinctive characteristic of eccentric binary and cannot be reproduced by a circular binary model (Kim et al., 2017).

a highly eccentric orbit leads to the penetration of the companion into the wind acceleration zone; 3) nascent bipolar (or multipolar) structure at the line edges, which would be a result of strong interaction between the binary stars at periastron passages.

In Table 2, these two carbon stars proposed as members of long-period eccentric binaries are compared to V Hydrae, a carbon star that is showing bullet-like mass ejection every 8.5 years, which is the possible orbital period of a binary (Sahai et al., 2016). Indeed, the derived orbital periods have a relation with the presence and geometry of the bipolar structures. For a binary in a circular orbit with these long periods, there is no mechanism to produce to the bipolar structure. Perhaps, strong interactions at the close periastron passages for a component in an eccentric binary can lead to a gradual decrease in the orbital separation, eventually leading to the formation of a disk around the companion star where bipolar outflows can be launched. This remains as a hypothesis and more theoretical investigations are needed. If true, the orbital eccentricity must be a key parameter linking the observed spiral-shell patterns to the bipolar structures.

Is it reasonable to expect such high eccentric orbits for these objects? Raghavan et al. (2010) showed that the distribution of orbital eccentricity in the main-sequence binaries is random for systems with orbital periods greater than 10 days. The recent results for the eccentricity distribution of red giant binaries show a similar trend (van Winckel et al., in prep.). The above three objects with orbital periods longer than several years are well within the regime that the circularization does not occur.

A triple system is another possible scenario for explaining the coaxis-

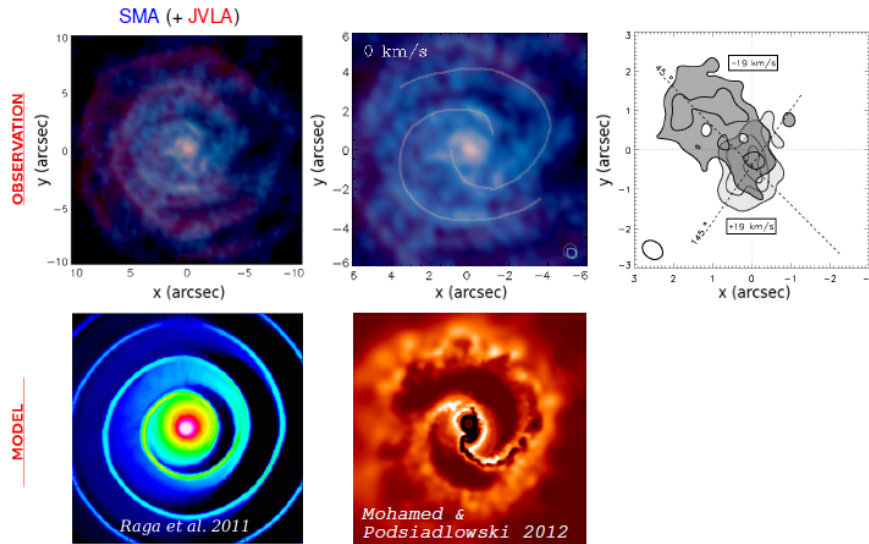


Figure 5: Hints of eccentric binary in CIT 6 (Kim et al., 2015): (*left*) one-sided gaps of interarm emission, (*middle*) inner double spiral feature, and (*right*) nascent bipolar (or multipolar) structure. These features of CIT 6 revealed in the SMA observations are compared with the hydrodynamic model for a highly eccentric-orbit binary by Raga et al. (2011) and the slow wind model by Mohamed & Podsiadlowski (2012), respectively.

tence of outer long-period spiral-shell patterns and inner bipolar structures, although it should be very fine-tuned. The primary and secondary objects should be distant to explain the timescale of outer pattern spacing as observed to be of the order of a few hundred years, while the third body should be located near the companion star launching the bipolar structure. Among possible triple system configurations, only such configuration works to explain the coexistence of two distinguished structures. Since the main-sequence fraction of triple and higher-order multiple systems is less than 10%, it would be difficult to understand all known pPNe and PNe having recurrent patterns (> 60 objects, according to Ramos-Larios et al., 2016) by triple systems.

4 Implications

Spiral patterns are now frequently detected in the CSEs of stars in the AGB phase thanks to the high-sensitivity high-resolution submillimeter/millimeter observations. This is a major step forward as many of them were not obvious in the dust scattered light images (Fig. 1). The complex rose-window pattern of IRC+10216 is understood in terms of a binary system, but requiring a mass loss variation (Cernicharo et al., 2015). For R Scl, a star that has

AFGL 3068	CIT 6	V Hydrae
~ 800 years	~ 300 years	8.5 years
no bipolar	broadened bipolar	bullet-like ejection
(Kim et al., 2017)	(Kim et al., 2015)	(Sahai et al., 2016)

Table 2: Comparison of three carbon stars AFGL 3068, CIT6, and V Hydrae tends to show a relation between the presence (and geometry) of bipolar structures and the orbital periods derived from either the spiral pattern or the mass ejection.

a spiral and a thermal pulse shell, Maercker et al. (2012) used the spiral property as a timer to estimate the thermal pulsation period. In the case of Mira, the ALMA data reveal overall complex structures, but because it has a confirmed white dwarf companion, the partial arcs could be connected as a spiral (Ramstedt et al., 2014). Many of these objects have a secondary point-like source as revealed in the near-infrared, optical, or radio continuum with apparent projected separations greater than 50 AU.

These five, best-known spiral/shell/arc objects are all in the AGB phase and are mostly carbon-rich. In order to determine whether the presence and evolution of circumstellar patterns depend on the stellar evolutionary phase and the chemical environment, molecular line surveys for AGB spirals in post-AGB sources are needed. Given such surveys, we can contemplate carrying out statistical studies of the known spiral/ring/arc sources. At the same time, analysis of the simplest objects, coupled with theoretical studies, will enable parameter estimation for a statistically meaningful sample. The golden era for studying the spiral-shell patterns is here, allowing us to progress in unravelling the nature and evolution of these evolved stars as encoded in their circumstellar patterns.

Acknowledgements H.K. acknowledges support for the travel and the work presented in this paper through the East Asian Core Observatories Association Fellowship, and thanks R. E. Taam and S.-Y. Liu for reviewing an early version of the manuscript.

References

- Cernicharo, J., Marcelino, N., Agúndez, M., & Guélin, M. 2015, *A&A*, 575, A91
- Corradi, R. L. M., Sánchez-Blázquez, P., Mellema, G., Giammanco, C., & Schwarz, H. E. 2004, *A&A*, 417, 637
- He, J. H. 2007, *A&A*, 467, 1081
- Kim, H., & Taam, R. E. 2012a, *ApJ*, 744, 136
- Kim, H., & Taam, R. E. 2012b, *ApJ*, 759, 59

- Kim, H., & Taam, R. E. 2012c, *ApJL*, 759, L22
- Kim, H., Hsieh, I.-T., Liu, S.-Y., & Taam, R. E. 2013, *ApJ*, 776, 86
- Kim, H., Liu, S.-Y., Hirano, N., et al. 2015, *ApJ*, 814, 61
- Kim, H., Trejo, A., Liu, S.-Y., et al. 2017, *Nat. Astron.*, 1, 0060
- Leão, I. C., de Laverny, P., Mékarnia, D., de Medeiros, J. R., & Vandame, B. 2006, *A&A*, 455, 187
- Maercker, M., Mohamed, S., Vlemmings, W. H. T., et al. 2012, *Nature*, 490, 232
- Mastrodemos, N., & Morris, M. 1999, *ApJ*, 523, 357
- Meijerink, R., Mellema, G., & Simis, Y. 2003, *A&A*, 405, 1075
- Mohamed, S., & Podsiadlowski, P. 2012, *Baltic Astronomy*, 21, 88
- Olofsson, H., Maercker, M., Eriksson, K., Gustafsson, B., & Schöier, F. 2010, *A&A*, 515, A27
- Raga, A. C., Cantó, J., Esquivel, A., Huggins, P. J., & Maun, N. 2011, in *Asymmetric Planetary Nebulae V Conference*, ed. A. A. Zijlstra et al. (Jodrell Bank Centre for Astrophysics, Manchester), 185
- Raghavan, D., McAlister, H. A., Henry, T. J., et al. 2010, *ApJS*, 190, 1
- Ramos-Larios, G., Santamaría, E., Guerrero, M. A., et al. 2016, *MNRAS*, 462, 610
- Ramstedt, S., Mohamed, S., Vlemmings, W. H. T., et al. 2014, *A&A*, 570, L14
- Sahai, R., Trauger, J. T., Watson, A. M., et al. 1998, *ApJ*, 493, 301
- Sahai, R., Scibelli, S., & Morris, M. R. 2016, *ApJ*, 827, 92
- Schmidt, G. D., Hines, D. C., & Swift, S. 2002, *ApJ*, 576, 429
- Soker, N. 1994, *MNRAS*, 270, 774
- Su, K. Y. L. 2004, in *ASP Conf. Ser. 313, Asymmetrical Planetary Nebulae III: Winds, Structure and the Thunderbird*, ed. M. Meixner et al. (San Francisco, CA: ASP), 247

Jets and Other Signs of Accretion in Planetary Nebulae

Romano L.M. Corradi

GRANTECAN, Cuesta de San José s/n, E-38712, Breña Baja, La Palma, Spain
Instituto de Astrofísica de Canarias, Vía Láctea s/n, E-38200, La Laguna, Tenerife, Spain

It is nowadays recognized that binarity is an essential ingredient to understand many properties of planetary nebulae (PNe), such as their varied morphologies, chemical composition, dynamical evolution, and perhaps even their formation. The number of known binary central stars in PNe has largely increased in the last decade, but the vast majority of discoveries are binaries with periods smaller than few days, as they are much more easily detected than longer period systems.

These close binaries, which went through a common envelope (CE) phase during the red giant phase of their progenitors, experience a variety of interactions with their companions. The presence of collimated outflows and jets, and the detection of chemically polluted or inflated secondaries, provide evidence for the occurrence of accretion at some stages of their recent evolution. Some illustrative examples are presented.

Discussion on the similar phenomena observed in symbiotic stars and their link with PNe is also included.

Key Words: jets – mass loss – accretion – planetary nebulae – symbiotic stars

1 Binarity in planetary nebulae

During several decades, it has been proposed that evolution of interacting binaries plays an important role to understand planetary nebulae (PNe). However, it is only in the last ten years that this idea has been supported by the discovery of a significant number of binary central stars.

Interacting binary stars can be divided in two main groups: those which are separated enough to avoid a common-envelope (CE) phase during the red-giant (RGB and AGB) phases of their progenitors (symbiotic-like), and those which go through it (CV-like, hereafter post-CE binaries).

The vast majority of known PN binary central stars belong to the second group, mainly because discovering short period binaries is a much easier task than for long-period systems, owing to their fast orbital motions and to the

conspicuous irradiation or gravitational effects produced on the companions.

The number of PN post-CE binaries known today is around 50, still only 2% of the total number of Galactic PNe, but enough to allow first statistical analyses of their frequency. Surprisingly, the present data imply that at least 15-20% of all PNe (Miszalski et al., 2009), and perhaps a much larger fraction, have a post-CE central star, contrary to population synthesis models that predict a fraction no larger than 2.5% (Maddapatt, De Marco & Villaver, 2016). This excess of post-CE PNe, if confirmed by ongoing observational programmes, would pose an important problem to understand the formation of PNe in general. Another potential problem is the paucity of PN binary central stars with orbital periods between one and several days (Jones, 2017), which is likely to be a real effect as discovery surveys are sensitive to this range of separations.

Very little information is instead available on long-period binaries (Van Winckel et al., 2014), although the study of extended nebulae around symbiotic stars suggest that even at separations of tens or hundred of years the gravitational interaction of binaries containing a red giant can significantly affect mass ejection (Corradi, 2003), and therefore the PN properties.

2 Post-CE binaries in PNe

These PNe are assumed to be the envelope of their AGB progenitors ejected at the end of the CE phase, when the orbital energy lost in the spiralling in of the companion inside the AGB envelope is transferred to the envelope that is eventually ejected. As the CE process is predicted to be very fast, and PN have lifetimes of only few ten thousand years at most, these systems are observed right after they leave the CE, and therefore provide unique constraints on the CE physics and properties such as the post-CE period distribution. The main general results obtained so far by studying post-CE PN binaries are:

- the nebular symmetry follows the orbital orientation, in the sense that the typical "equatorial" density enhancements observed in many PNe coincide with the orbital plane, and "polar" outflows expand along the orbital axis (Jones et al., 2017);
- in several cases (Corradi et al., 2015), the mass of the PN is too small to have produced the observed orbital shrinking. This is an additional, important problem that severely limits our understanding of the complex physics of CE phase. It is possible that these are not the AGB envelope ejected in the CE phase, but later mass outflow episodes from the post-CE binaries;
- post-CE PNe provide clues to apparently unrelated issues such as the abundance discrepancy problem (Corradi et al., 2015);
- there is **growing evidence for pre-during-post CE accretion**. The first indicator is the presence of **fast polar outflows (jets)**,

which are expected to be launched by accretion discs that are formed at some stages of the CE evolution. The second one is the detection of **chemically polluted secondaries**, containing carbon or s-process elements excesses that can only be explained by accretion from the primary star when it was on the AGB. The third one is the evidence for **inflated secondaries** (i.e. with radii larger than the corresponding ones for main-sequence stars of the same spectral type), which is explained to be a consequence of rapid CE mass accretion, to which the star has not yet thermally adjusted. Some illustrative cases are presented below.

2.1 Fleming 1

Fg 1 is the first PN in which the formation of *precessing* jets has been shown to arise in a binary system (Boffin et al., 2012) as predicted since long time ago by theory (Figure 1).

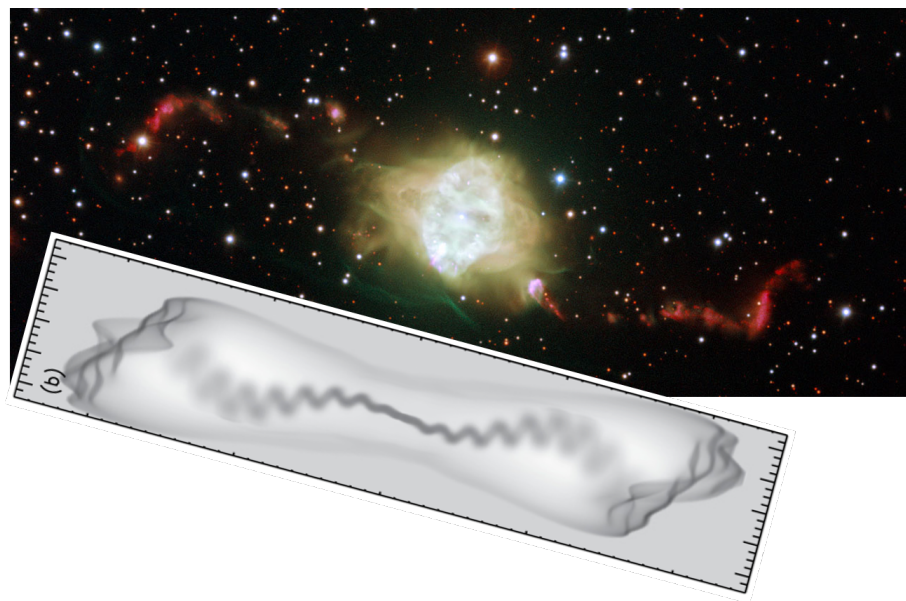


Figure 1: In colour, the image of Fg1 from Boffin et al. (2012). Below, in grey-scale, the simulation of a precessing jets by Raga et al. (2009), which produces a very similar morphology, but for orbital periods four or five orders of magnitude longer than the one of Fg 1 (1.2 days).

2.2 The Necklace nebula

The Necklace PN is a textbook illustration of the kind of mass outflows that are generally observed in interacting binary stars (Figure 2). From the analysis of its morphology and dynamics, it is found that most of the stellar

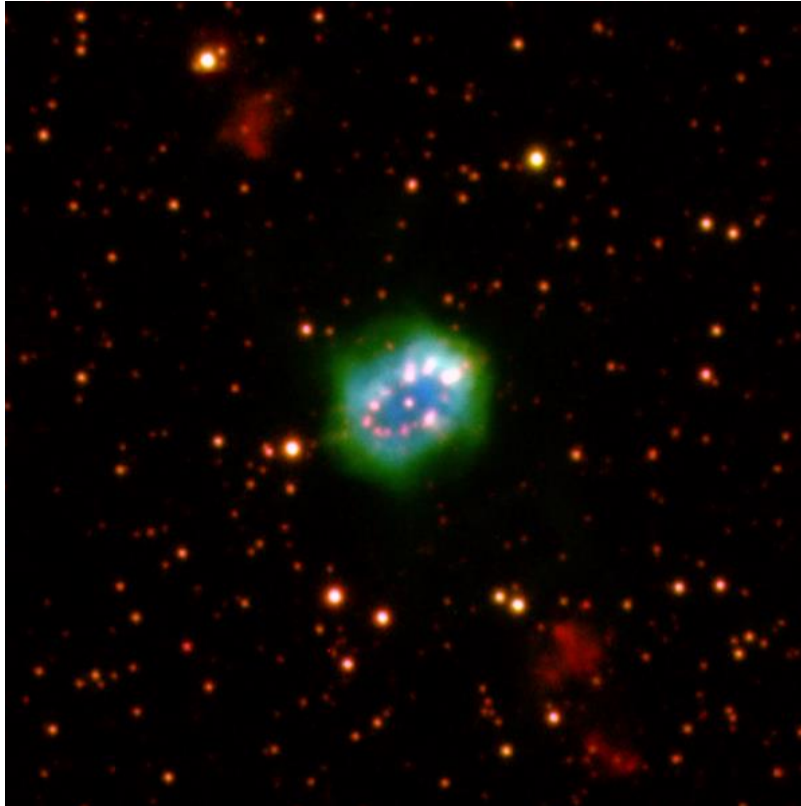


Figure 2: The Necklace nebula.

envelope was lost in the orbital plane, forming the slowly expanding inner nebula and its remarkable knotty ring. Much less massive, faster outflows are ejected in the polar directions. These short-lived, tenuous jets are expected to be ejected by an accretion disc from one of the stars of the system. In the Necklace nebula, it was also found that the kinematic age of the jet is larger than the age of the inner nebula (Corradi et al., 2011). As the latter is supposed to be the result of the CE ejection, it would imply that the jets were formed before the very short CE phase. The same effect is found in other objects, which further supports the idea that **pre-CE accretion** is common.

Furthermore, in the case of the Necklace nebula it has been found that the secondary star is carbon rich (Miszalski, Boffin & Corradi, 2013). As carbon is not produced in main-sequence stars, the companion must have accreted it from the primary when it was a carbon AGB star. In the same process, the fast polar outflows may have been ejected.

2.3 s-process enrichment and inflated secondaries

In addition to the case of carbon enrichment of the secondary star of the Necklace nebula, other binary PNe have giant companions in a pre-AGB phase which are enriched with s-process elements such as barium (Miszal-ski et al., 2013). This is considered another indirect evidence of chemical pollution by accretion of material from the PN progenitor.

Similarly, the fact that every well constrained main-sequence secondary has a radius larger than it would correspond to a main-sequence star of the same spectral type (Jones, 2017), is likely to indicate that these stars have been inflated as a consequence of rapid CE mass accretion, and have not yet returned to thermal equilibrium.

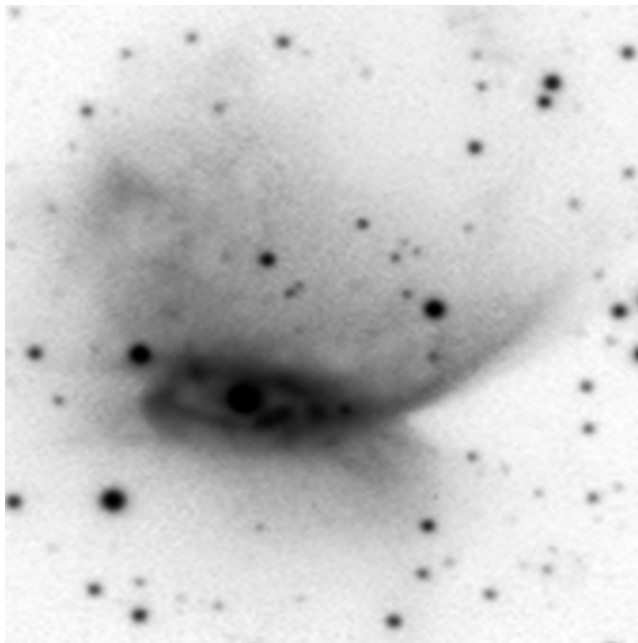


Figure 3: Henize 2-428.

2.4 Double degenerates: SN Ia progenitors?

Henize 2-428 (Figure 3) is an evolved bipolar PN, with an unresolved, dense nebular core where mass exchange within the central binary system may still be going on. Santander-García et al. (2015) measured the light and radial velocity curves of the system. This allowed to determine the orbital and system parameters, indicating that He 2-428 contains a short-period, double-degenerate binary with a total mass of 1.9 solar masses, well above the Chandrasekhar limit. The two stars are predicted to merge within 700 million years exploding as a SN Ia, which makes He 2-428 one of the best candidates of the elusive progenitors of this important class of supernovae.

Double-degenerate PN central stars of PN might be quite common, up to 25% of the PNe with close-binary nuclei according to Hillwig (2013). Among them, another two systems may exceed the Chandrasekhar limit: TS 01 (Tovmassian et al., 2010) and V458 Vul (Rodríguez-Gil et al., 2010). For these reasons, post-CE PN central stars may provide a channel to SN Ia much more common than previously thought.

3 Links with symbiotic stars

It is worth reminding the formal, physical distinction between these two classes. PNe are the ejected AGB envelopes photoionized by the hot post-AGB stellar remnants. Symbiotic stars are long-period binaries composed of a hot white dwarf that is accreting and photoionizing the wind of a red giant companion.

The copious mass loss that characterizes both systems, producing a dense circumstellar environment, together with the action of a hot (pre)white dwarf and its associated fast winds or nova-like explosions, result in extended ionized nebulae that present strong morphological, dynamical and chemical similarities. This makes it difficult to distinguish some PNe from nebulae around symbiotic stars, and misclassification is likely to be present in the literature.

Indeed, a large fraction of D-type symbiotic stars, i.e. those containing an AGB star, display extended nebulae, most of which with a marked bipolar morphology (Corradi et al., 1999). The main difference with PNe is the nebular mass, that is generally much smaller in symbiotic stars ($\sim 10^{-3}$ solar masses). An exception is He 2-104, the Southern Crab, whose ionized nebular mass is estimated to be 0.1 solar masses (Santander-García et al., 2008), close to typical values for PNe.

Symbiotic nebulae show the ability of **wind accretion** to produce collimated outflows such as bilobal/bipolar nebulae and prominent jets (see the spectacular cases of R Aqr, or of the huge jet from the Sanduleak star in the LMC, Angeloni et al. 2011), even at the very large separations of these binary systems, that correspond to orbital periods as large as several hundreds of years.

3.1 Minkowsky 2-9: unique and puzzling

M 2-9 is an outstanding bipolar nebula whose binary (symbiotic?) nature, suggested by the nebular morphology and the spectral characteristics of its dense core, could not be proven yet. The unique property of M 2-9 is the lighthouse effect (Figure 4) on the walls of its bipolar lobes, which is thought to be produced by a bended jet that is rotating with a period of 90 years (Corradi et al., 2011b).

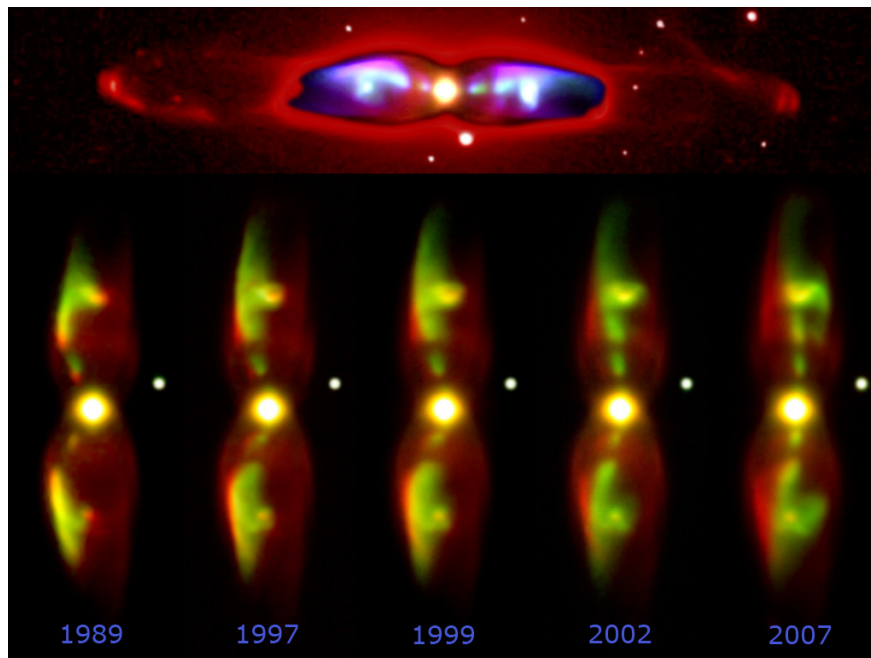


Figure 4: Minkowski 2-9, observed at different epochs.

4 Conclusion

The discovery of a significant number of close binary central stars in PNe has brought a wealth of new information about the common-envelope phase, one of the most important but also most uncertain processes in binary evolution. As it usually happens, the new information also raises new problems that makes understanding the CE and PN phases intricate. Among the most relevant issues, we need to understand why there are so many post-CE PN central stars, why most have periods shorter than one day, and why a number of nebulae have such a low mass that cannot be produced following the standard CE scenario.

Concerning accretion processes in these systems, it is clear that there is a lot of new - albeit indirect- evidence provided by their collimated fast outflows, or by the chemical or dynamical peculiarities of the secondary stars. These phenomena are also highly relevant for other astrophysical topics, such as the formation of the cosmologically important SNe Ia.

Symbiotic stars are a different class of interacting binaries, but produce large scale outflows (rings, bipolar lobes, jets) very similar to those observed in much closer binaries. Preferential mass ejection along the equatorial (orbital) plane seems to be a common property regardless of the binary separation, the physics of the accretion (via a disc or wind), and the mechanism of ejection (CE ejection, intrinsic stellar mass loss, nova-like phenomena).

These similarities are also cause of misclassification, and in some cases of

recurrent misuse of the term "symbiotic" to label all nebulae with a prominent bipolar morphology and dense nebular core. Effort should be dedicated to clean misclassification as much as possible, to better understand which specific physical processes produce the fascinating properties observed in PNe, symbiotic stars, and related objects.

Acknowledgements I would like to thank the organizers of this conference, and in particular Rodolfo Angeloni and Hee-Won Lee, for their kind invitation, the travel support, and the warm hospitality, which allowed me to be part of such an enjoyable and inspiring conference.

References

- Angeloni, R., Di Mille, F., Bland-Hawthorn, J., Osip, D.J. 2011, *ApJL*, 743, L8
- Boffin, H.M.J., et al. 2012, *Science*, 338, 773
- Corradi, R.L.M. 2003, in *Symbiotic stars probing stellar evolution*, ASP Conf. Ser. Vol. 303, p. 393
- Corradi, R.L.M., et al. 2009, *A&A*, 343, 841
- Corradi, R.L.M., et al. 2011, *MNRAS*, 410, 1349
- Corradi, R.L.M., et al. 2011b, *A&A*, 529, A43
- Corradi, R.L.M. et al. 2015, *ApJ*, 803, 99
- Hillwig, T. 2013 *ASPC* 469, 277
- Jones, D., et al. 2014, *Asymmetrical Planetary Nebulae VI conference*, C. Morisset, G. Delgado-Inglada and S. Torres-Peimbert eds. Online at <http://www.astroscu.unam.mx/apn6/PROCEEDINGS/>, id.43
- Jones, D. 2017, to appear in the proceedings of IAUS323: Planetary nebulae: Multiwavelength probes of stellar and galactic evolution
- Maddapatt, De Marco, O. & Villaver, E. 2016, *MNRAS*, 463, 1040
- Miszalski, B., et al. 2009, *A&A* 496, 813
- Miszalski, B., Boffin, H.M.J. & Corradi, R.L.M. 2013, *MNRAS*, 428, L39
- Miszalski, B., et al. 2013, *MNRAS* 436, 3068
- Raga, A.C., et al. 2009, *ApJ*, 707, L6
- Rodriguez-Gil, P. et al. 2010, *MNRAS*, 407, L21
- Santander-García, M., et al. 2008, *A&A* 485, 117
- Santander-García, M., et al. 2015, *Nature*, 519, 63

Tovmassian, G. et al. 2010, ApJ, 714, 178

Van Winckel et al. 2014 A&A 563, L10

GHOST: The Gemini High-Resolution Optical Spectrograph

Steve J. Margheim

Gemini Observatory, Southern Operations Center, Chile

Abstract: The Gemini High-Resolution Spectrograph (GHOST) is the next facility instrument for Gemini Observatory. It is being developed in collaboration with the Australian Astronomical Observatory (AAO), NRC-Herzberg, and the Australian National University (ANU). GHOST will provide $R=50,000$ and $R=75,000$ spectroscopy with simultaneous wavelength coverage between 363 and 950 nm. GHOST supports simultaneous observation of two objects at $R=50,000$ and a single object at $R>75,000$.

Key Words: instrumentation

1 GHOST Overview

The Gemini High-Resolution Optical Spectrograph (GHOST) is the next facility instrument under development for Gemini Observatory. The instrument project is a collaboration with the Australian Astronomical Observatory (AAO), Canada's National Research Council Herzberg (NRC-Herzberg), and the Australian National University (ANU). GHOST is designed to serve a broad scientific community as a workhorse high-resolution spectrograph.

GHOST is a fiber-fed echelle spectrograph with a single-object high-resolution mode ($R>75,000$) and a two-object standard resolution mode ($R>50,000$). The spectrograph is fed by micro-lens based integral field units, which image slice a 1.2 arcsec object field-of-view. The spectrograph itself is located in the pier lab of Gemini for stability. The spectrograph is a two arm asymmetric white pupil design, utilizing Volume Phase Holographic Gratings (VPHG) for cross dispersion. The blue camera uses a 4kx4k detector and the red camera uses a 6kx6k detector. These large-format detectors allow for the full continuous wavelength coverage of 363nm to 950nm in a two arm design.

The spectrograph is expected to have a limiting magnitude of 18 at 450nm, defined as 30 sigma per resolution element in a single 3600s exposure. The spectrograph will have a radial velocity of 600 m/s in standard resolution mode. A simultaneous calibration source is available in the high-resolution mode for precision radial velocity observations. The expected radial velocity precision in this mode is 10 m/s.

As of February 2017, the GHOST instrument is currently in the build

phase. Instrument commissioning is planned for the third quarter of 2018. Full availability of GHOST to the Gemini Community is expected in 2019.

Oral Session

The Accretion Column of AE Aqr

Claudia V. Rodrigues¹, Karleyne M. G. Silva², G. Juan M. Luna³, Jaziel G. Coelho¹, Isabel J. Lima (INPE), ¹, Joaquim E. R. Costa (INPE)¹, and J. Carlos N. de Araujo (INPE)¹

¹Instituto Nacional de Pesquisas Espaciais, Brazil

²Gemini Observatory

³Instituto de Astronomía y Física del Espacio, Argentina

AE Aqr is a magnetic cataclysmic variable, whose white dwarf rotates at the very fast rate of 33 s modulating the flux from high energies to optical wavelengths. There are many studies about the origin of its emission, which consider emission from a rotating magnetic field or from an accretion column. Recent observations have not found emission from AE Aqr in gamma rays, putting difficulties for the pulsar-like model. Furthermore, X-ray data can be fit using thermal models. Here we present a successful modeling of AE Aqr X-ray spectra and light curve considering the emission of a magnetic accretion column using the CYCLOPS code. The model takes into consideration the 3D geometry of the system, allowing to properly represent the white-dwarf auto eclipse, the pre-shock column absorption, and the varying density and temperature of a tall accretion column. To our knowledge, we present the first physical modeling of AE Aqr light curve in high energies.

Key Words: Accretion, accretion disks - Magnetic fields - Radiative transfer - novae, cataclysmic variables - Stars: individual: AE Aqr - X-rays: stars

1 Introduction

AE Aqr is classified as a magnetic cataclysmic variable (CV). Its orbital period is 9.88 h and consistent with a K4-5V secondary star (Patterson et al., 1980). In CVs, the secondary loses mass by Roche Lobe overflow, which is accreted by the white-dwarf. If the white-dwarf magnetic field is intense enough to influence the accretion dynamics, we have a magnetic CV. In these systems, the main emitting region is the accretion column portion located between the shock front and the white-dwarf surface, the so called post-shock region.

The emission of AE Aqr from X rays to optical wavelengths is modulated at 33 s. This is interpreted as the white-dwarf spin period (Patterson et al., 1980), making the white dwarf in AE Aqr the fastest in a CV system. There is only one faster white dwarf, RX J0648.04418, which is in a post

common-envelope binary (Israel et al., 1997; Bisscheroux et al., 1997). This fast rotation has led Wynn, King, & Horne (1997) to propose that AE Aqr has a propeller regime, in which the centrifugal force of the white-dwarf magnetosphere prevents the accretion. In this case, the 33 s flux modulation would be associated with some kind of pulsar-like white-dwarf emission (e.g., Ikhsanov & Biermann, 2006). The existence of white-dwarf pulsars is a compelling question and is associated with alternative models of magnetars based on fast, massive, and magnetized WDs (e.g., Coelho & Malheiro, 2014; Lobato, Malheiro, & Coelho, 2016).

The recent strong upper limits to the gamma-ray emission of AE Aqr from MAGIC and Fermi (Aleksić et al., 2014; Li et al., 2016) puts strict constraints to pulsar-like models. Moreover, some observational data have been successfully explained by an accretion scenario. Eracleous et al. (1994) used a polar-cap model (consistent with an accretion-induced hot spot) to fit the optical and UV light curves of AE Aqr. Kitaguchi et al. (2014) fitted the soft and hard X-ray emission of AE Aqr using a bremsstrahlung thermal model, consistent with an accretion column.

In this proceedings, we present a preliminary fit of the X-ray emission of AE Aqr using a magnetic accretion model. Complementing previous studies, we propose a possible geometry that explains AE Aqr X-ray light curve.

2 Modeling the X-ray emission of AE Aqr

Our aim is to find a geometrical and physical model for the X-ray spectrum and light curve of AE Aqr. We utilize NuSTAR and Swift data, which were presented by Kitaguchi et al. (2014).

The fitting of AE Aqr data was done using the CYCLOPS code (Costa & Rodrigues, 2009; Silva et al., 2013). The CYCLOPS code calculates the continuum emission from post-shock regions in magnetic accretion geometries. The code implements emission from cyclotron and bremsstrahlung processes. It considers the photo absorption by material internal to the binary and also by the interstellar medium. CYCLOPS adopts a 3D representation. Hence phase-dependent internal binary absorption and occultation are consistently considered from a geometrical perspective. The physical parameters, as the density and temperature, can be set variable along the emission region according to a shock structure. The code uses the convolution routines of PINTOFALE (Kashyap & Drake, 2000) to consider the high-energy instrumental files in the data fitting procedure.

3 Preliminary results

The time-integrated spectrum of AE Aqr strongly constrains the temperature distribution. Figure 1 shows the X-ray spectra fit using a model with a shock temperature of 4 keV, consistent with previous results (e.g., Kitaguchi et al., 2014). Figure 2 presents the radial temperature and density distribution used in the fit. The region with $E < 2$ keV of the spectrum (shown

in red in Figure 1) was not considered in the fitting procedure, because it is dominated by emission lines and only free-free continuum emission was presently included in the code.

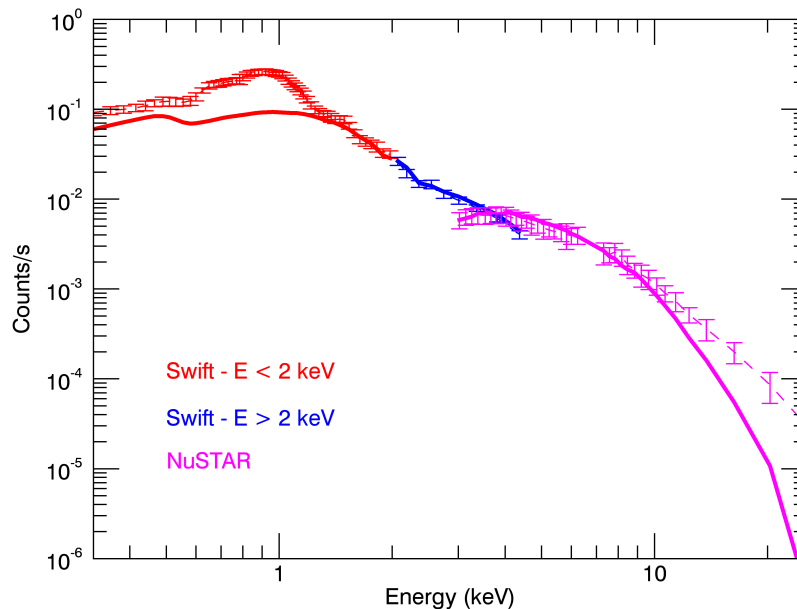


Figure 1: Swift and NuSTAR spectra of AE Aqr (error bars) and the CYCLOPS model for a shock structure having $T_{\max} = 4$ keV (solid line).

But whereas the X-ray spectrum of AE Aqr can be fit by many combinations of geometrical parameters (as long as the temperature distribution is kept similar), the same is not true for the light curve. Figure 3 shows a preliminary fit of the light curve of AE Aqr from 3 to 20 keV. The flux modulation is caused by partial eclipse of the accretion column by the white dwarf. Figure 4 illustrates the view of the post-shock region along the white-dwarf rotation. The main geometrical parameters are:

- inclination is 67 deg;
- the emission region is located 42 deg from the rotation pole and extended by 30 deg in longitude and has 0.12 white-dwarf radius in height;
- the magnetic-field axis is parallel to the rotation axis.

The magnetic field is a necessary ingredient of our modeling because the accretion column geometry is defined by the magnetic field lines. However, our model does not depend on the magnetic field value because it is not a parameter for the free-free emission. The model counts are normalized to

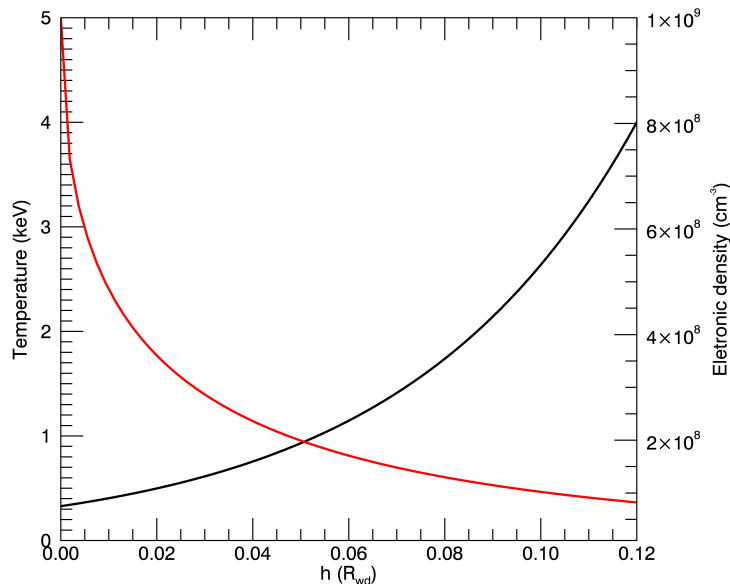


Figure 2: Radial distributions of density (red) and temperature (black) adopted in the model.

reproduce the observations at one point, hence the electron density is not well constrained by the present modeling.

The spectrum and light curve represent the output of the same model.

4 Conclusions and perspectives

We present a preliminary physical and geometrical scenario for AE Aqr high energy emission. It is based on a post-shock region near the white-dwarf surface created by magnetic accretion. It explains X-ray AE Aqr spectrum and rotational flux variation. As far as we know, this is the first model to the X-ray light curve of AE Aqr.

To improve the fitting procedure, we plan to: (i) fit time resolved X-ray spectra; (ii) adopt different shock structures, including other cooling process; (iii) exploit properly the parameter space to understand the degeneracy of parameters. To verify the consistency of the physical and geometrical description of AE Aqr, we plan to compare the model luminosity with observations and extend the model to other wavelengths.

Acknowledgements This work was supported by CNPq (CVR: 306701/2015-4), Fapesp (IJJ: 2015/24393-7 – CVR, JGC, ISL: 2013/26258-4 – JGC: 2013/15088-0), FONCyT/PICT (GJML: 2014/0478). The CVR’s travel was funded by Capes/Brazil, CNPq/Brazil and the meeting sponsors.

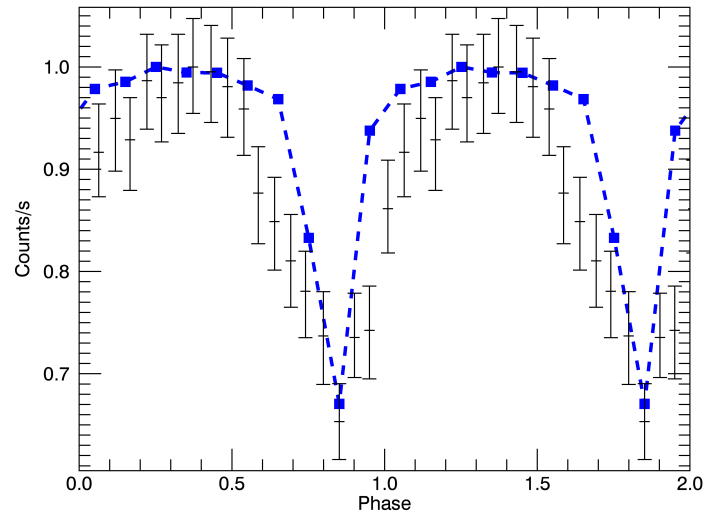


Figure 3: CYCLOPS model to the light curve of AE Aqr from 3 to 20 keV (blue line). The error bars are the data from Kitaguchi et al. (2014).

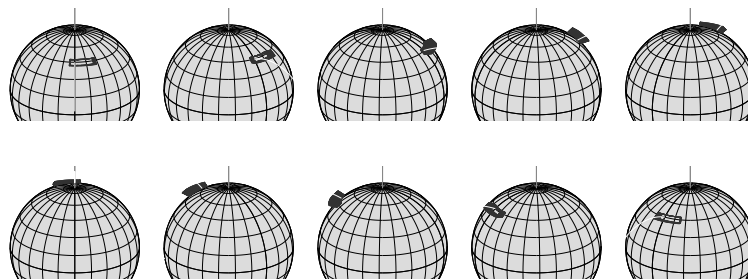


Figure 4: The post shock region of the AE Aqr model seen along the spin cycle of the white dwarf.

References

- Aleksić J., et al., 2014, *A&A*, 568, A109
- Bisscheroux B. C., Pols O. R., Kahabka P., Belloni T., van den Heuvel E. P. J., 1997, *A&A*, 317, 815
- Coelho J. G., Malheiro M., 2014, *PASJ*, 66, 14
- Costa J. E. R., Rodrigues C. V., 2009, *MNRAS*, 398, 240
- Eracleous M., Horne K., Robinson E. L., Zhang E.-H., Marsh T. R., Wood J. H., 1994, *ApJ*, 433, 313
- Ikhsanov N. R., Biermann P. L., 2006, *A&A*, 445, 305
- Israel G. L., Stella L., Angelini L., White N. E., Kallman T. R., Giommi P., Treves A., 1997, *ApJ*, 474, L53
- Kashyap V., Drake J. J., 2000, *BASI*, 28, 475
- Kitaguchi T., et al., 2014, *ApJ*, 782, 3
- Li J., Torres D. F., Rea N., de Oña Wilhelmi E., Papitto A., Hou X., Mauche C. W., 2016, *ApJ*, 832, 35
- Lobato R. V., Malheiro M., Coelho J. G., 2016, *IJMPD*, 25, 1641025
- Patterson J., Branch D., Chincarini G., Robinson E. L., 1980, *ApJ*, 240, L133
- Silva K. M. G., Rodrigues C. V., Costa J. E. R., de Souza C. A., Cieslinski D., Hickel G. R., 2013, *MNRAS*, 432, 1587
- Wynn G. A., King A. R., Horne K., 1997, *MNRAS*, 286, 436

Raman O VI Profile Analysis of Accretion and Bipolar Outflows in Sanduleak's Star

Jeong-Eun Heo¹, Rodolfo Angeloni², Francesco Di Mille³, Tali Palma⁴, and Hee-Won Lee¹

¹Department of Physics and Astronomy, Sejong University, Seoul, Korea

²Gemini Observatory, La Serena, Chile

³Las Campanas Observatory, La Serena, Chile

⁴Departamento de Ciencias Físicas, Universidad Andrés Bello, Santiago, Chile

Sanduleak's star is a suspected symbiotic binary in the Large Magellanic Cloud known to have a huge jet that extends a physical size of 14 pc. Located in the Large Magellanic Cloud, Sanduleak's star shows two strong emission bands at 6825 Å and 7082 Å. These bands are formed through Raman scattering of O VI $\lambda\lambda$ 1032 and 1038 doublet by atomic hydrogen and so far only unambiguously confirmed in symbiotic stars. In this work, we present the high-resolution spectrum of Sanduleak's star obtained with the Magellan-Clay telescope to investigate the O VI emission region based on the profiles of the two Raman bands. The Raman 7082 Å band exhibits a clear triple-peak structure, whereas the Raman 6825 Å band shows a single-peak profile with an extended bump in the red part. Based on our profile analysis we propose that the O VI emission region consists of three main emission parts: an accretion disk, a bipolar outflow and an optically thin, compact component surrounding the white dwarf. Our Monte Carlo results indicate that the observed flux ratio in the two Raman bands $F(6825)/F(7082) \sim 4.5$ is consistent with the representative column density of the H I scattering region $N_{HI} \sim 1 \times 10^{23} \text{ cm}^{-2}$.

Key Words: binaries: symbiotic line: profiles radiative transfer scattering stars: individual (Sanduleak's star)

1 Introduction

Sanduleak's star resides in the Large Magellanic Cloud, whose symbiotic activities were disclosed by Sanduleak (1977). In particular, Angeloni et al. (2011) reported their discovery of the powerful jet in this object, whose

physical extent is estimated to be ~ 14 pc establishing itself as one of the largest stellar jets reported thus far. In fact, bipolar outflows seem to be associated with the binarity of their central source (Sahai et al. 2011).

Despite lack of evidence for the presence of a giant component in this object, the symbiotic nature can be inferred from highly ionized emission lines reminiscent of a dusty type symbiotic star (Munari & Zwitter 2002) and a clear detection of Raman-scattered O VI bands at 6825 Å and 7082 Å (Schmid 1989). So far these Raman-scattered O VI bands have been detected only in *bona fide* symbiotic stars, and served as one of the criteria for classifying a star as symbiotic (Belczyński et al. 2000).

According to Schmid (1989), an O VI λ 1032 photon that is incident on a hydrogen atom in the ground 1s state may be scattered to become an optical photon with wavelength 6825 Å leaving the scattering hydrogen atom in an excited 2s state. An analogous process for O VI λ 1038 photons results in a Raman-scattered band at 7082 Å. The cross section being of order 10^{-22} cm², the operation of Raman scattering requires a special condition of the coexistence of a thick neutral component and a strong far-UV emission source, which is ideally met in symbiotic stars (Nussbaumer et al. 1989).

The wavelength of a Raman scattered line photon is mainly determined by the motion of the emitter relative to the scatterer, which is attributed to the inelasticity of scattering. This unique property of Raman O VI bands provides an edge-on view as seen from the donor star, allowing us to investigate the mass transfer process in symbiotic systems (Lee & Park 1999). Adopting a Keplerian accretion flow around the white dwarf, Lee & Kang (2007) provided a successful fit to the Raman 6825 Å bands in the two symbiotic novae V1016 Cyg and HM Sge. They attributed the asymmetric double-peak profiles exhibited in these two objects to the O VI emission region taking the form of an accretion disk surrounding the white dwarf.

Another interesting feature of the two Raman O VI bands is that, in many cases, they exhibit different profiles, in which the blue part of a Raman 6825 Å band is stronger than the Raman 7082 Å counterpart, despite the fact that they share the same place of formation (Harries & Howarth 1996; Schmid et al. 1999). Heo & Lee (2015) performed a quantitative profile comparison of the two Raman O VI bands at 6825 Å and 7082 Å of V1016 Cyg in the parent Doppler factor space. They suggested that the local variation of the flux ratio $F(1032)/F(1038)$ in the emission region leads to the profile disparity in the two Raman bands.

In an optically thin nebula, the ratio tends to $F(1032)/F(1038) = 2$ because the 1032 transition has twice stronger oscillator strength than the 1038 transition. Thermalization becomes important in a nebula with a high optical depth, resulting in the flux ratio $F(1032)/F(1038)$ approaching 1 (Kang & Lee 2008; Schmid et al. 1999). If the O VI emission region is inhomogeneous and is divided into a large number of small spots, then each O VI emission spot is characterized by the Doppler factor with respect to the H I region and the flux ratio $F(1032)/F(1038)$ determined by the local density. Therefore, the entire profile of two Raman bands reflects the information about the density distribution and the kinematics of the emission

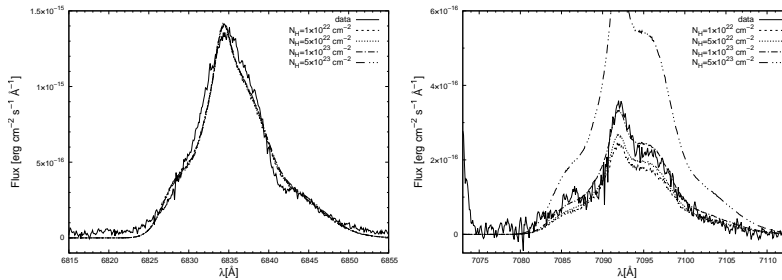


Figure 1: The Raman O VI bands at 6825 Å (left) and 7082 Å (right) in Sanduleak’s star. The solid line shows the observation, while the dotted lines represents the results of our Monte Carlo simulations for various N_{HI} .

region. In this presentation, we show a detailed profile analysis of the Raman O VI bands demonstrating that the O VI emission region is formed in the accretion flow and bipolar outflowing regions in Sanduleak’s star.

2 Observation and Profile Decomposition

2.1 High Resolution Spectroscopy

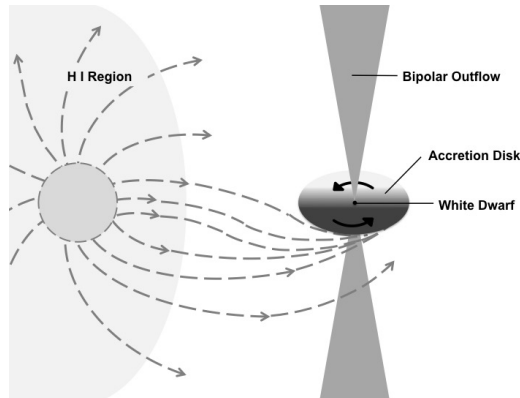


Figure 2: Schematic model of Sanduleak’s star. The O VI emission region is assumed to consist of an accretion disk, bipolar outflows and a further optically thick compact component. The strong far UV radiation from the hot component photoionizes partly the stellar wind from the giant forming a neutral H I region in the vicinity of the giant companion. See text for details.

High-resolution spectroscopy of Sanduleak’s star were carried out on 2010 November 21 using the *Magellan Inamori Kyocera Echelle* (MIKE) spectrograph mounted on the 6.5 m Magellan-Clay telescope, Las Campanas Observatory in Chile. We used the 0.7×5 arcsec slit with spectral resolution of

$\sim 32,000$ and took a series of 3×900 sec exposures. More information can be found in Heo et. al (2016). We present the Raman-scattered O VI $\lambda\lambda$ bands at 6825 \AA and 7082 \AA of Sanduleak's star in the left and right panels in Fig. 1, respectively. The data are indicated by the solid lines. It is noteworthy that these two Raman bands have very different profiles. In the case of the Raman 6825 \AA band, a single broad peak dominates the profile with an extended bump in the red side, whereas the Raman 7082 \AA band shows a distinct triple-peak structure.

In order to reconstruct the O VI far-UV emission lines based on the observed profiles of the Raman O VI bands, we divide the O VI emission region into five emitting components: a) Blue Emission Part (BEP) and Red Emission Part (REP) and b) Central Emission Part (CEP) of an accretion disk, c) a bipolar outflow and d) an optically thick compact component. For the sake of simplicity, each component is described by a Gaussian function characterized by a central velocity ΔV_{atm} , a FWHM Δv and a peak value f , the latter normalized at the peak value of the 1032 line. A schematic illustration of Sanduleak's star is shown in Fig. 2.

2.2 Blue Emission Part (BEP) and Red Emission Part (REP) from the Accretion Disk

We assume that the blue and red peaks of the Raman 7082 \AA band are associated with the accretion disk, and fit them with a FWHM of $\Delta v \sim 28 \text{ km s}^{-1}$. Their peak separation ($\sim 70 \text{ km s}^{-1}$) implies a Keplerian motion with 1 AU scale, which have been proposed for other symbiotic stars (Lee & Kang 2007). By setting the average velocity of the two peaks as null-velocity, we introduce the parameter ΔV_{OVI} defined by the velocity of the O VI emission region with respect to the H I scattering region and shown by dotted lines in Fig. 3.

The two Gaussian components corresponding to the blue and red peaks represent the approaching and the receding parts of the accretion disk with respect to the scattering region, respectively. These parts correspond to the Blue Emission Part (BEP) and Red Emission Part (REP), respectively, discussed in the previous subsection. Taking into account that the red-peak is stronger than the blue-peak, we assign $F(1032)/F(1038) = 2$ to BEP and 1 to REP, which is consistent with a density inhomogeneity in the accretion disk.

2.3 Central Emission Part (CEP) in the Accretion Disk

It should be noted that the null-velocity region apparent in the observed spectrum is not covered by invoking only BEP and REP. Also considering the triple-peak structure of the Raman 7082 \AA band, an additional part at $\Delta V_{OVI} \sim 0$ is needed. As in the previous section, we refer to this component as the Central Emission Part (CEP). The contribution to the Raman 7082 band of the CEP should remain to a minimum in order to preserve the triple-peak structure strongly implying that the CEP is characterized by

Table 1: Line Profile Parameters - Doppler factors, corresponding central wavelengths, FWHM (Δv), and peak values of the five Gaussian components (see text for details).

Emission Region	ΔV_{atm} (km s ⁻¹)	ΔV_{OVI} (km s ⁻¹)	λ_{1032} (Å)	λ_{1038} (Å)	Δv (km s ⁻¹)	f_{1032}	f_{1038}
Accretion Disk (BEP)	-20	-34	1031.859	1037.549	28.3	0.22	0.11
Accretion Disk (REP)	48	34	1032.093	1037.784	28.3	0.22	0.22
Accretion Disk (CEP)	20	6	1032.997	1037.687	41.6	0.8	0.4
Bipolar Outflow	71	57	1032.172	1037.864	66.6	0.24	0.12
Optically Thick Compact Component	19	5	1032.993	1037.684	11.7	0.18	0.18

$F(1032)/F(1038) = 2$. The best fitting parameter is obtained with $\Delta V_{OVI} = 6$ km s⁻¹, $\Delta v \sim 42$ km s⁻¹, which implies an extended volume covering a wide velocity range. The CEP may be identified with a coronal component that is implied from various X-ray observations of symbiotic stars (e.g. Luna et al. 2013)

2.4 Bipolar Outflow

Another notable feature in the Raman 6825 Å band is the extended red bump with a representative velocity of $\Delta V_{OVI} = +57$ km s⁻¹. However there is no corresponding feature in the Raman 7082 Å band at the same velocity. Considering the high radial velocity of this emitting component and the presence of the huge jet in Sanduleak's star, this component is most plausibly attributed to the bipolar outflow region. The best fit is obtained for a selection of the Gaussian function characterized by $\Delta v \sim 67$ km s⁻¹ and the flux ratio $F(1032)/F(1038) = 2$.

2.5 Optically Thick Compact Component

The clear and sharp central peak of the Raman 7082 Å band requires the introduction of a weak and narrow component with $\Delta V_{OVI} \sim 0$. Our fitting analysis indicates that the velocity with respect to the H I region $\Delta V_{OVI} = +5$ km s⁻¹, the Gaussian width of $\Delta v \sim 12$ km s⁻¹ and the flux ratio of $F(1032)/F(1038) = 1$. This result shows that that the optically thick component is nearly stationary or very slowly moving with respect to the scattering region. One suggestion for this component is the outer region on the red side of the accretion disk, where we expect that the accretion flow is convergent. This component is also reminiscent of the hot spot of the accretion disk in cataclysmic variables, where the material injected from the inner Lagrangian point hits the outer part of the accretion disk.

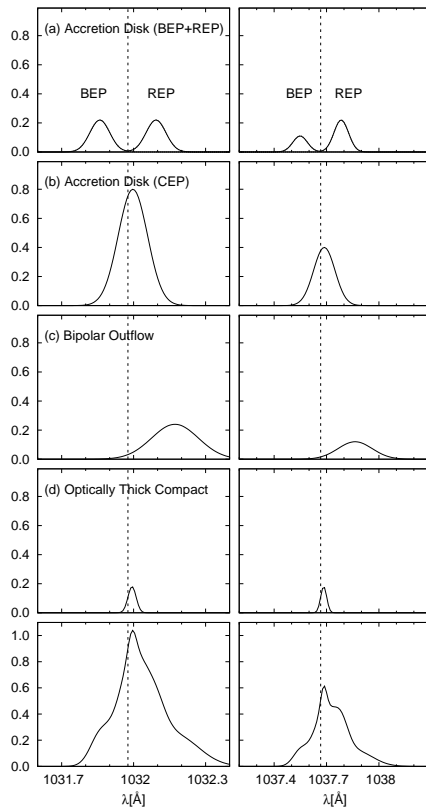


Figure 3: Profile synthesis of the far-UV O VI $\lambda\lambda$ 1032, 1038 doublet based on the observed Raman bands in Sanduleak’s star. All parameters of Gaussian functions can be found in Table 1.

3 Monte Carlo Simulations

Our high resolution spectroscopy yields the flux ratio $F(6825)/F(7082) \sim 4.5$. We perform Monte Carlo simulations to find the representative column density of the H I scattering region N_{HI} that is compatible with the observed flux ratio of $\sim 4/5$. In this work we assume a stationary neutral scattering region with respect to the white dwarf so that we can deal with the relative kinematics between the O VI emission region and the scattering region.

We vary N_{HI} from $1 \times 10^{22} \text{ cm}^{-2}$ to $5 \times 10^{23} \text{ cm}^{-2}$ in order to find the best fitting profile of the Raman 7082 Å band while the Raman 6825 Å band is kept fixed. The results of our Monte Carlo simulations for various N_{HI} are shown by dotted lines in Fig. 1. The observed spectrum is fitted satisfactorily with the choice of $N_{HI} = 1 \times 10^{23} \text{ cm}^{-2}$. However, the Raman conversion efficiency is also dependent on the binary separation and mass loss rate, which are highly uncertain for Sanduleak’s star.

4 Summary and Discussion

The two Raman O VI bands at 6825 Å and 7082 Å show disparate profiles, it appears that the triple peak structure of the 7082 band necessarily requires the presence of the accretion disk with a few additional structures. Furthermore, the observed huge jet feature in Sanduleak's star invokes an O VI emission region moving away from the binary system contributing the red part of Raman O VI bands at both 6825 and 7082 Å. The clear disparity of the two observed Raman O VI bands points out unambiguously local variations of the flux ratio $F(1032)/F(1038)$ ranging from one to two depending on the O VI ion density. We expect that the red part contributed from the O VI photons formed in the outflowing region along the jet directions will be polarized in the direction parallel to the orbital plane, whereas the remaining major parts of the Raman O VI bands are polarized in the direction parallel to the jet axis. Spectropolarimetry will shed much more light on the accretion flow and bipolar outflowing structure in Sanduleak's star.

Acknowledgements This research was supported by the Korea Astronomy and Space Science Institute under the R&D program (Project No. 2015-1-320-18) supervised by the Ministry of Science, ICT and Future Planning.

References

- Angeloni, R., Di Mille, F., Bland-Hawthorn, J. & Osip, D. J. 2011, ApJ, 743, L8
- Belczyński, K., Mikołajewska, J., Munari, U., Ivison, R. J. & Friedjung, M. 2000, A&AS, 146, 407
- Harries, T. J. & Howarth, I. D. 1996, A&AS, 119, 61
- Heo, J.-E. & Lee, H.-W. 2015, J. Korean Astron. Soc., 48, 105
- Heo, J.-E., Angeloni, R., Di Mille, F., Palma, T. & Lee, H.-W. 2016, ApJ, 833, 286
- Kang, E.-H. & Lee, H.-W. 2008, J. Korean Astron. Soc., 41, 49
- Lee, H.-W. & Kang, S. 2007, ApJ, 669, 1156
- Lee, H.-W. & Park, M.-G.. 1999, ApJL, 515, L89
- Luna, G. J. M., Sokoloski, J. L., Mukai, K. Nelson, T., 2013, A&A, 559, 6
- Munari, U., Zwitter, T. 2002, A&A, 383, 188
- Nussbaumer, H. Schmid, H. M. & Vogel, M., 1989, A&A, 211, L27
- Sahai, R., Morris, M. R. & Villar, G. G. 2011, AJ, 141, 134

Sanduleak, N., 1977, IBVS, 1304, 1

Schmid, H. M. 1989, A&A, 211, L31

Schmid, H. M., et al. 1999, A&A, 348, 950

Hunting Stellar-mass Black Holes in X-ray Binaries

Jesús M. Corral-Santana¹

¹European Southern Observatory (ESO), Alonso de Córdova 3107, Vitacura, Casilla 19001, Santiago, Chile

Since the beginning of the X-ray astronomy era, we have detected nearly 60 Galactic stellar-mass black hole (BH) candidates in transient X-ray binaries –a type of interacting X-ray binaries with low-mass companions– and 2 other systems with high-mass companion stars. However, only 17 out of the ~ 60 have been dynamically confirmed since 1966. Actually, during this decade, we have confirmed only one black hole (XTE J1859+226) and establish strong constraints in two more systems (Swift J1357.2-0933 and KY TrA). The former has been established as the most massive black hole transient ever measured in our Galaxy with more than $9 M_{\odot}$. In *BlackCAT: A catalogue of stellar-mass black holes in X-ray binaries* we present a thorough compilation of all the dynamical parameters of the BH transients and show a statistical analysis of the expected population of BH transients in our Galaxy based on observations. Thus, we estimate 1300 systems in the Milky Way, implying that we have only detected the tip of the iceberg of a hidden population of black hole transients. In this contribution, we will introduce the X-ray binaries, summarise their status and present the latest discoveries in the field.

Key Words: X-ray binaries – black holes – accretion

1 Introduction

X-ray binaries are systems formed by a compact object (either a neutron star or a black hole) which is fed by an accompanying star, oftenly in the main-sequence. According to the mass of the star, they classify in high-mass or low-mass X-ray binaries, being completely different in their properties. Thus, high-mass X-ray binaries are formed by early spectral type stars (O–B) which usually transfer material to the compact object via the strong stellar winds. Thus, the optical spectrum is dominated by the contribution of the hot star. They have long orbital periods (i.e. days) and short lifetimes ($10^5 - 10^7$ yr). On the other hand, low-mass X-ray binaries usually have late spectral type stars (K–M) which transfer material through Roche lobe overflow forming an accretion disc around the compact object. Unlike the high-mass type, the

optical spectrum in low-mass binaries is a combination of both the accretion disc and the cold star. The orbital periods in these systems are typically in the range of hours with lifetimes between 10^7 and 10^9 years.

There are only 2 high-mass X-ray binaries in the Galaxy with confirmed BHs whereas there are 18 dynamically confirmed BHs in low-mass X-ray binaries (see e.g. Corral-Santana et al., 2016). Among the high-mass X-ray binaries, Cyg X-1 is the most known one. It was discovered in 1964 (Giacconi et al., 1967) and was promptly appointed as a firm BH candidate Bolton (1972); Webster & Murdin (1972). But it was not until recently when there was a big improvement in the measurements of the dynamical parameters finding a $15 \pm 1 M_{\odot}$ BH with an O9.7Iab companion star of $19 \pm 2 M_{\odot}$ (Orosz et al., 2011). This does not fill the Roche lobe but transfer the material through stellar winds at a ratio of $10^{-8} M_{\odot}/\text{yr}$. On the other hand, MWC 656 –the other BH confirmed in a high-mass X-ray binary– was discovered as the γ -ray source AGL J2241+4454 (Casares et al., 2012) but later was identified as a BH with a Be-star companion due to the presence of an HeII emission line produced in an accretion disc (Casares et al., 2014). This is the first Be–BH X-ray binary system ever detected and has a low mass transfer rate ($10^{-11} M_{\odot}/\text{yr}$). The BH is supposed to be between 3.8 and $6.9 M_{\odot}$ fed by a B1.5–2III star of 10–15 M_{\odot} orbiting around the center of masses every 60.4 d. From all the above, it seems clear that we should focus on low-mass X-ray binaries to search for new BHs since the high-mass X-ray binaries has not proven to be the ideal type.

2 Black hole transients

Most of the BHs have been found in a type of low-mass X-ray binaries called *transients*. These are characterized by sporadic outburst episodes produced by thermal-viscous instabilities in the accretion disc (which usually last months) followed by long quiescent states where the systems stays more of their lifetimes (years to centuries). During the outburst state, they increase the brightness in all wavelengths but it is due to the increase in X-ray what allows the detection of the new source by the all-sky monitors on-board the X-ray satellites. These systems follow a very characteristic hysteresis pattern in an hardness-intensity diagram in X-rays during outburst (see e.g. Belloni et al., 2011). Due to this, all systems that follow the same behaviour, are classified as BH candidates. However, to firmly confirm the true nature of the compact object, we need to perform dynamical studies. These must be done during the quiescence state, when the star dominates the optical emission. As a matter of fact, during the 50 years of the X-ray astronomy era, we have detected nearly 60 BH transients but we have only confirmed the presence of BH in 18 out of them, i.e. only a third of the detected population (see Fig. 1) which indicates the difficulty to obtain the dynamical parameters. Although the rate of discoveries of new systems has increased since the 1980's with the improvement in the sensitivity of the X-ray detectors, the way of discovery of new systems only through outburst

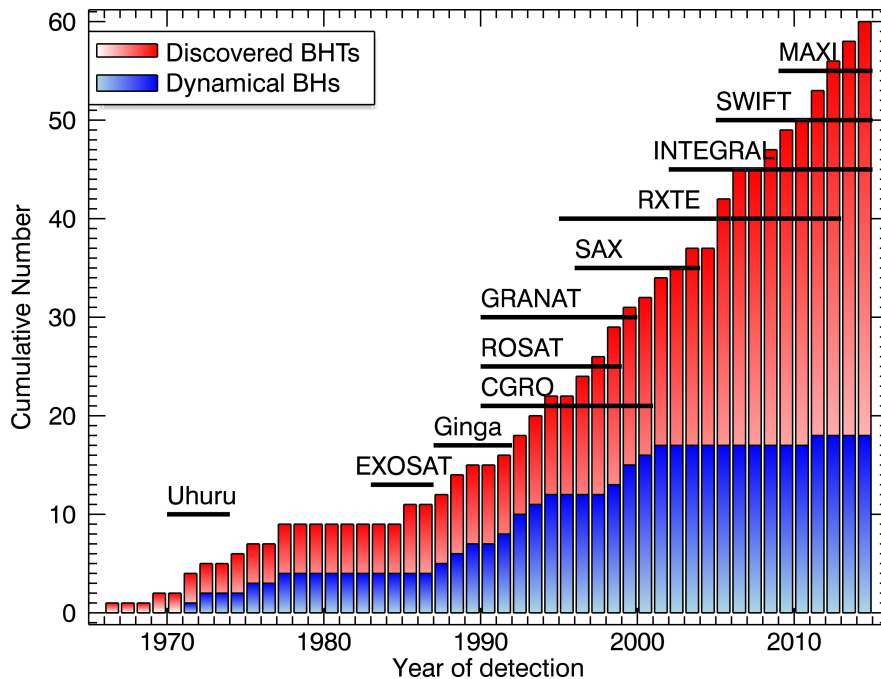


Figure 1: Cumulative histogram of the detection of black hole transients (BHT; red) and dynamically confirmed BHs (blue). Taken from Corral-Santana et al. (2016)

episodes is clearly inefficient and we require new methods. On the other hand, the dynamical confirmation of new systems is also problematic due to the faintness and/or high extinction of these systems in quiescence. Several studies using different approaches have established a Galactic population of $10^3 - 10^4$ black hole transients. Recently, we have obtained an estimation of 1300 BH transients in the Galaxy (Corral-Santana et al., 2016) by analysing the observed population and distribution of the systems. Therefore, we have only detected the tip of the iceberg of a hidden population of BH transients.

Another open debate on these sources is the existence of a gap between 2 to 5 M_{\odot} in the mass distribution of the dynamically confirmed BHs (see Fig. 2). It is expected that the mass distribution of compact objects is smooth because of its correlation with the masses of the progenitor stars. In Fig. 2 we see that the measurements in the masses of BHs suffer of 20-30% uncertainties, mainly due to the low accuracy in the values of the binary inclination. There is an open debate about the nature of this gap. Some authors believe it is due to a selection effect (Özel et al., 2010; Farr et al., 2011), others due to the errors in the inclination already mentioned (Kreidberg et al., 2012) and others believe that it is real i.e. due to physical processes (Belczynski et al., 2012; Fryer et al., 2012). Actually, some studies suggest that this gap might be related with the absence of supernovae type-

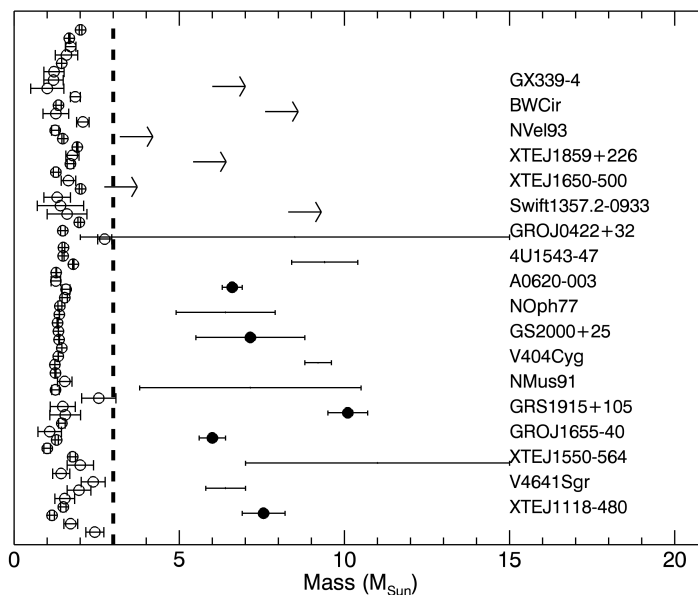


Figure 2: Mass distribution of compact objects: neutron stars in open circles and black holes in solid circles. Taken from Corral-Santana et al. (2016)

II progenitors between roughly 18 and 25 M_{\odot} (see e.g. Kochanek, 2014, for more details about this).

One of the most exiting BHs confirmed is Swift J1357.2–0933. It was discovered in 2011 during its only outburst episode reported so far. During this phase, we discovered very unique properties (see e.g. Corral-Santana et al., 2013) suggesting an edge-on inclination and we could measure an orbital period of only 2.8 ± 0.3 h, the second shortest reported so far in an X-ray binary. With data taken in quiescence, we could pinpoint the value of the radial velocity of the secondary star to 967 ± 49 km/s and a distance of at least 2.29 kpc, placing this system in the thick disc of the Milky Way (Mata Sánchez et al., 2015). These values imply a mass of the BH of at least $9.3 M_{\odot}$, being the most massive BH transient in the Galaxy. We must note here that the companion star of this system has never been found. Therefore, strictly speaking, it is not a dynamical confirmation. Thus, the radial velocity measures were obtained i) in outburst, using an empirical relation which scales the double-peak separation of the $H\alpha$ line and the radial velocity (Orosz et al., 1994; Orosz & Bailyn, 1995) and ii) in quiescence, using a new empirical relation between the full-width at half-maximum of the $H\alpha$ line (Casares, 2015) and the radial velocity. In conclusion, all these values present very robust evidences of the presence of a BH in the system.

3 Conclusions

In the last 50 years we have discovered nearly 60 BH transients in the Galaxy. Of those, we have only confirmed the presence of BHs in 2 systems with high-mass companions and in 18 systems with low-mass companions. The last estimates, based on the observational properties of the systems already detected, indicate that there should be around 1300 BH transients in the Milky Way. Therefore, our understanding on these types of source is clearly biased by our poor statistics. Thus, new techniques to uncover them while they are in quiescence and also to confirm the presence of BHs are urgently needed.

Acknowledgements This research has been made with the collaboration of Franz E. Bauer, Jorge Casares, Teodoro Muñoz-Darias, Pablo Rodríguez-Gil, Dave Russell, Tariq Shahbaz and Manuel A. P. Torres among others. I thank all of them for their contribution.

References

- Belczynski K., Wiktorowicz G., Fryer C. L., Holz D. E., Kalogera V., 2012, *ApJ*, 757, 91
- Belloni T. M., Motta S. E., Muñoz-Darias T., 2011, arXiv:1109.3388
- Bolton C. T., 1972, *Nat. Phys.*, 235, 271
- Casares J., 2015, *ApJ*, 808, 80
- Casares J., Ribó M., Ribas I., Paredes J. M., Vilardell F., Negueruela I., 2012, *MNRAS*, 421, 1103
- Casares J., Negueruela I., Ribó M., Ribas I., Paredes J. M., Herrero A., Simón-Díaz S., 2014, *Nat. Phys.*, 505, 378
- Corral-Santana J. M., Casares J., Muñoz-Darias T., Rodríguez-Gil P., Shahbaz T., Torres M. A. P., Zurita C., Tyndall A., 2013, *Science*, 339, 1048
- Corral-Santana J. M., Casares J., Muñoz-Darias T., Bauer F. E., Martínez-Pais I. G., Russell D. M., 2016, *A&A*, 587, A61
- Farr W. M., Sravan N., Cantrell A., Kreidberg L., Bailyn C. D., Mandel I., Kalogera V., 2011, *ApJ*, 741, 103
- Fryer C. L., Belczynski K., Wiktorowicz G., Dominik M., Kalogera V., Holz D. E., 2012, *ApJ*, 749, 91
- Giacconi R., Gorenstein P., Gursky H., Waters J. R., 1967, *ApJ Lett.*, 148, L119
- Kochanek C. S., 2014, *ApJ*, 785, 28

- Kreidberg L., Bailyn C. D., Farr W. M., Kalogera V., 2012, *ApJ*, 757, 36
- Mata Sánchez D., Muñoz-Darias T., Casares J., Corral-Santana J. M., Shahbaz T., 2015, *MNRAS*, 454, 2199
- Orosz J. A., Bailyn C. D., 1995, *ApJ Lett.*, 446, L59+
- Orosz J. A., Bailyn C. D., Remillard R. A., McClintock J. E., Foltz C. B., 1994, *ApJ*, 436, 848
- Orosz J. A., McClintock J. E., Aufdenberg J. P., Remillard R. A., Reid M. J., Narayan R., Gou L., 2011, *ApJ*, 742, 84
- Özel F., Psaltis D., Narayan R., McClintock J. E., 2010, *ApJ*, 725, 1918
- Webster B. L., Murdin P., 1972, *Nat. Phys.*, 235, 37

Investigating Scattering Processes in the Symbiotic Nova V1016 Cyg

Matej Sekeráš and Augustin Skopal

Astronomical Institute of Slovak Academy of Sciences

V1016 Cyg is a D-type symbiotic star. Environment of V1016 Cyg can be investigated throughout the observed effects of the Thomson and Raman scattering processes. Thomson scattering produces very broad and shallow wings of most intense emission lines. Modeling the line profile of O VI 1032, 1038Å resonance doublet, we determined the optical depth and electron temperature of the nebula in V1016 Cyg. Investigating Raman scattering of the He II 1025Å emission line into the emission feature at 6545Å, we determined the efficiency of this process, and using a simplified ionization model of symbiotic stars, we estimated the mass-loss rate of the Mira-variable of $\sim 10^{-6} M_{\odot}\text{yr}^{-1}$. Using only the optical spectrum represents a strong advantage of this method to determine the mass-loss rate in D-type symbiotic stars.

Key Words: symbiotic star - line profile - scattering - mass loss

1 Introduction

Symbiotic star V1016 Cyg comprises a cool giant, which is the type of Mira variable and a hot white dwarf embedded in a symbiotic nebula. In 1964, V1016 Cyg underwent a nova-like outburst. Since then its brightness was slowly fading from its peak $V \sim 10.6$ mag (1967 - 1970) to $V \sim 11.4$ mag (2016) (McCuskey, 1965). V1016 Cyg belongs to a group of D-type symbiotics, which means, that the emission of the dust dominates the near-infrared spectrum. Although we could expect complicated structure of the dust emission in the symbiotic stars, the spectral energy distribution of the dust emission in V1016 Cyg can be in first approximation fitted by the sum of two Planck functions with different dust temperature: ~ 1040 K and 340 K, heated by both the hot component and the Mira-variable. (Fig. 1). According to Schild et al. (2001), this implies a presence of the two dust shells heated by both the hot component and the Mira-variable. However a more realistic model of dust emission comprising the chemical composition should be applied to fit also two broad silicate emission bands at ~ 10 and $18 \mu\text{m}$.

The symbiotic nebula represents a part of the circumstellar matter originated mostly in the stellar wind of the giant, ionized by the high energetic photons from the white dwarf (Seaquist et al., 1984). A certain part of the circumstellar matter around the giant is dense enough to remain neutral.

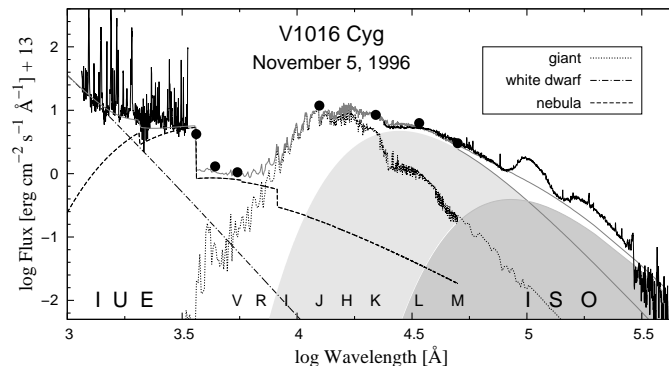


Figure 1: The observed spectral energy distribution (the IUE & ISO spectra and UVJJKLM photometry) with the models of individual sources of radiation in V1016 Cyg. The curves with filled areas represent the Planck functions corresponding to dust emission with temperature of ~ 1040 and 340 K.

Such an environment of a symbiotic star is very suitable for observing the scattering processes.

2 Thomson scattering

Thomson scattering by free electrons arises in the symbiotic nebula. Despite of its very small cross section, $\sigma_T = 6.652 \times 10^{-25} \text{cm}^{-2}$, a large amount of photons from emission lines of highly ionized elements in the vicinity of the white dwarf and a lot of free electrons throughout the nebula allow to observe the effect of electron scattering. This process is wavelength independent and the scattered photon has practically the same wavelength as before scattering (if neglecting the Compton wavelength $\sim +0.024 \text{\AA}$). A significant Doppler effect, arising from thermal motion of free electrons, produces very shallow and broad wings of the scattered emission line. To model the profile of broad wings of O VI 1032, 1038 \AA doublet we followed a simplified approach described by Castor et al. (1970). In this model a layer of free electrons of optical thickness τ_e and temperature, T_e , separated from line forming region (located in a vicinity of the hot star) and other opacity sources, is irradiated by the line photons. The line profile after scattering can be approximated by:

$$\Psi(x) = (1 - \tau_e) \Phi(x) + \tau_e \int_{-\infty}^{\infty} \Phi(x') R_e(x', x) dx', \quad (1)$$

where $\Phi(x)$ is the line profile before scattering, R_e is the redistribution function for Thomson scattering, assuming Maxwellian distribution of free electron velocities and isotropic scattering (Mihalas, 1970) and x or x' is the

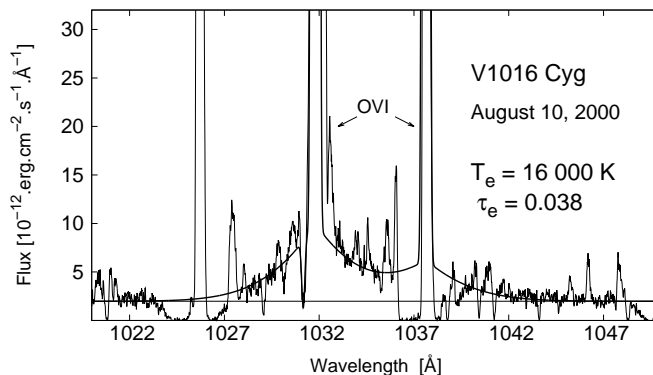


Figure 2: The model of broad O VI emission line wings (thick line) arising from Thomson scattering in the symbiotic nebula.

frequency displacement from the line center in units of electron Doppler width before and after the scattering, respectively. From the best model of O VI 1032, 1038Å line profile we determined $\tau_e = 0.038$ and $T_e = 16\,000$ K of the scattering layer of free electrons, i.e. the symbiotic nebula (Fig. 2). The value of T_e is consistent with temperatures observed in other symbiotic stars during their quiescent phases. Modeling is described in detail by Sekeráš & Skopal (2012).

3 Raman scattering

Unlike the Thomson scattering, the Raman scattering takes place in the neutral part of the giant's wind. It occurs when a photon excites an atom from its ground state to an intermediate state and subsequently a photon of different frequency is re-emitted. A diagnostic possibility of Raman scattering in astrophysics was first outlined by Nussbaumer et al. (1989). The most famous example of Raman scattering in symbiotic stars are broad emission features at 6825 and 7082Å, which are formed by scattering of O VI 1032 and 1038Å emission lines on the neutral hydrogen atoms (Schmid, 1989). We can observe also Raman scattered emission of those spectral lines, which are close lying to the hydrogen emission lines of Lyman series.

According to Lee et al. (2003) we analyzed the emission feature at 6545Å, which is the Raman scattered He II 1025Å emission line, in two spectra of V1016 Cyg observed in April, 2006 and July, 2007. We isolated Raman 6545Å feature from blending broad H α line wings and N II 6548Å emission line by approximating their composite profiles with sum of Gaussian functions (Fig. 3). We compared the FWHM of Raman feature with He II 6527 and 6560Å emission lines in the radial velocity scale, assuming they are similar in the profile with the parental He II 1025Å line. The linewidth of 6545Å feature is larger by ≈ 20 km s $^{-1}$. This additional broadening can be caused by the Doppler effect produced by the motion of neutral hydrogen atoms in

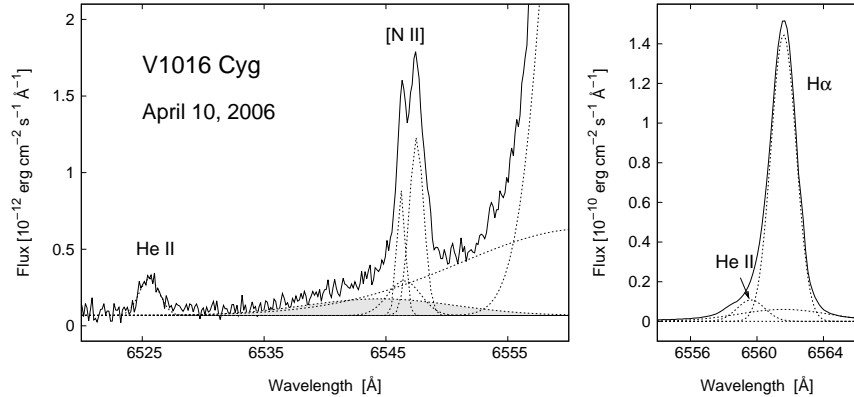


Figure 3: **Left:** The Raman emission feature (filled area) blended with the N II 6548 Å emission line and broad H α wings. **Right:** He II 6560 Å emission line blended in H α line core. Dotted lines represent the Gaussian functions approximating individual emission lines/features

the giants wind relative to He II region. Using theoretical line ratios of observed He II 1025 and 6560 Å emission lines relative to He II 4686 Å line, we determined the efficiency of 1025 Å \rightarrow 6545 Å conversion (the ratio of Raman scattered photons to all He II 1025 Å line photons) to 10.2% and 14.8% for 2006 and 2007 spectrum respectively. The fact, that only 60% of He II 1025 Å photons entering the H I region around the giant are Raman scattered (Lee, 2000), allows us to estimate the covering factor of Raman scattering zone, which is a fraction of the sky, seen from He II zone covered by the scattering region. It can be expressed via a solid angle, corresponding to the plane angle θ_R between the binary axis and the direction from the white dwarf, in which the neutral hydrogen column density, $N_{\text{H}} = 1.24 \times 10^{21} \text{cm}^{-2}$. Within this angle the region of neutral hydrogen is optically thick for investigated Raman scattering, i.e. the optical depth is greater or equal to unity (the scattering cross section is $\sim 8 \times 10^{-22} \text{cm}^2$ (Lee & Lee, 1997)).

In order to determine the mass loss rate, \dot{M} , from the Mira-variable, we used the simplified model of the ionization structure of a symbiotic star (Seaquist et al., 1984). In this model the ionization boundary between the neutral and ionized part of the circumstellar matter (we consider only hydrogen atoms), has cone-like shape and is defined by the parameter X_{H^+} or by the viewing angle θ_a from the hot star (Fig. 4). Since $X_{\text{H}^+} \propto \dot{M}^{-2}$, we determined the relation between the parameter X_{H^+} and the angle θ_R for specific properties of V1016 Cyg to obtain X_{H^+} . Then the angle θ_R from the Raman scattering efficiency gives the parameter X_{H^+} and hence \dot{M} (for detail see Sekeráš & Skopal (2015)). In this way we determined $\dot{M} = 2.0 \times 10^{-6} M_{\odot} \text{yr}^{-1}$ and $2.7 \times 10^{-6} M_{\odot} \text{yr}^{-1}$ from the spectrum observed in 2006 and 2007, respectively. The corresponding ionization structure is shown in Fig. 4.

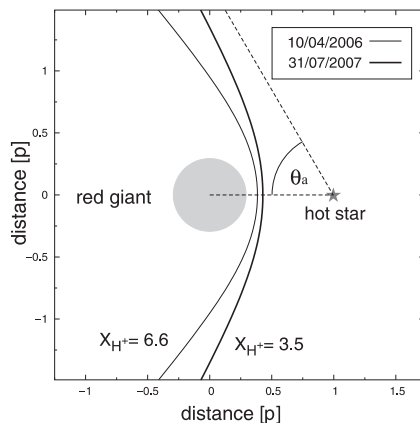


Figure 4: The ionization structure of V1016 Cyg from Raman scattering efficiency of $1025\text{\AA} \rightarrow 6545\text{\AA}$ conversion. The distance is in units of binary separation p and θ_a is the asymptotic angle to the ionization boundary.

4 Discussion

The used model of Thomson scattering was applied also to spectra of symbiotic stars *Z And* and *AG Dra* (Sekeráš & Skopal, 2012). The electron temperature was consistent with results obtained with different methods (e.g. Skopal, 2005). From analysis of broad wings of O VI 1032, 1038Å and He II 1640Å emission lines in spectra of *AG Dra* it was shown, that both parameters, T_e and τ_e , reflects the activity phase of the star (Sekeráš & Skopal, 2012; Skopal et al., 2009). The derived T_e for V1016 Cyg is consistent with the value of 17 000 K obtained from modeling the spectral energy distribution (Fig. 1).

In our model of V1016 Cyg the difference $\Delta\theta = \theta_a - \theta_R$ is very small ($< 0.5^\circ$). This is valid for massive mass loss rates of $\sim 10^{-6} M_\odot \text{yr}^{-1}$ and a large value of the Raman scattering cross section. Thus we could simply assume $\theta_R = \theta_a$. However, e.g. for Raman scattering of O VI 1032 and 1038Å photons on neutral hydrogen atoms, the cross section is of two orders smaller than for scattering of He II 1025Å photons (Lee & Lee, 1997) and limiting N_H for optically thick region for Raman scattering is $\sim 10^{23} \text{cm}^{-2}$. In this case $\Delta\theta$ can be significantly higher and should be taken into account in determining a correct value of \dot{M} .

5 Conclusion

In the environment of the symbiotic star V1016 Cyg we can observe the effects of scattering processes, resulting from the interaction between two stars of very different nature. We introduced two of them that can help to determine basic parameters of this symbiotic star. By modeling the broad wings of O VI 1032 and 1038Å emission lines we determined T_e and τ_e of

the symbiotic nebula and by investigating Raman emission feature at 6545\AA we determined \dot{M} of the Mira-variable. The used method of determining the mass loss rate from the Raman scattering, although simplified, can be helpful to inspect a possible dependence of \dot{M} on the pulsation phase of the Mira variable in V1016 Cyg. The great advantage is that the scattering efficiency can be derived just from the optical spectrum.

Acknowledgements The research was supported by a grant of the Slovak Academy of Sciences: VEGA 2/0008/17

References

- Castor, J. I., Smith L. F., van Blerkom D., 1970, ApJ, 159, 1119
- Lee, K. W., Lee H.-W., 1997, MNRAS, 292, 573L
- Lee H.-W., 2000, ApJL, 541, L25
- Lee H.-W., Sohn, Y.-J., Kang, Y. W., Kim, H.-I. 2003, ApJ, 598, 553
- Mc Cuskey, S. 1965, IAUC. No. 1916
- Mihalas, D. 1970, Stellar Atmospheres (San Francisco:W. H. Freeman), p. 321
- Nussbaumer, H., Schmid, H. M., Vogel, M. 1989, A&A, 211, L27
- Schild H., Eyers, S. P. S., Salama, A., Evans, A., 2001, A&A, 378, 146
- Schmid H. M., 1989, A&A, 211, L31
- Seaquist, E. R., Tylor A. R., Button S., 1984, ApJ, 284, 202
- Sekeráš , M. & Skopal, A., 2012, MNRAS, 427, 979
- Sekeráš , M. & Skopal, A., 2015, ApJ, 812, 162
- Skopal, A. 2005, A&A, 440, 995
- Skopal, A., Sekeráš, M., González-Riestra, R., Viotti, R. F. 2009, A&A, 507, 1531

Properties of the Wind Outflow from the Cool Components in Symbiotic Binaries

Natalia Shagatova and Augustin Skopal

Astronomical Institute of the Slovak Academy of Sciences,
Tatranská Lomnica, Slovakia

Mass outflow from the majority of cool components in symbiotic binaries is still not understood well mainly due to unknown mechanism of the wind acceleration for the normal red giants. Here, we present the wind velocity profiles derived from measured column densities of neutral hydrogen for two S-type symbiotic systems, EG And and SY Mus. The obtained velocity profiles represent an important restriction for the theoretical models of mass outflow from red giants in symbiotic binaries. Moreover, our column density models provide an indication of the wind focusing towards the orbital plane in S-type symbiotic binaries. Wind velocity profiles can be used to investigate the origin of the asymmetric UV light-curve profiles of the symbiotic stars. The asymmetric distribution of the absorption as indicated in the H α line-profile along the orbital phase, observed in the symbiotic star EG And, is the problem that can be addressed with our column density model in future investigation.

Key Words: symbiotic stars - stellar wind - mass-loss - scattering

1 Introduction

With respect to the evolutionary stage of the cool companion, providing the wind matter to be transferred onto the white dwarf accretor of a symbiotic system, a particular mass-loss mechanism is driving the giant's wind. In the case of the Mira-type donor in D-type systems, the physical mechanism of the wind outflow is quite well understood. As in the AGB stars generally, the wind is driven by the radiative acceleration of dust grains that can be formed by levitation of the wind matter through pulsations of the star (e.g. Höfner, 2015). However, for the normal red giants (RGs) in S-type systems, the mass-loss mechanism is unknown. Numerous models for the wind-driving mechanism from RG stars were proposed, but non of them is in agreement with observations (O'Gorman et al., 2013).

To make a progress in this direction, the knowledge of the wind velocity profile is one of the basic requirements. While the canonical β -law can be used to describe the winds of the hot stars, it is not appropriate in the case

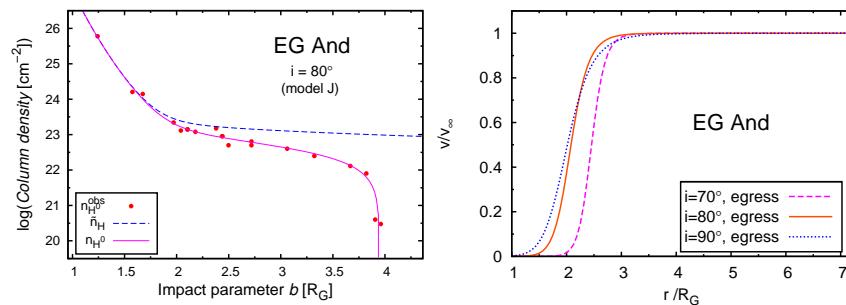


Figure 1: Example of the column density model (left) and resulting wind velocity profiles for EG And (right) from Shagatova et al. (2016). R_G is the radius of RG.

of cool star winds with steeper measured velocity profiles (e.g. Crowley & Espey, 2010; Decin et al., 2015). For RGs in symbiotic stars EG And and SY Mus, we derived the wind velocity profiles at the near-orbital plane by hydrogen column density modelling. We used them to model the asymmetric light curves of SY Mus and to determine the orbital inclination of symbiotic prototype Z And.

2 Velocity profiles of the wind

The wind velocity profile of a RG in symbiotic binary can be derived by hydrogen column density modelling using the inversion method of Knill et al. (1993). We improved the method by including the ionization structure of the wind according to Seaquist et al. (1984). In this way, we were able to separate the H^0 column density $n_{H^0}(b)$, from the total hydrogen column density $\tilde{n}_H(b)$,

$$\tilde{n}_H(b) = \frac{n_1}{b} + \frac{n_K}{b^K}, \quad (1)$$

where b is the impact parameter and n_1 , n_K , K are fitting parameters.

Accordingly, we fitted the H^0 column density values $n_{H^0}^{obs}$, measured from the Rayleigh attenuation around the Ly- α line in the International Ultraviolet Explorer (IUE) and Hubble Space Telescope (HST) spectra, by the $n_{H^0}(b)$ function (see Fig. 1, left, and Eq. (13) of Shagatova et al., 2016). We used the method of Knill et al. (1993) to derive the wind velocity profile $v(r)$ in the form:

$$\frac{v(r)}{v_\infty} = \frac{1}{1 + \xi r^{1-K}}, \quad (2)$$

where v_∞ is the terminal velocity of the wind, $\xi = (n_K \lambda_1)/(n_1 \lambda_K)$, λ_1 and λ_K are the eigenvalues of the Abel operator (see Knill et al., 1993). The details of the method and resulting values of parameters in Eqs. (1), (2) and of the ionization parameter for several values of the orbital inclination for EG And and SY Mus can be found in Shagatova et al. (2016). Corresponding velocity profiles show a very low wind velocity up to the distance of ≈ 1 RG

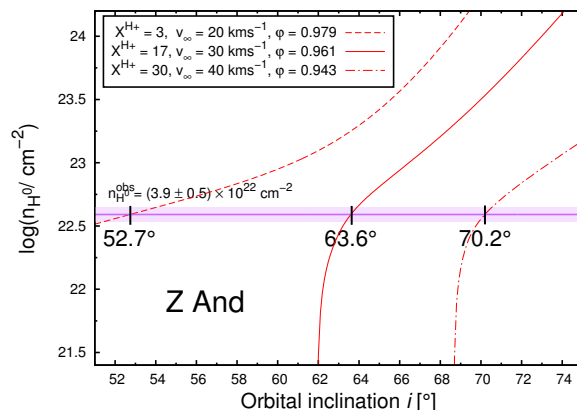


Figure 2: The H^0 column density dependence on the orbital inclination, plotted for different values of ionization parameter X^{H^+} , terminal velocity v_∞ and orbital phase φ (in the legend). The corresponding values of i are given by the intersection of the $n_{H^0}(i)$ curves with the horizontal line representing the measured value of H^0 column density at $\varphi = 0.961$. The horizontal strip corresponds to the uncertainty of the measured H^0 column density.

radius from the giant’s surface and then a very steep increase to the value of the terminal velocity (see Fig. 1, right).

3 Wind focusing towards the orbital plane

Our column density model assumes spherical symmetry of the wind distribution. As our column densities correspond to the specific directions, i.e. the line of sight is crossing the near-orbital plane for eclipsing binaries, we actually derived the spherical equivalent of the mass-loss rate, $\dot{M}_{sp} \approx 10^{-6} M_\odot \text{yr}^{-1}$. This approach revealed a discrepancy between our values of \dot{M}_{sp} for appropriate terminal velocities of the wind from RGs in symbiotic stars, and the typical value of the total mass-loss rate $\approx 10^{-7} M_\odot \text{yr}^{-1}$ obtained by the methods independent on the line of sight (e.g. Seaquist et al., 1993; Skopal, 2005). This result indicates that the spherical symmetry of the RG wind does not hold in S-type symbiotic binaries and the wind density is enhanced at the near-orbital-plane region (Shagatova et al., 2016).

4 Orbital inclination of Z Andromedae

Z Andromedae is the prototype of symbiotic systems. However, the values of its orbital inclination i that can be found in the literature are often contradictory and vary from approximately 41° to 76° (e.g. Isogai et al., 2010; Skopal, 2003). We used the H^0 column density modelling at $\varphi = 0.961$ to derive the orbital inclination of Z And. To match the value of i measured

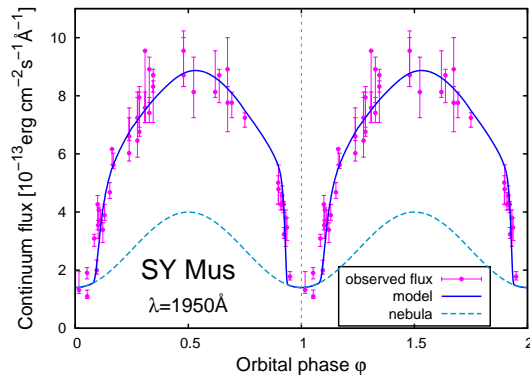


Figure 3: Example of the light curve model at $\lambda = 1950 \text{ \AA}$ (adapted from Shagatova & Skopal, 2017). Vertical dotted line corresponds to the orbital phase of the inferior conjunction of the giant.

from Rayleigh attenuation around the Ly- α line, we calculated the $n_{\text{H}^0}(i)$ integral for a set of the values of ionization parameter X^{H^+} , terminal velocity and orbital phase φ , within their uncertainties (Fig. 2). By including also the uncertainty of the H^0 column density, $n_{\text{H}^0}^{\text{obs}} = (3.9 \pm 0.5) \times 10^{22} \text{ cm}^{-2}$, measured from Rayleigh scattering, we obtained the resulting interval of inclinations:

$$i = 66.3^\circ - 12.2^\circ / + 6.9^\circ. \quad (3)$$

The method is described in detail in Skopal & Shagatova (2012). The updated value of i (Eq. (3)) corresponds to the velocity profile (2) for $\xi = 1.81 \times 10^4$ and $K = 13$, as derived for the giant in SY Mus (model O of Shagatova et al., 2016), which is of the same spectral type as that in Z And.

5 Asymmetric light-curve modelling

The light curves of some symbiotic systems show an asymmetry of their ingress and egress parts, and in the position of minima/maxima (see e.g. Skopal et al., 2012). For SY Mus, Dumm et al. (1999) proposed that the asymmetric distribution of the material from the RG wind is the cause of the asymmetric UV eclipse profile of this system. We tried to justify this assumption in a quantitative way.

For the purpose of modelling the UV light curves of SY Mus, we determined continuum fluxes at 10 wavelengths from 1280 to 3080 \AA using IUE spectra. We assumed two sources of radiation in the UV domain: the white dwarf radiation that we approximated by a Planck function, and the nebular radiation, approximated by a scaled sine wave along the orbital motion, with a minimum at $\varphi = 0$. As a sources of attenuation of the stellar radiation, we assumed the Rayleigh scattering on neutral hydrogen and the bound-free transitions of the negative hydrogen ion in neutral region. In the

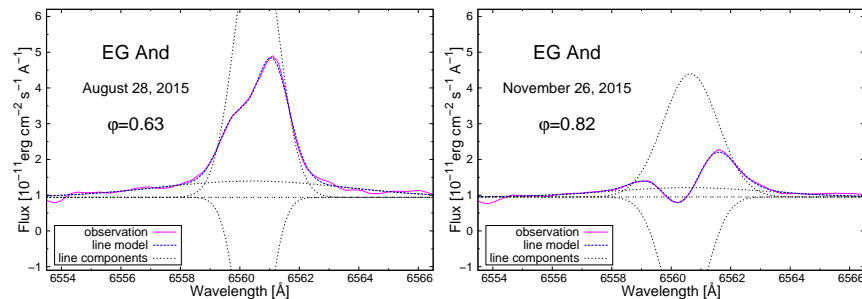


Figure 4: Comparison of $H\alpha$ line profile in the spectrum of EG And at two orbital phases. Observed $H\alpha$ -line is fitted by three Gaussian components.

ionized region, we assumed the Thomson scattering on free electrons and the bound-free and free-free transitions of neutral hydrogen.

To determine the column densities of attenuating atoms/ions, we used the velocity profiles derived from ingress and egress data of SY Mus for $i = 84^\circ$ (i.e. the model M and O of Shagatova et al., 2016). We interconnected them by a smooth function to obtain the united asymmetric model of ionization structure and column densities of H^0 in neutral region and H^+ in ionized region.

Overall, the model light curves reproduce successfully the asymmetry in the observed profiles (see example for $\lambda = 1950 \text{ \AA}$ in Fig. 3). Therefore, the cause of the asymmetry in the light curves of SY Mus is the asymmetric wind density distribution at the plane of observations.

6 Future outlook

Our velocity profiles (Sec. 2) can be used to solve various problems of S-type symbiotic stars. One of them is the understanding of the orbital variations of the $H\alpha$ -line profile of EG And. Fig. 4 shows examples of $H\alpha$ -line profiles at $\varphi = 0.63$ and $\varphi = 0.89$. The model $H\alpha$ -line profile is just a fit of the observed profile by three Gaussian functions: one for the core emission, second one for the broad wing emission and third one for the absorption. With the orbital phase towards eclipse, the absorption component becomes stronger.

To model these orbital variations, we can use the spectra of EG And obtained at Stará Lesná Observatory and those available at the Astronomical Ring for Access to Spectroscopy (ARAS) database¹, together with our wind velocity profiles. Then, we can determine the amount of matter along the line of sight that shapes the absorption component of the $H\alpha$ line at each orbital phase.

¹http://www.astrosurf.com/aras/Aras_DataBase/Symbiotics/EGAnd.htm

7 Conclusion

By modelling the observed H^0 column density distribution of symbiotic stars EG And and SY Mus, we determined the corresponding total hydrogen column densities in the form of Eq. (1) and their wind velocity profiles in the form of Eq. (2). These results allowed us to indicate the focusing of the RG wind towards the orbital plane and to justify that the asymmetry of the UV continuum light curves of SY Mus is caused by the asymmetric wind density distribution at the plane of observations. Further, using the column density model, we obtained the orbital inclination of Z And. In future, our approach can be used to model the orbital variations of the absorption and emission component of the $H\alpha$ line in symbiotic star EG And to probe the distribution of circumstellar matter in the binary.

Acknowledgements This research was supported by a grant of the Slovak Academy of Sciences, VEGA No. 2/0008/17, and by the Slovak Research and Development Agency under the contract No. APVV-15-0458.

References

- Crowley, C. & Espey, B., 2010, ASP Conf. Ser. (Editors: C. Lietherer, P. Bennett, P. Morris, J. van Loon), 425, 191
- Decin, L., Richards, A. M. S., Neufeld, D., Steffen, W., Melnick, G., Lombaert, R., 2015, A&A, 574, A5
- Dumm, T., Schmutz, W., Schild, H., Nussbaumer, H., 1999, A&A, 349, 169
- Höfner, S., 2015, ASP Conf. Ser. (Editors: F. Kerschbaum, R. F. Wing, J. Hron), 497, 333
- Isogai, M., Seki, M., Ykeda, Y., Akitaya, H., Kawabata, K.S., 2010, AJ, 140, 235
- Knill, O., Dgani, R., Vogel, M., 1993, A&A, 274, 1002
- O’Gorman, E., Harper, G. M., Brown, A., Drake, S., Richards, A. M. S., 2013, AJ, 146, 98
- Seaquist, E. R., Taylor, A. R., Button, S., 1984, ApJ, 284, 202
- Seaquist, E. R., Krogulec, M., Taylor, A. R., 1993, ApJ, 410, 260
- Shagatova, N., Skopal, A., Cariková, Z., 2016, A&A, 588, A83
- Shagatova, N., Skopal, A., 2017, A&A (submitted)
- Skopal, A., 2003, A&A, 401, L17
- Skopal, A., 2005, A&A, 440, 995
- Skopal, A. & Shagatova, N., 2012, A&A, 547, A45
- Skopal, A., Shugarov, S., Vaňko, M., et al., 2012, AN, 333, No. 3, 242

Reclassifying Symbiotic Stars with 2MASS and WISE: An Atlas of Spectral Energy Distribution

Akras Stavros¹, Guzman-Ramirez Lizette², Leal-Ferreira Marcelo², and Ramos-Larios Gerardo³

¹Observatório Nacional/MCTIC, Rio de Janeiro, Brazil

²Leiden Observatory, Leiden University, Netherlands

³Instituto de Astronomía y Meteorología, Mexico

We present a new updated catalogue of Galactic and extragalactic symbiotic stars (SySts). Since the last catalogue of SySts (Belczynski et al. 2000), the number of known SySts has significantly increased. Our new catalogue contains 316 known and 82 candidates SySts. Of the confirmed SySts 252 are located in our Galaxy and 64 in nearby galaxies. This reflects an increase of $\sim 50\%$ in the population of Galactic SySts and $\sim 400\%$ in the population of extragalactic SySts. The spectral energy distribution (SED) of 334 (known and candidates) SySts have been constructed using the 2MASS and WISE data. These SEDs are used to provide a robust reclassification in scheme of S- (74%), D- (15%) and D⁺-types (2.5%). The SEDs of S- and D-type peak between 0.8 and 1.6 μm and between 1.6 and 4 μm , respectively, whereas those of D⁺-type exhibit a plateau profile. Moreover, we provide the first compilation of SySts that exhibit the OVI Raman-scattered line at 6830Å. Our analysis shows that 55% of the Galactic SySts exhibit that line in their spectrum, whereas this percentage is different from galaxy to galaxy.

Key Words: symbiotic stars - classification - catalogues

1 Introduction

Symbiotic stars (SySts) are interacting, long-period, binary systems consisting of a cool red giant star that transfer matter to a much hotter companion, usually a white dwarf but it is also possible to be a neutron star or black hole. The atmosphere of the red giant or its wind are excited by the UV radiation from the white dwarf resulting in the formation of a colourful nebula. Their spectrum consists of both absorption features due to the photosphere of the cool companion and a number of emission-lines from highly-excited ions due to the surrounding nebula.

SySts represent ideal objects for investigating and studying several as-

trophysical phenomena such as the formation of aspherical circumstellar envelopes and high-velocity jets, dust forming regions, colliding winds, the interaction of binary components and their evolution, mass transfer processes, accretion disks, soft and hard-X rays emission (e.g. Mikolajewska 2012; Luna et al. 2013, Skopal & Cariková 2015; Mukai et al. 2016). They have also been proposed as potential progenitors of type Ia supernova (SN Ia) due to the large amount of masses that the white dwarf accretes from the cold companion resulting in exceeding the Chandrasekhar mass ($1.4 M_{\odot}$) and exploding as a SN Ia (e.g. Di Stefano 2010; Dilday et al. 2012). Hence, the interest in SySts has been gradually increasing the last decades and many attempts are being made to discover new SySts either in our Galaxy or other galaxies in the Local Group.

Based on their near-IR 2MASS colours, SySts are divided into two main categories near-infrared data: (i) those with a near-IR colour temperatures of ~ 3000 - 5000 K, which attributed to the temperature of a G-, K- or M-type giant (stellar or S-type SySts), and (ii) those with a near-IR colour temperature around 700 - 1000 K, indicating a warm dusty circumstellar envelope (dusty or D-type SySts) (Webster & Allen 1975).

The identification of an object as SySts is made based on a number of widely used criteria: (i) the presence of strong He II and H I emission lines as well as emission lines from high-excitation ions (ionization potential, $I.P. \geq 35$ eV), (ii) the presence of absorption features of TiO and VO associated with the photosphere of the cold companion and (iii) the presence of the OVI Raman-scattered line centred at 6830 \AA (e.g. Lee 2000; Belczyński et al. 2000; Mikolajewska et al. 2014).

More effort has been invested in developing a more general way of distinguishing SySts from other strong $H\alpha$ emitters (e.g. genuine PNe, H II regions, WR stars, Be stars etc.). In the optical regime, Gutierrez-Moreno et al. (1995) proposed a diagnostic diagram between $[\text{O III}] 4363/H\gamma$ vs. $[\text{O III}] 5007/H\beta$ emission line ratios, which reflects on the different densities between PNe and SySts (see e.g. Clyne et al. 2015). Recently, Corradi et al. (2008) proposed a new diagnostic diagram based on the IPHAS $r-H\alpha$ vs. $r-i$ colour indices.

SySts are also important X-ray sources. Based on their X-ray spectrum, they are divided into four types: (a) the supersoft X-ray sources with energies ≤ 0.4 keV probably emitted directly from the white dwarf (α -type), (b) the objects that exhibit a peak at 0.8 keV in their X-ray spectrum and maximum energies up to 2.4 keV, likely originate from a hot, shocked gas where the stellar winds collide (β -type), (c) the objects with a non-thermal emission and energies higher than 2.4 keV (γ -type) due to the accretion of mass onto the hot companion (white dwarf or neutron stars) and (d) those with very hard X-ray thermal emission and energies higher than 2.4 keV likely originate from the inner regions of an accretion disk (δ -type; Muerstet et al. 1997; Luna et al. 2013).

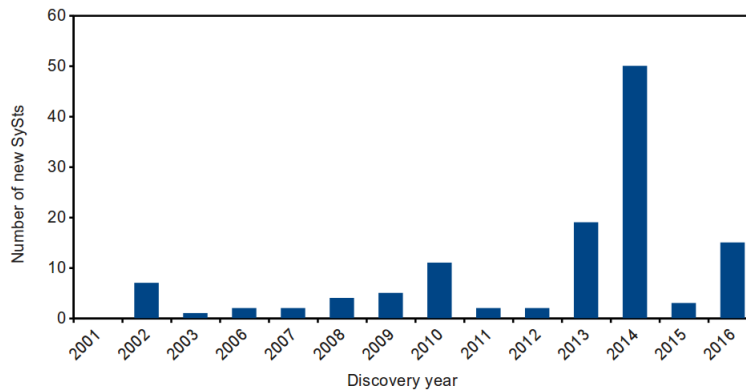


Figure 1: The number of SySts discoveries per year between 2000 and 2016.

2 Sample selection

The most complete and comprehensive compilation of SySts was published by Belczyński and collaborators 16 years ago (Belczyński et al. 2000). This catalogue includes all the known Galactic and extragalactic SySts (188) as well as a number of 30 candidates SySts. The histogram in Figure 1, shows the number of new SySts discoveries per year the last 16 years. Of the 316 confirmed SySts, 252 are Galactic and 64 are extragalactic. This implies an increase of $\sim 50\%$ and $\sim 400\%$ in the population of Galactic and extragalactic SySts since the publication of Belczyński’s catalogue (2000). Besides new discoveries, the total number of SySts still remains very low compared to the expected number of SySts in our Galaxy, which varies between 3×10^3 (Allen 1984) and 4×10^5 (Magrini et al. 2003). Nevertheless, the number of SySts is expected to significantly increase over the next years due to the on-going surveys like VPHAS+ (Drew et al. 2014), J-PAS/J-PLUS (Benitez et al. 2014) and S-PLUS (Mendez de Oliveira et al. in prep.).

3 Spectral energy distribution

According to Ivison et al. (1995), spectral energy distribution of SySts peaks between 1 and $2\mu\text{m}$ for the S-type, 5 - $15\mu\text{m}$ for the D-type and at longer wavelengths between 20 and $30\mu\text{m}$ for the D’-type SySts. Therefore, it is coherent to construct and study the SEDs of SySts using both the 2MASS and WISE data providing a more robust classification.

In Figure 2, we display two examples for each type of SySts (S-, D- and D’-type). The SED of S-type is dominated by the cool companion and those of D-type by the emission of dust. We performed a statistical analysis that shows the SED of the S-type peak between 0.8 and $1.6\mu\text{m}$, D-type 1.6 and $5\mu\text{m}$, whereas those of D’-type SySts show a plateau profile within the wavelength range covered by 2MASS and WISE. We also find a statistically significant number of SySts with a clear S-type profile plus

an infrared excess at 11.6 and/or 22.1 μ m (see Fig. 2). We, thus, propose a fourth type of SySts, namely S+IR excess. A further study on this type of SySts is required in order to understand whether it consists a new type between the S- and D-type SySts. Figure 3 shows the percentages as well as the population of known and candidate SySts for each type based on our preliminary classification.

4 OVI Raman scattered line 6830Å

One of the criteria to classify an object as SySt is the detection of the line features centred at 6830Å and 7088Å (Belczynski et al. 2000). These two broad lines are interpreted as the result of Raman scattering of the ultraviolet OVI $\lambda\lambda$ 1032,1038 resonance lines by neutral hydrogen (Schmid 1989). Allen (1980) pointed out that 50% or more of SySts exhibit these Raman lines even before their identifications. However, this analysis should be further explored since the sample contains only a few SySts.

Therefore, the first compilation of SySts that show the OVI Raman-scattered line λ 6830 in their spectrum is presented in the current catalogue. We find that 55% of the Galactic SySts (119 out of 218 with available optical spectra) show the OVI λ 6830 line very close to what found by Allen (1980). Examining the detection of the OVI Raman line in different type, we find no difference between S- (58%) and D-types (54%), whereas only 8 out of 21 S+IR excess type (38%) and one out of four D'-type (25%) show the Raman line.

Given that the number of confirmed extragalactic SySts has increased, we are able now to perform a similar analysis in four nearby galaxies. In particular, we find that all eight known SySts in the SMC show the Raman line (100%), whereas only four out of seven in the LMC (57%). As for the M31 and M33 galaxies, 16 out of 31 SySts in the M31 (51%, Mikolajewska et al. 2014) and 5 out of 12 SySts in the M33 (41%, Mikolajewska et al. 2017) show the Raman line in their spectra. This implies that galaxies have different percentages probably due to different physical conditions such as the metallicity parameter. However, these sample contains very few SySts and this results has to be further explored in the future when the sample have a statistically significant number of SySts.

Moreover, looking carefully at the spectra of the SySts in M31 and M33 (Mikolajewska et al. 2014,2017), we also find a clear trend between the OVI λ 6830 Raman line and He II λ 4686. When the latter line is detected the former is also detected, the opposite is not true and the flux ration between the two line is $F_{OVI}/F_{He\ 4686} \sim 0.5$.

Acknowledgements I would like to thank the organizing committee for the opportunity to attend this event and present this work as well as for their financial support. S.A. and M.L.L.-F. also acknowledge support of CNPq, Conselho Nacional de Desenvolvimento Científico e Tecnológico - Brazil (grant 300336/2016-0 and 248503/2013-8 respectively).

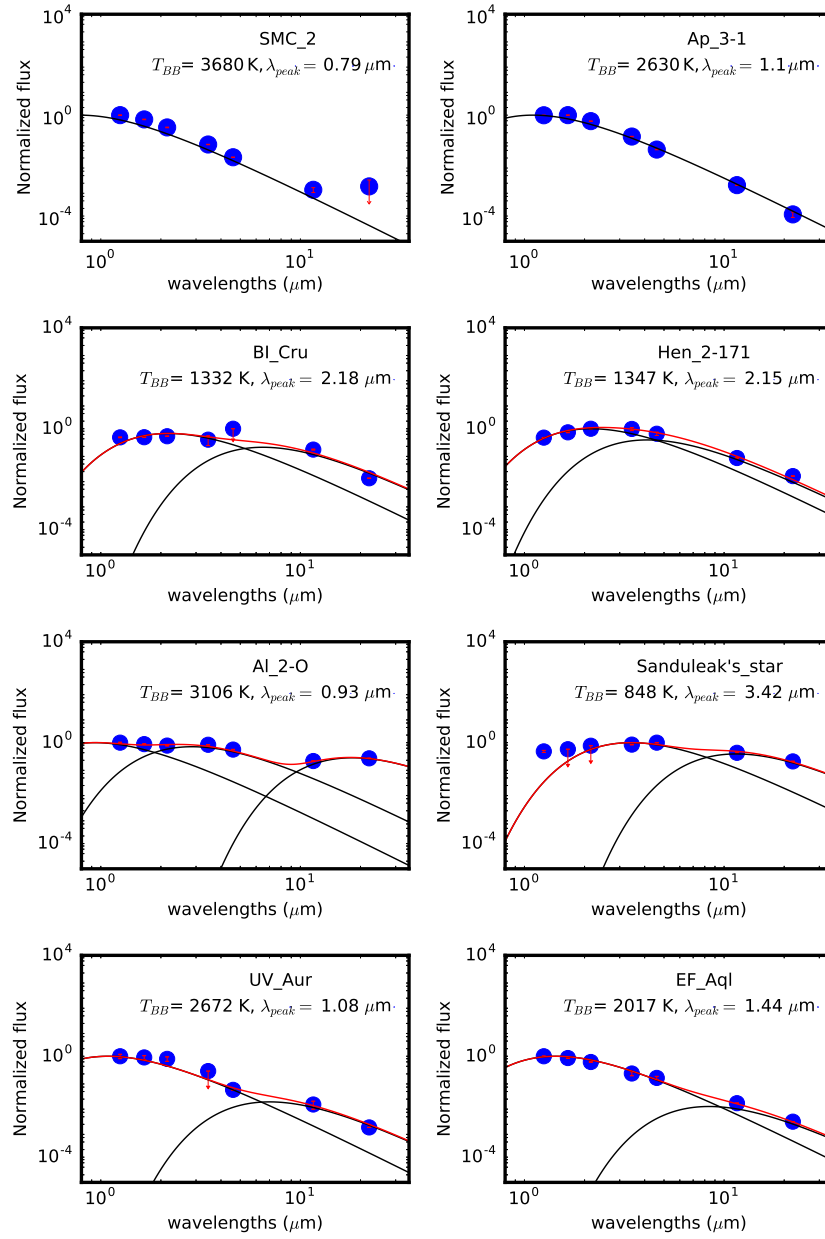


Figure 2: Examples of SEDs for two S- (first line), D- (second line), D'- (third line) and S+IR-type (fourth line) SySts.

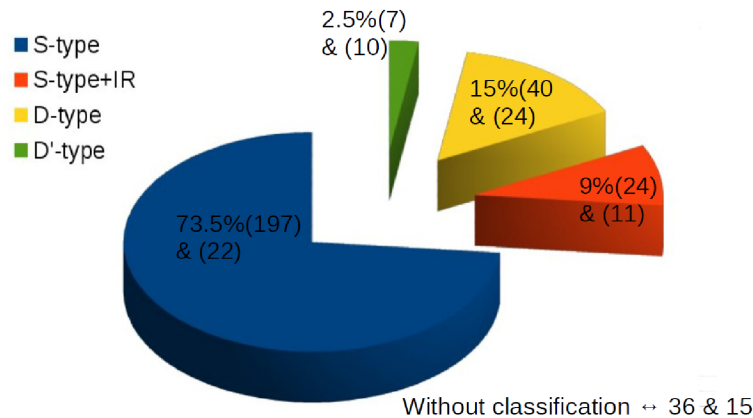


Figure 3: Pie chart of the new classification of SySts. Numbers in parenthesis give the exact population of known and candidate SySts in each type. The 12 new SySts discoveries in M33 are not included.

References

- Allen D. A., 1980, MNRAS, 190, 75
 Allen D. A., 1984, PASAu, 5, 369
 Belczyński K., et al., 2000, A&AS, 146, 407
 Benítez N., et al., 2014, 2014arXiv1403.5237B
 Clyne N., Akras S., Steffen W., et al., 2015, A&A, 582
 Corradi R. L. M., et al., 2008, A&A, 480, 409
 Dilday B., Howell D. A., Cenko S. B., et al., 2012, Sci, 337, 942
 Di Stefano R., 2010, ApJ, 719, 474
 Drew J. E., et al., et al., 2014, MNRAS, 440, 2036
 Gutiérrez-Moreno A., Moreno H., Costa E., 1999, PASP, 111, 571
 Hee-Won L., 2000, ApJ, 541, 25
 Ivison R. J., et al., 1995, MNRAS, 273, 517
 Luna G. J. M., Sokoloski J. L., Mukai K., Nelson T., 2013, A&A, 559, 6
 Magrini L., Corradi R. L. M., Munari U., 2003, ASPC, 303, 539
 Mikolajewska J., 2012, BaltA, 21, 5
 Mikolajewska J., Caldwell N., Shara M. M., 2014, MNRAS, 444, 586
 Mikolajewska J., Shara M. M., Caldwell N., et al., 2017, MNRAS, 465, 1699
 Muerset U., Wolff, B., Jordan, S. 1997, A&A, 319, 201
 Mukai K., Luna G. J. M., Cusumano G., et al., 2016, MNRAS, 461, 1
 Schmid H. M., 1989, A&A, 211, 31
 Skopal A., Čariková Z., 2015, A&A, 573, 8
 Webster B. L., Allen D. A., 1975, MNRAS, 171, 171

Accretion in Young and Evolved Stars

W.J. de Wit¹, A. Caratti o Garatti², and S. Kraus³

¹European Southern Observatory, Santiago, Chile

²Dublin Institute of Advanced Studies, Dublin, Ireland

³Astrophysics Group, University of Exeter, Exeter, UK

A compact overview is presented of disk accretion among stars with an emphasis on proto-planetary disks. Recent observational discoveries related to the character of mass accretion in young high-mass stars are highlighted. These discoveries are compared to disks and accretion in main sequence stars and evolved stars, like post-AGB, classical Be, and sgB[e] stars.

Key Words: young stars - evolved stars - accretion

1 Introduction

A general definition of accretion is the following (Myriam-Webster): *"a gradual process in which layers of a material are formed as small amounts are added over time"*. In astrophysics, adding material to an object (a planet, star or black hole) releases gravitational potential energy. This is the source of many interesting astrophysical phenomena which are discussed in the contributions to this first Chile-Korea-Gemini workshop on accretion in symbiotic stars and related objects. Our contribution focuses on accretion and disks in young stars with an eye on disk bearing and accreting stars beyond the formation stage. Mass exchange and accretion in compact binaries and symbiotic stars are discussed elsewhere in these proceedings.

2 Accretion in young stars

The time of accretion in the formation of stars covers loosely a main accretion phase and a residual accretion phase. The main accretion phase is earlier, relatively short in time, and delivers the bulk of the star's mass. This process takes place when a molecular core has evolved a self-luminous, coherent object at its centre and which continues to grow by accreting material from a protostellar disk. The disk material is supplied by the in-falling core. How the core collects its mass, or what the boundary conditions are for star formation in a molecular cloud is still open to debate (André et al. 2014).

During the main accretion phase, the infall of envelope material onto the disk will likely influence the ability of the disk to transport angular momentum and therefore the mass flux through the disk. Several disk processes result in angular momentum transport. They depend on the mass, magnetic field strength, and ionization fraction of the disk (*viz.* gravitational torques, disk winds, MRI, see Hartmann et al. 2016). On the other hand, the envelope's infall rate is determined by the core's angular momentum and mass. The infall and accretion processes are related (continues infall secures continues disk accretion) but distinct. In the main accretion phase, the envelope dominates the spectral energy distribution which renders the observational access to the disk difficult in the near and mid-IR and impossible at shorter wavelengths. Recent ALMA studies address the formation of the disk within the core (Aso et al. 2015). Most of our understanding of disk accretion in young stars comes therefore from the residual accretion phase during the pre-main sequence (PMS).

3 Disks in different evolutionary phases

For low and intermediate mass PMS stars whose internal stellar structure evolves relatively slow, the disk remains present and continues accreting during the star's contraction towards the main sequence. In detail, material is lifted up from the disk and deposited onto the star by means of magnetic funnels (e.g. Bessolaz et al. 2008). The field guides the material which subsequently free-falls onto the star (Hartmann et al. 2016). This picture does not necessarily apply to objects accreting at high rates. The evolution of the disk towards depletion takes place on a 10 Myr timescale as delineated from the drop in dust emission in stars with different ages (Wyatt 2008). The exact longevity of circumstellar disks and accretion is however debated, fed by examples of long-lived, gaseous disks (Beccari et al. 2015) and the retention and the transition to collisionally processed dusty material (e.g. de Wit et al. 2013). For more massive stars ($> 8M_{\odot}$), the star settles on the main sequence before accretion has terminated and before the envelope is dispersed. The formation phase of a massive star will end by stellar feedback processes rather than accretion/infall regulated processes. It is for this reason that accretion processes in massive stars are comparatively difficult to observe as the complete formation takes place behind closed curtains (Beltrán & de Wit 2016).

Alternative information on the nature of disks around luminous stellar objects can be gleaned from evolved objects, e.g. the rare supergiant B[e] stars (de Wit et al. 2014). For the dusty sgB[e]s, interferometric observations indicate that most disks are circumbinary. The densities in the disk are sufficient for molecule and dust grain formation, providing kinematics and spatially resolved geometries with optical interferometers. To the best of our knowledge, no direct detection (emission lines, UV excess) of accretion in sgB[e]s has been reported. Among the approximately fifteen known sgB[e]s (Kraus 2009), one object exhibits indirect evidence of on-going accretion

as traced by an extended and collimated 1.7pc jet advancing at projected velocities up to 450 km s^{-1} (MWC 137, Mehner et al. 2016). The jet shows knots and is strikingly similar to that of accreting low-mass stars. The authors evaluate six scenarios explaining the presence of accretion in this evolved object, e.g. due to binary mass exchange, or a merger event.

Classical Be stars are able to launch stellar material into orbit owing to conspiring radial pulsation and rapid stellar rotation. The gaseous disk is tenuous and largely ionized and evolves viscously (Rivinius et al. 2013). Although no direct evidence for accretion in classical Be stars exist, once the star stops losing mass the torque exerted at the inner rim of the disk vanishes and disk material can be re-accreted. The radial flow of material (in or out) can be traced photometrically thanks to the different wavelength dependence between optically thin (large radii) and optically thick (small radii) Bremsstrahlung (de Wit et al. 2006). No jets by the re-accretion of gas in Be stars are reported.

Dusty disks are created in advanced evolutionary stages of about half of the low and intermediate mass stars owing to mass-loss in wide binaries. The disks in (post-)AGB stars are in Keplerian rotation, circumbinary and compact (Hillen et al. 2016). The disk allows departure from spherical symmetry in the geometry of nascent Planetary Nebulae. Feeding circumstellar disks, it also allows accretion activity producing jets in PNe (Reyes-Ruiz & López 1999). Symbiotic stars, being wide giant-white dwarf binary systems ($P > 12$ hours), have this feat in common with the disk bearing (post-)AGBs. The jet in Sanduleak's star lends itself for an analogy with on-going strong wind-fed accretion (Perets & Kenyon 2013) in, at least some, symbiotic stars, especially those for which the white dwarf is moving through the optically thick and dusty envelope of a donor post-AGB star (Angeloni et al. 2011).

4 Accretion in high-mass star formation

4.1 Circumbinary and two circumstellar disks

In recent years, two important advances in high-mass star formation have been established: (1) numerical simulations show that radiative pressure does not impede disk accretion (Kuiper et al. 2010); (2) about 80% of the O-type stars are multiple systems (Chini et al. 2012). Given that fact, proper understanding of the high-mass star disk evolution involves envisaging the accretion flow as part of a complex binary - disk - envelope system. In this respect, we would like to make the rough comparison with the wind-fed disk of the hot white dwarf companion experiencing the headwind of the red giant wind that may or will distort the geometry of the "accretion flow", depending on momenta involved (see e.g. Walder et al. 2008).

Spectro-interferometric observations with AMBER and Gravity at the VLT Interferometer revealed that the massive YSO IRAS17216-3801 is a compact high-mass protobinary. The binary has a separation of 57.9 ± 0.2 mas (170 au, see Fig. 1). The data allowed to reconstruct a synthesis image at the spatial resolution of the interferometer of 3 mas. The masses of the

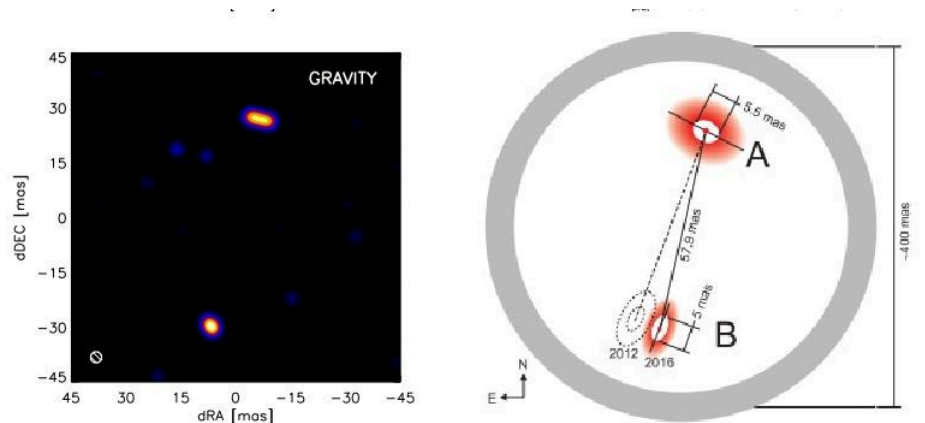


Figure 1: *Left:* The K-band synthesis image reconstructed from VLTI observations with the Gravity instrument of the massive YSO system IRAS17216-3801. *Right:* The cartoon detailing the interpretation of the image as two high-mass stars each with a disk, while the protobinary system is surrounded by a circumbinary disk. Figures from Kraus et al. (2017).

binary components was derived to be $\sim 20M_{\odot}$ and $\sim 18M_{\odot}$. The YSO system is significantly more massive ($\sim 3x$) and compact than previously known accreting massive binary systems. This is the first high-mass protobinary system where circumstellar and circumbinary dust disks could be imaged (Kraus et al. 2017). Similar results will be forthcoming with the full deployment of Gravity and the other 2nd generation VLTI instrument MATISSE, operating in the mid-IR.

4.2 An accretion burst

With the reliability and technical advances of IR and mid-IR detectors over the years, phenomena in the time domain at these wavelength bands become now possible (e.g. Contreras Peña et al. 2017). That young low-mass stars exhibit accretion driven bursts of continuum emission has been known for many years. Such bursts are likely caused by disk fragmentation and subsequent migration of dense clumps onto the protostar. The magnetic funnel guiding the disk material onto the star probably breaks down because of the increased pressure of the disk.

Yet, the existence of accretion bursts in higher mass, embedded objects has only recently been established (Caratti o Garatti, 2017). In the case of the massive YSO S255 – IRS3 ($\sim 20 M_{\odot}$), the burst was first detected owing to increased emission in methanol maser lines. Near-IR imaging established the brightening of the central source and the outflow lobes (Fig. 2). The spectral fingerprint of the emission is comparable to that of a low-mass source in outburst. The total energy release derived from the change in the spectral energy distribution is four orders of magnitude larger than the

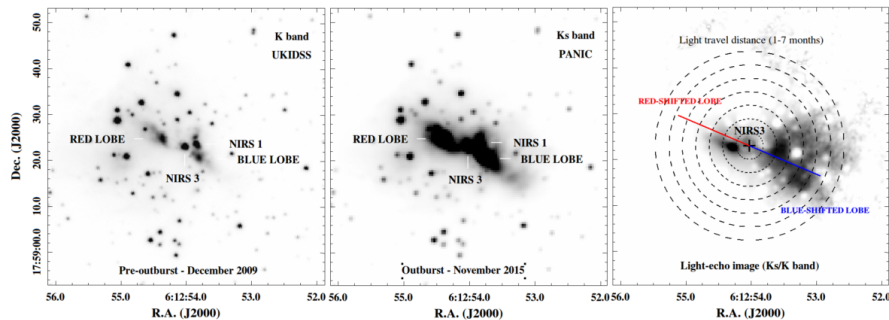


Figure 2: K-band images of the S255 region. *Left*: Pre-outburst December 2009. *Middle*: Outburst (November 2015), showing the brightening of NIRS 3 and its outflow cavities. *Right*: Ratio image. The gradual increment of brightness ratio towards the centre indicates a light echo. Concentric circles mark light travel distances in the plane of the sky separated by one month. Figures from Caratti o Garatti et al. (2017).

energy release in low-mass star bursts. The discovery allows the team to estimate unambiguously a mass accretion rate larger than $6 \times 10^{-3} M_{\odot} \text{ yr}^{-1}$. These observations show clearly that stars in this mass range grow by means of disk accretion and that accretion is not a stable process (Caratti o Garatti et al. 2017).

5 Summary and concluding remarks

We have provided a very brief overview of accretion during the protostellar and pre-main sequence phases of young stars. Given the challenges in determining the character of the wind-fed disk surrounding the white dwarf in symbiotic systems, we highlighted observational diagnostics and physical situations in star formation that might find analogies in such systems. In particular, it could be investigated more thoroughly whether the observed variability (photometric, spectroscopic) in symbiotics could be related to the white dwarf disk rather than the inhomogeneities in the red giant mass-loss and/or the orbital parameters.

Acknowledgements

The authors would like to thank the organizers for a splendid and informative workshop.

References

- André, P., Di Francesco, J., Ward-Thompson, D., Inutsuka, S.-I., Pudritz, R. E., & Pineda, J. E. 2014, *Protostars and Planets VI*, 27
- Angeloni, R., Di Mille, F., Bland-Hawthorn, J., & Osip, D. J. 2011, *ApJ*, 743, L8
- Aso, Y., Ohashi, N., Saigo, K., Koyamatsu, S., Aikawa, Y., Hayashi, M., Machida, M. N., Saito, M., Takakuwa, S., Tomida, K., Tomisaka, K., & Yen, H.-W. 2015, *ApJ*, 812, 27
- Beccari, G., De Marchi, G., Panagia, N., Valenti, E., Carraro, G., Romaniello, M., Zoccali, M., & Weidner, C. 2015, *A&A*, 574, A44
- Beltrán, M. T., & de Wit, W. J. 2016, *A&A Rev.*, 24, 6
- Bessolaz, N., Zanni, C., Ferreira, J., Keppens, R., & Bouvier, J. 2008, *A&A*, 478, 155
- Caratti o Garatti, A., et al. 2017, *Nature, Physics*, in press, doi:10.1038/nphys3942
- Chini, R., Hoffmeister, V. H., Nasserri, A., Stahl, O., & Zinnecker, H. 2012, *MNRAS*, 424, 1925
- Contreras Peña, C., et al. 2017, *MNRAS*, 465, 3039
- de Wit, W. J., Grinin, V. P., Potravnov, I. S., Shakhovskoi, D. N., Müller, A., & Moerchen, M. 2013, *A&A*, 553, L1
- de Wit, W. J., Lamers, H. J. G. L. M., Marquette, J. B., & Beaulieu, J. P. 2006, *A&A*, 456, 1027
- de Wit, W. J., Oudmaijer, R. D., & Vink, J. S. 2014, *Advances in Astronomy*, 2014, 270848
- Hartmann, L., Herczeg, G., & Calvet, N. 2016, *ARA&A*, 54, 135
- Hillen, M., Van Winckel, H., Menu, J., Manick, R., Debosscher, J., Min, M., de Wit, W.-J., Verhoelst, T., Kamath, D., & Waters, L. B. F. M. 2016, *ArXiv e-prints*. 1610.09930
- Kraus, M. 2009, *A&A*, 494, 253
- Kraus, S., Kluska, J., Kreplin, A., Bate, M., Harries, T. J., Hofmann, K.-H., Hone, E., Monnier, J. D., Weigelt, G., Anugu, A., de Wit, W. J., & Wittkowski, M. 2017, *ApJ*, 835, L5
- Mehner, A., de Wit, W. J., Groh, J. H., Oudmaijer, R. D., Baade, D., Rivinius, T., Selman, F., Boffin, H. M. J., & Martayan, C. 2016, *A&A*, 585, A81
- Perets, H. B., & Kenyon, S. J. 2013, *ApJ*, 764, 169
- Reyes-Ruiz, M., & López, J. A. 1999, *ApJ*, 524, 952
- Rivinius, T., Carciofi, A. C., & Martayan, C. 2013, *A&A Rev.*, 21, 69
- Walder, R., Folini, D., & Shore, S. N. 2008, *A&A*, 484, L9
- Wyatt, M. C. 2008, *ARA&A*, 46, 339

Poster Session

SDSS J122339.61-005631.1: A Short Period Eclipsing Binary with a White Dwarf Component

Saker, L.^{1,2}, Lovos, F.^{1,2}, Petrucci, R.P.^{1,2}, Jofré, J.E.^{1,2}, & Gómez, M.^{1,21}

¹Observatorio Astronómico, Universidad Nacional de Córdoba, Argentina (OAC)

²Consejo Nacional de Investigaciones Científicas y Técnicas (CONICET, Argentina)

SDSS J122339.61–005631.1 (hereafter SDSS J1223–0056) is a detached short period ($P = 2.1$ h) post-common envelope eclipsing binary, formed by a white dwarf plus a main-sequence star. In this work, we present new optical photometry of SDSS J1223–0056, obtained with the 2.15 m Jorge Sahade telescope at the Complejo Astronómico El Leoncito (CASLEO, Argentina). This system, as well as others containing a white dwarf component, are being observed with the aim of detecting eclipsing time variations (ETVs). In this contribution, we report a new initial analysis of this binary system. In addition, we perform an ETV analysis combining our time of eclipse with those previously reported.

Key Words: binaries: close - binaries: eclipsing - stars: white dwarfs - stars: individual: SDSS J122339.61–005631.1

1 Introduction

Post-Common-Envelope-Binary (PCEB) systems have typical orbital periods between 2 hours and 2 days, although the great majority of them are closer to the lower boundary. In recent years, the number of eclipsing binaries with a white dwarf component has increased, mainly due to large surveys such as the Sloan Digital Sky Survey (York et al., 2000, SDSS) and the Catalina Sky Survey (Drake et al., 2009, CSS). SDSS J122339.61–005631.1 (hereafter SDSS J1223–0056) was identified as a binary system by Raymond et al. (2003). Table 1 lists the stellar parameters determined by Rebassa-Mansergas et al. (2007, 2010, 2012a) as well as the orbital ephemeris obtained by Parsons et al. (2013). SDSS J1223–0056 is composed of a white dwarf (WD) plus a main-sequence (MS) stars. In this contribution, we present new observations and a preliminary analysis of this system.

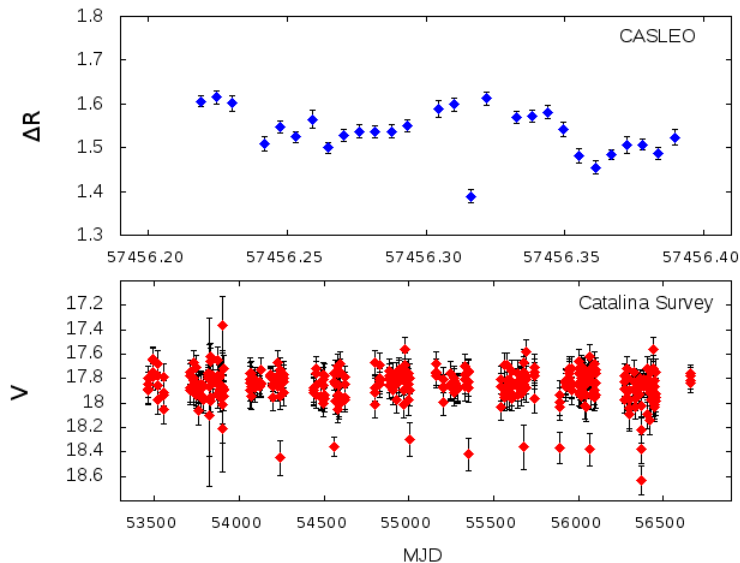


Figure 1: (Top panel) Light curve of SDSS J1223–0056 obtained at CASLEO. (Bottom panel) Light curves of SDSS J1223–0056, from the CSS database.

2 Observations

2.1 Light Curve

We present new optical photometry of SDSS J1223–0056, obtained the night of March 8, 2016, with Roper 2048×2048 pixels CCD, attached to the 2.15 m Jorge Sahade telescope at the Complejo Astronómico El Leoncito (CASLEO, Argentina). The field covered was $5.1' \times 5.1'$. During the observation, the Johnson R filter was used and the exposure time was 5 min, with a dead-time between exposures of 30 sec. To obtain differential magnitudes with aperture photometry, we used an algorithm called FOTOMCC (Petrucci et al., 2013, 2015), a quasi-automatic pipeline which uses the DAOPHOT package, from the IRAF environment. We complemented our observations with the CSS light curves. In Figure 1, top panel, we present the differential light curve obtained at CASLEO. Although it was possible to detect a time of minimum, SDSS J1223–0056 has a partial eclipse that only lasts a few minutes (Parsons et al., 2013; Pyrzas et al., 2015). For future observations, we plan to reduce the exposure time to improve the cadence of observations. In the bottom panel of Figure 1, we show the light curve from the CSS, obtained with an exposure time between 5 and 40 sec.

3 Analysis

3.1 Ephemeris and O–C diagram

Using the time of mid-eclipse from the CASLEO light curve, as well as those from the CSS and those reported in the thesis of M. C. P. Bours (2015), we calculated the orbital ephemeris of the system. A linear ephemeris was derived using a least-squares approach to minimize the residuals: $T = T_o + P_{\text{orb}} \times E$, where P_{orb} is the orbital period of the binary in days, T_o is the time at which the cycle number $E=0$, and T is the time of a given orbital cycle E . Figure 2, upper panel, shows the O–C diagram for this system. We detected no significant periodicity in the O–C values but found two points that are outside the standard deviation. We re-calculated the ephemeris discarding these points. Therefore, the best linear ephemeris obtained is $T[\text{MJD}] = 55707.0141(46) + 0.09007811(49)E$, where the numbers in brackets indicate the error on the last two digits. As before, no significant periodicity in the O–C diagram was apparent.

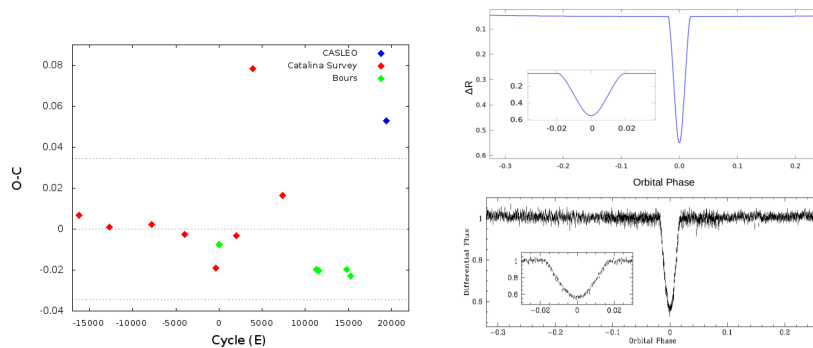


Figure 2: (Upper panel) Observed-Computed (O–C) versus Cycle. Dashed lines indicate $\pm 3\sigma$. CASLEO, CSS, and Bours data of SDSS J1223–0056 are shown as blue, red and green diamonds, respectively. (Middle panel) synthetic light curve generated with the W-D code, using the parameters listed in Table 1. (Bottom panel) g' filter light curve of SDSS J1223–0056 obtained by Pyrzas et al. (2015). Insert panel: a zoom around the eclipse.

References: 1) Rebassa-Mansergas et al. (2010), 2) Parsons et al. (2013), 3) stellar parameters used to generate the synthetic light curve of SDSS J1223–0056, shown in Figure 2 middle panel.

3.2 Synthetic light curve obtained with the W-D code

We generated a synthetic light curve with the LC subroutine of the Wilson-Devinney (W-D) code (Wilson & Devinney, 1971), using the stellar parameters of Table 1. We obtained a light curve (middle panel of Figure 2) that is quite similar to that presented by Pyrzas et al. (2015), showed in the bottom panel of Figure 2. We plan to continue the systematic monitoring of SDSS J1223–0056, covering several orbital periods. This will allow us

Table 1: Stellar parameters of SDSS J1223–0056 and the orbital ephemeris of the system

Parameter	Value	References
M_{WD} [M_{\odot}]	0.45 ± 0.06	1
T_{WD} [K]	11565 ± 59	1
R_{WD} [R_{\odot}]	0.01549 ± 0.00107	1
Spectral-Type $_{WD}$	DA	1
Spectral-Type $_{MSstar}$	M6	1
Orbital Period [hr]	2.1618720 ± 0.0000003	2
T_o [MJD]	55707.0169865(72)	2
R_{WD} [R_{\odot}]	0.06	3
q	0.44	3
e	0	3
i [°]	83.9	3
Orbital Period [hr]	2.1624	3
s-m axis [R_{\odot}]	0.733	3

to derive a well-covered light curve to be adjusted with the DC subroutine of the W-D code. The parameters listed in Table 1 should provide a good starting solution to be refined with the DC subroutine.

4 Conclusions

In this contribution, we present new optical photometry of SDSS J1223–0056, obtained at the CASLEO. We re-determined the orbital ephemeris of the system, complementing our observations with the CSS light curves and the nine mid-eclipse times presented in the thesis of M. C. P. Bours (2015). We did not detect any significant periodicity in the O–C values (Figure 2).

Finally, we generated a synthetic light curve with the W-D code, quite similar to that presented by Pyrzas et al. (2015), show in the bottom panel of Figure 2. We plan to continue the systematic monitoring of SDSS J1223–0056, covering several orbital periods. This will allow us to derive a well covered light curve to be adjusted with the DC subroutine of the W-D code. The parameters listed in Table 1 should provide a good starting solution to be refined with the DC subroutine.

References

- Bours, M. C. P. 2015 in Thesis presented at the University of Warwick, Department of Physics
- Drake, A. J., et al., 2009, ApJ, 696, 870
- Parsons, S. G., et al., 2013, MNRAS, 429, 256
- Petrucci R., et al., 2013, ApJL, 779, L23

- Petrucci R., et al., 2015, MNRAS, 446, 1389
Pyrzas S., et al., 2015, MNRAS, 447, 691
Raymond S. N., et al., 2003, AJ, 125, 2621
Rebassa-Mansergas, A., et al., 2007, MNRAS, 382, 1377
Rebassa-Mansergas, A., et al., 2010, MNRAS, 402, 620
Rebassa-Mansergas, A., et al., 2012a, MNRAS, 419, 806
Wilson, R. E., & Devinney, E. J. 1971, ApJ, 166, 605
York, D. G., et al., 2000, AJ, 120, 1579

OVI 6830Å Imaging Polarimetry of Symbiotic Stars

Akras Stavros¹

¹Observatório Nacional/MCTIC, Rio de Janeiro, Brazil

I present here the first results from an ongoing pilot project with the 1.6 m telescope at the OPD, Brasil, aimed at the detection of the OVI λ 6830 line via linear polarization in symbiotic stars. The main goal is to demonstrate that OVI imaging polarimetry is an efficient technique for discovering new symbiotic stars. The OVI λ 6830 line is found in 5 out of 9 known symbiotic stars, in which the OVI line has already been spectroscopically confirmed, with at least 3σ detection. Three new symbiotic star candidates have also been found.

Key Words: symbiotic stars - polarization

1 Introduction

Raman scattering is a well established mechanism in symbiotic stars (Schmid 1989; Nussbaumer et al. 1989). Generally, two broad lines are detected in symbiotic stars (SySts) centred at 6830Å and 7088Å, with the latter being approximately 4 times weaker. These two lines are attributed to Raman scattering of the ultraviolet OVI $\lambda\lambda$ 1032, 1038 resonance lines by neutral hydrogen (Schmid 1989; Nussbaumer et al. 1989). Of the confirmed Galactic SySts 252 or 55% (Akras et al. these proceedings) show the broad OVI λ 6830 Raman-scattered line (Allen 1980; Schmid & Schild 1994).

The mechanism of Raman scattering is well known to produce strong polarization from a few percent up to 10-15% (Schmid & Schild 1994; Harries & Howarth 1996,2000). Spectro-polarimetric observations are very important for determining the orbital parameters for these systems as well as the mass-loss rate of the cold giant by studying the O VI line profiles (Harries & Howarth 1997). However, only a few of them have been systematically observed. Hence, an OVI λ 6830 imaging polarimetric survey of SySts is required in order to unveil those with significant polarization.

In this paper, I present the first OVI 6830Å imaging polarimetric observations of SySts. This pilot project aims to pave the way for larger and systematic OVI surveys (imaging photometry and/or polarimetry) searching for new SySts without necessarily obtain follow-up observations.



Figure 1: OVI $\lambda 6830$ line image of RR Tel taken with the IAGPOL at position angle of the prism of 0 degree. The two stars in the red circle refer to the real and imaginary part of RR Tel. North is up, east to the left.

2 Observations

Linear imaging polarimetric observations were obtained with the $1.6 \mu\text{m}$ Perkin-Elmer telescope at the Observatório do Pico dos Dias (OPD/LNA) in Brasil. The data were taken using the imaging polarimeter Instituto de Astronomía, Geofísica e Ciências Atmosféricas polarimeter (IAGPOL; Magalhães et al. 1996). The polarimeter consists of a half-wave plate that can be rotated in steps of 22.5 degrees and a Savart calcite prism (Ramírez et al. 2015). The broad-band filter R and a narrowband filter centred at 6810\AA (100\AA bandwidth) were used with exposure times between 5 and 240 s. The field of view and image scale are 12 arcmin^2 and $0.36 \text{ arcsec pixel}^{-1}$, respectively. During observations, the seeing varied between 1.5 and 2 arcsec. Fig. 1 shows an image of RR Tel obtained with the OVI λ filter.

Separate images were obtained for both filters and at relative position angles of the prism of 0, 22.5, 45, 67.5, 90, 112.5, 135, 157.5 and 180 degrees. The instrumental polarization as well as the rotation angle of the polarimeter were estimated by observing a number of unpolarized and polarized standard stars during the campaign. The data reduction was performed by using the IRAF package BEACON pipeline. The code applies a standard reduction technique which includes, removal of cosmic rays, subtraction of the dark current and bias, as well as flat-field normalization. It calculates the degree of polarization (DoP) and position angle (PA) for several stars in the field.

Table 1: Degree of linear polarization of SySts.

Name	O VI [†] (6830Å)	P _{OVI} (%)	P _R (%)	P _{ISM,OVI} (%)	P _{ISM,R} (%)
<i>RR Tel</i>	yes	3.09±0.13	0.58±0.02	0.42±0.03	0.45±0.02
<i>Hen 2-106</i>	yes	4.19±0.20	3.02±0.03	2.21±0.02	2.13±0.01
<i>CD-43 14304</i>	yes	0.65±0.03	0.22±0.01	0.53±0.02	0.28±0.01
<i>AR PAV</i>	yes	1.30±0.03	1.16±0.02	0.61±0.01	0.61±0.01
<i>2MASS16422739</i>	yes	9.32±3.07	4.79±0.06	1.91±0.01	1.71±0.01
BI Cru	no	1.04±0.03	1.07±0.06	1.33±0.02	1.26±0.02
HD 330036	no	2.79±0.06	2.66±0.02	2.06±0.02	2.01±0.01
Hen 3-1213	no	2.82±0.20	3.04±0.14	2.01±0.01	2.10±0.01
Hen 3-1761	no	1.00±0.02	1.01±0.02	0.97±0.01	0.98±0.01
V4018	no	0.35±0.03	0.40±0.02	0.50±0.01	0.51±0.01
V4074	yes	1.15±0.07	1.05±0.33	1.18±0.02	1.25±0.01
Hen 3-1341	yes	1.89±0.05	1.75±0.14	2.01±0.01	2.04±0.01
StHa 164	yes	2.47±0.13	2.58±0.17	2.58±0.01	2.66±0.02
PN K 3-12	yes	0.95±0.17	0.75±0.13	0.92±0.02	0.93±0.01

[†] Spectroscopic detection of the OVI λ 6830 Raman-scattered line.

3 Results

In narrowband polarization imaging there are three components that have to be taken into account, (i) the polarization in spectral line, (ii) the polarization in the continuum and (iii) the interstellar medium polarization (ISP). For a positive detection of the spectral line via polarization imaging, the continuum and ISP components have to be measured and properly subtracted. For the continuum polarization, the broadband filter R was used.

Regarding the ISP, the field star method was used (e.g. Akras et al. 2017). Assuming that the field stars are unpolarized, the average DoP from all the stars in the field gives a rough estimate of the ISP.

Table 1 presents the DoP in the OVI and R filters for 14 known SySts (Belczyński et al. 2000, Akras et al. these proceedings) as well as the ISP in the direction of each object (5th and 6th columns). Two criteria were used in order to get a positive detection of the OVI Raman line, (i) $P_{\text{OVI}} > P_{\text{ISM,OVI}} + 3 \times \sigma_{P_{\text{OVI}}}$, which implies the star is intrinsically polarized in the OVI line and (ii) $P_{\text{OVI}} > P_{\text{R}} + 3 \times \sigma_{P_{\text{OVI}}}$, which implies that the observed polarization is due to the spectral line and not the continuum. In some cases, the target can be highly polarized in the continuum (R) but not necessarily in the spectral line (e.g. Hen 3-1213).

In my sample, there are nine SySts in which the presence of OVI λ 6830 Raman line had been confirmed spectroscopically before and five SySts without a confirmed detection. I get a 3σ detection for 5 (*italic* in Table 1) out of 9 SySts with previous OVI detection. The non detection of the OVI line from the last four SySts may be due to the variation of the line (very faint

OVI line at the time of my observations). As for the five SySts, without a confirmed detection, I get no detection for all of them (100% success).

Besides the SySts, I have also found three stars that pass the aforementioned criteria and I have considered them as candidate SySts. Since this is a pilot project, follow-up spectroscopic observations of these three candidates are required in order to unveil their nature and confirm the power of this technique.

4 Conclusion

OVI 6830Å imaging polarimetry seems to be very promising technique for searching new SySts. 5 out of 9 SySts (56%) show a 3σ detection of the OVI Raman line. The detection of the OVI Raman line via polarimetry assures the symbiotic nature of the object without following-up observations. More observation of SySts, with or without a confirmed detection of the OVI line, are planned to be obtained this year.

Acknowledgements I would like to thank the organizing committee for the opportunity to attend this event and present this work as well as for their financial support. I also acknowledge support of CNPq, Conselho Nacional de Desenvolvimento Científico e Tecnológico - Brazil (grant 300336/2016-0). This work is based upon observations carried out at the Observatório do Pico dos Dias (LNAMECT/CNPq, Brazópolis, Brazil). Many thanks also to Nikos Nanouris for reviewing this paper.

References

- Akras S., Ramirez-Velez J. C., Nanouris N., et al. 2017, MNRAS, 466, 2948
- Allen D. A., 1980, MNRAS, 190, 75
- Belczyński, K., et al., 2000, A&AS, 146, 407B
- Harries T. J., Howarth I. D., 1996, A&AS, 119, 61
- Harries T. J., Howarth I. D., 1997, A&AS, 121, 15
- Harries, T. J.; Howarth, I. D., 2000, A&A, 361, 139
- Kenyon S. J., Livio M., Mikolajewska J., Tout C. A., 1993, ApJ, 407, L81
- Magalhães A. M., et al., 1996, Astronomical Society of the Pacific Conference Series, 97, 118
- Magalhães A. M., Benedetti E., Roland E. H., 1984, PASP, 96, 383
- Magrini L., Corradi R. L. M., Munari U., 2003, ASPC, 303, 539
- Munari U., Renzini A., 1992, AJ, 397, 87
- Nussbaumer H., Schmid H. M., Vogel M., 1989, A&A, 211, 27
- Ramírez Edgar A., et al. , 2015, arXiv151209085
- Schmid H. M., 1989, A&A, 211, 31
- Schmid H. M., Schild H., 1994, A&A, 281, 145

Flux Ratios of Raman Scattered O VI Features in Symbiotic Stars

Young-Min Lee and Hee-Won Lee

Department of Physics and Astronomy, Sejong University
Seoul, Korea

Being a wide binary system of an accreting white dwarf and a mass losing giant, symbiotic stars are an important stellar system to study the late stage of stellar evolution. The giant component suffers a heavy mass loss in the form of a slow stellar wind resulting in accretion onto the white dwarf through gravitational capture. Broad spectral emission features at 6825 and 7082 are known to be unique to symbiotic stars, formed from O VI λ 1032 and 1038 through Raman scattering with atomic hydrogen. These Raman features are an excellent tool to probe the wind accretion in symbiotic stars. We perform Monte Carlo simulations to compute the flux ratio of 6825 and 7082 formed in a neutral region with a geometric shape of a slab, cylinder and sphere by varying the neutral H I column density along a specified direction. In the optically thin limit $N_{HI} \leq 10^{22} \text{ cm}^{-2}$ the flux ratio F_{6825}/F_{7082} reflects the ratio of cross sections, which is around 3 when we inject the same number of OVI 1032 and 1038 photons. The ratio tends to converge to unity in the optically thick limit $N_{HI} \geq 10^{24} \text{ cm}^{-2}$. In the column density around 10^{23} cm^{-2} where Raman scattering optical depth approaches unity, flux ratio changes in a complicated way due to nonlinear dependence of the scattering number on N_{HI} . In the case of a neutral slab illuminated by an O VI source outside, the flux ratio in the optically thick limit is less than unity, implying a significant fraction of O VI photons escape through Rayleigh scattering near the boundary. We compare our high resolution CFHT data of HM Sge and AG Dra with the data simulated with finite cylinder models confirming that S type symbiotic tend to be characterized by a thicker HI region than D type counterparts.

Key Words: symbiotic star - radiative transfer - scattering - stars: individual (HM Sagittae, AG Draconis)

1 Introduction

Symbiotic stars consist of a compact star, mostly a white dwarf, and a giant star losing a large amount of mass in the form of a slow stellar wind. Typical values of mass loss rate exhibited by giant components in symbiotic stars

range $\dot{M} \sim 10^{-8} - 10^{-7} M_{\odot} \text{ yr}^{-1}$. A nonnegligible fraction of the slow stellar wind from the giant companion is gravitationally captured by the white dwarf because the velocity scale of the slow stellar wind is comparable to the Keplerian velocity at several AU from the white dwarf (e.g. Mikołajewska 2012). A number of hydrodynamical studies show the plausibility of an accretion disk and also some symbiotic stars are known to exhibit optical flickering indicating the presence of an accretion disk (e.g., Sokoloski et al. 2001; Sokoloski & Bildsten 2010). The size of a giant simply implies that the dynamical time scales associated with symbiotic activities may be found up to several decades.

One useful classification of symbiotic stars involves the IR spectral characteristic. Many IR studies of symbiotic stars reveal that there are two major classes depending on the presence of an IR excess. Symbiotic stars showing an IR excess are classified into a D type, where the IR excess is proposed to be indicative of a dust component with a temperature $\sim 10^3$ K (e.g. Whitelock 1987; Angeloni et al. 2010). No such IR excess is apparent in 'S' type symbiotics. The orbital periods of 'D' type symbiotics are poorly known and are presumed to exceed several decades. This implies that the giant companion is separated from the white dwarf by tens of AU. This is in high contrast in that many 'S' type symbiotics are known to have orbital periods of several hundreds of days, which points out that the giant companion is much closer to the white dwarf than their 'D' type counterparts. It is also notable that the giant component of a 'D' type symbiotic star is usually a Mira variable.

A significant fraction of symbiotic stars exhibit unique broad emission features at 6825 and 7082 Å with a width 20–30 Å. These mysterious spectral features known as 'symbiotic bands' were finally identified by Schmid (1989), who proposed that they are formed through Raman scattering of O VI $\lambda\lambda$ 1032 and 1038 with atomic hydrogen. Raman scattering proceeds with a hydrogen atom in the ground state upon which an O VI line photon is incident. The incident photon is annihilated with the excitation of the hydrogen atom in one of infinitely many p states, which will subsequently de-excite into $2s$ state with a creation of an optical photon redward of $H\alpha$. Also allowed process is a creation of an outgoing optical photon with an excitation into a p state from the ground $1s$ state followed by an annihilation of the incident photon with a de-excitation into the $2s$ state. The cross section of this process is $\sigma_{Ram,1032} = 6.6$ and $\sigma_{Ram,1038} = 2.5$.

These Raman O VI features are known to exhibit multiple peak profiles, which can be explained by associating the O VI emission region with the accretion flow around the white dwarf in a physical size of ~ 1 AU. The enhanced red peak shows that the accretion flow around the white dwarf has an asymmetric matter distribution in a way that the entering side is of higher density than the opposite side. Considering the role played by the Raman O VI features as a diagnostic of the accretion flow in symbiotic stars, studies of fundamental properties on the conversion efficiency are of importance for the proper interpretation of spectroscopic data.

2 Result: Slab, Cylinder and Sphere

We developed a Monte Carlo code to produce Raman O VI photons that are formed in a neutral region with a simple geometric figure such as slab, cylinder and sphere. In particular, we inject the same number of O VI 1032 and 1038 photons into the neutral region and collect the emergent Raman O VI photons to compute the flux ratio F_{6825}/F_{7082} . Fig. ?? summarizes our work where the top 6 panels, middle 6 panels and bottom 6 panels are for slab, cylinder and sphere geometry. The left three panels correspond to the cases where the emission source is embedded at the center of the neutral region, and the right three panels are for the case where the emission source is outside the neutral region. The horizontal axis is the logarithm of N_{HI} , where neutral column density is measured along the normal direction in the case of a slab and radial direction in the cases of a cylinder and a sphere.

In each top two panel, the horizontal dashed line indicates the ratio of Raman scattering cross sections for O VI $\lambda\lambda$ 1032 and 1038, which is 3.04. This is the flux ratio expected in a very optically thin scattering region that completely surrounds the O VI emission source. In each middle two panels, we plot the Raman conversion efficiency, where the solid and dotted curves are for Raman O VI features at 6825 and 7082 Å, respectively. Each bottom two panels show the mean scattering number. It should be noted that the minimum number of scatterings is one for Raman scattered photons due to the inelastic nature of Raman scattering. In the slab cases, the flux ratio in the optically thin limit is not convergent to the ratio of Raman scattering cross sections but remains significantly below it. It appears that the flux ratio converges to a value 2.3 for both cases. In these cases, escape through a single Rayleigh scattering can be made more readily by O VI λ 1032 photons than O VI λ 1038 ones due to the larger branching ratio into Rayleigh scattering of O VI λ 1032.

Also notable point is the flux ratio forms a broad hump peaking at 2.5 near $N_{HI} = 10^{22.5} \text{ cm}^{-2}$ in the case where the O VI source is embedded in a neutral slab. At this H I column density, the total scattering optical depth for O VI λ 1032 is near unity, whereas O VI λ 1038 remains RayleighRaman optically thin. A nonlinear behavior between the mean scattering number and NH I becomes significant for O VI λ 1032, while a linear relation prevails for O VI λ 1038.

The flux ratio approaches the ratio of Raman scattering cross sections in the low N_{HI} limit in the cylindrical neutral region shown in the middle top panels. It is noted that escape through Rayleigh scattering is almost negligible in the cylindrical neutral region. As in the case of the slab geometry with the emission source embedded, there is also a broad hump near $N_{HI} \sim 10^{22.5} \text{ cm}^{-2}$ with a peak value of 3.2. As N_{HI} increases, the flux ratio approaches unity, which implies full conversion into Raman optical photons. In the right three panels, we show our Monte Carlo result for a cylindrical neutral region illuminated by an O VI emission source. As shown in the top right panel, the flux ratio monotonically decreases from the expected optically thin limit of 3.05 to a value 0.87 as N_{HI} increases. Again in this

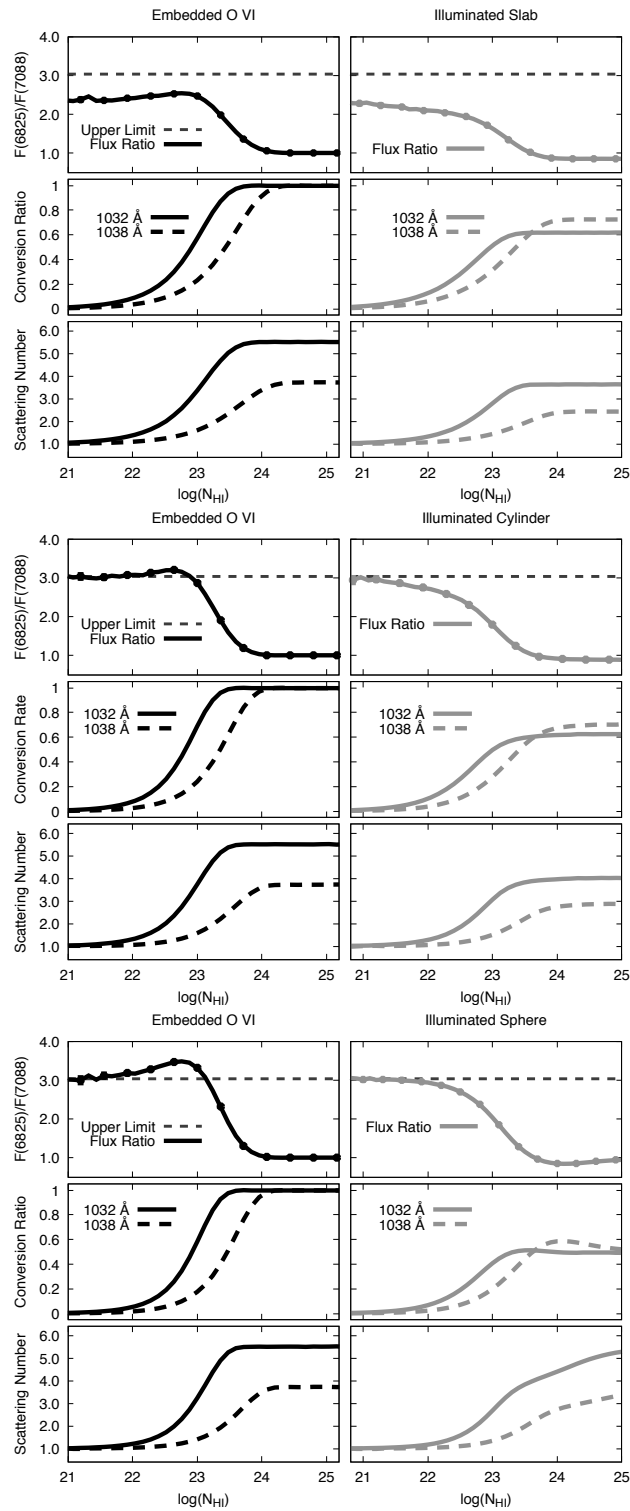


Figure 1: Flux ratio F_{6825}/F_{7082} , Raman conversion efficiency and mean scattering number of Raman scattered O VI emergent from a slab, cylinder and sphere with a embedded and illuminated cases. In this Monte Carlo calculation we inject the same number of O VI 1032 and 1038 photons.

case Rayleigh reflection occurs near the boundary region facing the O VI source, which lowers the flux ratio to 0.87 in the optically thick limit.

The last panel of Fig. ?? shows our Monte Carlo result for Raman scattered O VI formed in a spherical neutral region. In the optically thin limit, the flux ratio is convergent to the ratio of Raman scattering cross sections. In the opposite case of an extremely high optical depth, the flux ratio approaches unity, which indicates complete Raman conversion. In this figure, a particularly notable feature is the broad bump appearing at around $N_{HI} = 10^{22.7} \text{ cm}^{-2}$. The peak value is approximately 3.5, a value significantly in excess of the ratio of Raman scattering cross sections. The value of 3.5 is also the maximum flux ratio obtained in this work.

3 Comparison with CFHT spectra

Lee & Kang (2007) and Heo & Lee (2015) showed that the disparity of Raman O VI 6825 and 7082 profiles can be explained assuming an O VI emission region coinciding with a Keplerian accretion disk of velocity scale $\sim 30 \text{ km/s}$ with the entering side of enhanced density. We assume that O VI emission region is asymmetric in such a way that the entering side is significantly denser than the opposite side. We adopt a highly simplified H I region delineated by a finite cylinder specified by radius R and height H . The diameter of the neutral cylinder is set to equal the binary separation. We set $R/H = 5$.

In the bottom panels of Fig. ?? for HM Sge, simulated profiles are obtained adopting the same finite cylinder model with $N_{HI} = 10^{22} \text{ cm}^{-2}$ considered in the previous subsection. In the bottom panels, a finite cylinder model with $N_{HI} = 10^{23.3} \text{ cm}^{-2}$ is used with the other conditions the same as in the top panels. We obtain a relatively poor fit of the Monte Carlo simulated profiles to the CFHT spectra. However, the purpose of the current profile comparison is not a detailed profile fit but a simple estimate of the representative neutral column density of the scattering region from the ratio F_{6825}/F_{7082} . From this comparison, it is clear that AG Dra is characterized by a neutral region with N_{HI} an order of magnitude larger than that of HM Sge. We suggest that this is attributed to the closeness of the giant component to the white dwarf in S type symbiotic stars.

Acknowledgements This work was supported by K-GMT Science Program (PID: 14BK002) funded through Korea GMT Project operated by Korea Astronomy and Space Science Institute. This research was also supported by the Korea Astronomy and Space Science Institute under the R&D program (Project No. 2015-1-320-18) supervised by the Ministry of Science, ICT and Future Planning.

References

Schmid, H. M. 1989, A&A, 211, L31

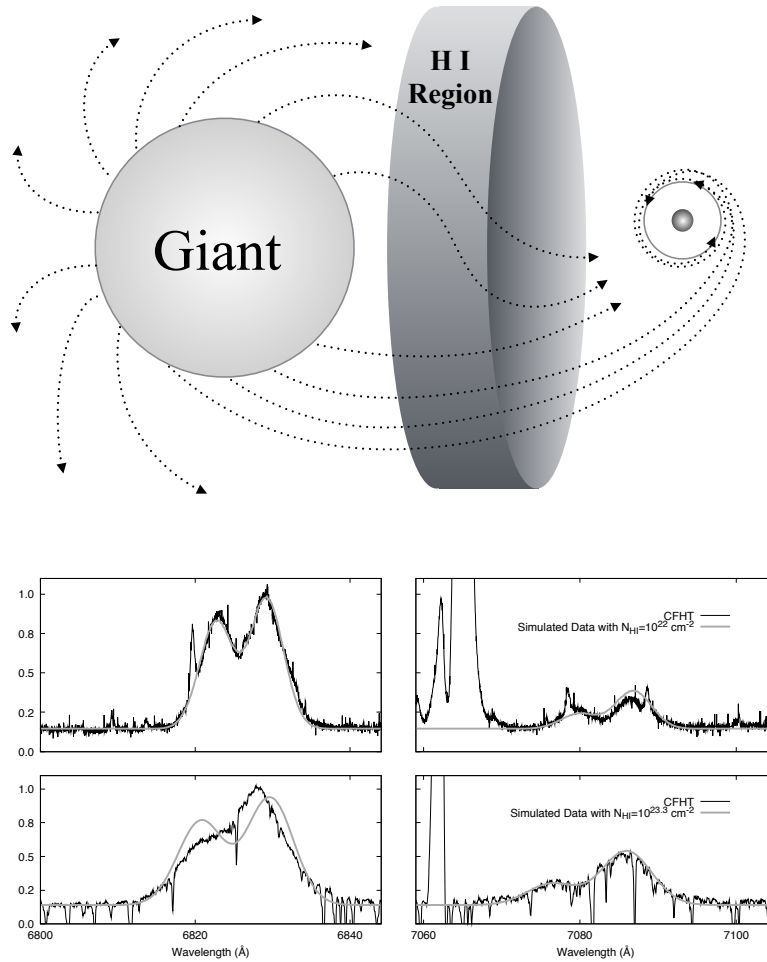


Figure 2: The top panel is a schematic illustration of Raman scattering geometry adopted in this work for a symbiotic star. We adopt a highly simplified neutral region delineated by a finite cylinder with $R/H = 5$ in front of the giant component. The bottom panels are *CFHT* spectra of Raman scattered O VI $\lambda\lambda$ 1032 and 1038 near 6825 Å and 7082 Å of a 'D' type symbiotic star HM Sge (top panels) and an 'S' type symbiotic star AG Dra (bottom panels). Profiles obtained from our Monte Carlo simulations are overlotted to the *CFHT* data.

- Mikołajewska, M., 2012, *Baltic Astronomy*, 21, 5
- Angeloni, R., Contini, M., Ciofi, S., Rafanelli, P., 2010, *MNRAS*, 402, 2075
- Sokoloski, J. L., Bildsten, L., Ho, W. C. G. 2001, *MNRAS*, 326, 553
- Sokoloski, J. L., Bildsten, L., 2010, *ApJ*, 723, 1188
- Whitelock, P. A., 1987, *PASP*, 99, 573
- Lee, H.-W., Kang, S, 2007, *ApJ*, 669, 1156
- Heo, J. -E., Lee, H.-W., 2015, *Journal of the Korean Astronomical Society*, 48, 105

Polarization of far UV Radiation near $\text{Ly}\alpha$ Rayleigh Scattered in Active Galactic Nuclei

Seok-Jun Chang, Hee-Won Lee

Department of Physics and Astronomy, Sejong University
Seoul, Korea

The AGN unification model asserts that all AGNs have both broad and narrow line regions with an optically thick molecular torus outside the broad line region hiding it from view of low latitude observers. Assuming the presence of a high column neutral region in the molecular torus region, we propose that far UV radiation around $\text{Ly}\alpha$ will be significantly polarized through Rayleigh scattering. Adopting a Monte Carlo technique we compute fluxes and degrees of linear polarization of Rayleigh scattered $\text{Ly}\alpha$ in a neutral slab region and a torus region. Due to the enormous range of scattering optical thickness dependent on the wavelength polarization flip may occur as the wavelength varies from the line center to the far wing regions. We conclude that Rayleigh scattering may induce uniquely polarized $\text{Ly}\alpha$ distinguishable from other emission lines, which will shed much light on the unification models of AGNs.

Key Words: active galaxy - radiative transfer - scattering

1 Introduction

The unification model of active galactic nuclei (AGNs) introduces a Compton thick molecular torus outside of the broad line region (BLR) so that the BLR is invisible to observers in the direction of low latitude, unifying the type I and type II AGNs. The presence of the thick molecular torus also provides the tendency of larger X-ray hardness exhibited by type 2 AGNs than type 1 counterparts. Spectropolarimetry of AGNs has shown that polarized broad lines appear in type 2 AGNs, lending strong support to the unification model of AGNs (e.g. Miller & Goodrich 1990).

In the presence of a high column neutral region, broad $\text{Ly}\alpha$ can be Rayleigh scattered by atomic hydrogen to be strongly polarized, which distinguishes $\text{Ly}\alpha$ from other broad metal lines. We may define the Rayleigh scattering band for a neutral slab with N_{HI} by the range of wavelength for which the Rayleigh scattering optical depth exceeds unity. The cross section of Rayleigh scattering near $\text{Ly}\alpha$ is excellently approximated by a Lorentzian function due to the resonance behavior (e.g. Isliker et al. 1989). from which

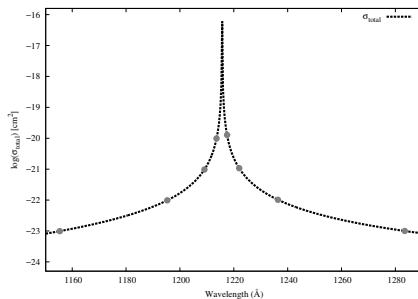


Figure 1: Cross section for Rayleigh scattering by atomic hydrogen. Due to resonance the cross section peaks sharply near Ly α and well approximated by a Lorentzian in the vicinity of the Ly α line center.

the Rayleigh scattering band of Ly α for a neutral slab with N_{HI} is given by

$$\frac{\Delta V}{10^4 \text{ km s}^{-1}} \simeq \left[\frac{N_{HI}}{3 \times 10^{22} \text{ cm}^{-2}} \right]^{1/2}. \quad (1)$$

This relation implies that a neutral region with $\log N_{HI} > 22.5$ will provide sufficiently broad Rayleigh scattering band for a typical broad Ly α of an AGN characterized by a velocity width $\sim 10^4 \text{ km s}^{-1}$ (e.g. Netzer 2015)

2 Monte Carlo Approach

A Monte Carlo technique is adopted to compute the polarization of broad Ly α of an AGN (e.g. Chang et al. 2015, Chang et al. 2017). In this work, the neutral region is approximated by a cylindrical shell and the Ly α emission source is located at the center. The torus or cylindrical shell is characterized by the inner radius R , height H and the H I column density N_{HI} along the lateral direction.

Fig. 3 shows the Monte Carlo results of the flux and polarization of far UV flat continuum near Ly α Rayleigh scattered in a torus with $H/R = 2$ for 2 different values of N_{HI} . The top, middle and bottom panels show the spectra and degree of polarization emerging along the symmetry axis, along the direction making an angle $\theta = \cos^{-1} 0.5$ and along the grazing direction, respectively.

The axial symmetry forces the emergent radiation shown in the top panels to be negligibly polarized. The flux profile exhibits local blue and red maxima. As is seen in the left middle panel, there appears a main central dip due to the blocking of the emission source by the neutral cylindrical shell. However, a close investigation shows that a slight enhancement of Rayleigh scattered flux is found, separating the two flux minima redward and blueward of the line center. The central enhancement is formed through a large number of bouncings on the inner cylinder surface as those photons with huge scattering optical depth τ_s struggle to escape from the region.

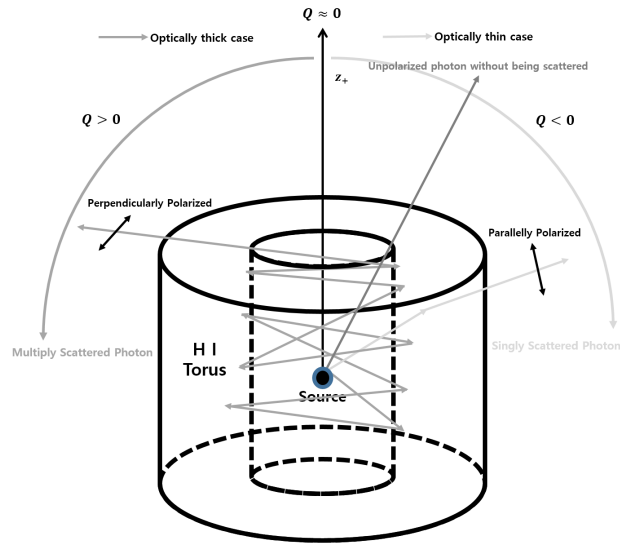


Figure 2: Illustration of polarization development for optically thin and thick cases in the torus model.

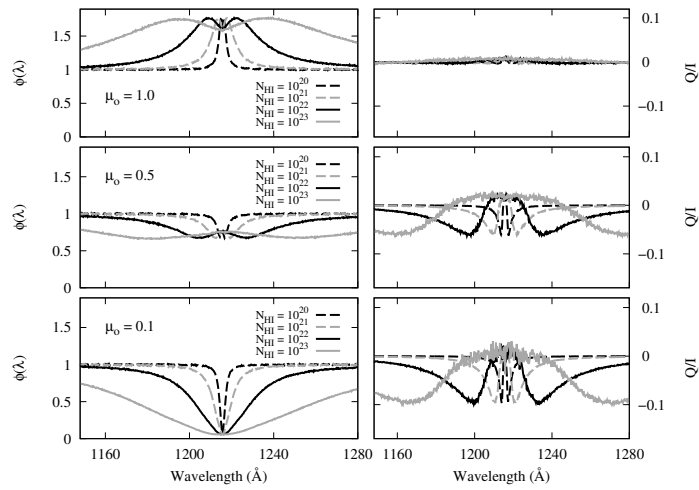


Figure 3: Polarization of Ly α Rayleigh scattered in a neutral cylindrical shell.

The escape process of these photons is analogous to diffusion in physical space in the direction parallel to the cylinder axis. This results in development of linear polarization in the direction perpendicular to the symmetry axis. Chandrasekhar (1960) showed that optically thick photons emergent in a slab geometry can be polarized with a degree of polarization up to 0.117 in the direction perpendicular to the slab normal. However, in the far wing regions, photons are optically thin and escape is made dominantly by single scattering. These optically thin photons are polarized in the direction parallel to the cylinder axis because neutral atoms are distributed equatorially.

In the bottom panels for grazingly emergent radiation, no central enhancement is formed simply because a negligible portion of the upper part of the cylindrical shell is available to the observer. Polarization near the line center is hardly noticeable and only the far wing regions are significant polarized along the symmetry axis.

To sum up, for a neutral torus geometry with $H/R = 2$ polarization near the line center develops in the direction perpendicular to the symmetry axis whereas the wing parts are polarized in the parallel direction. Another interesting possible application of this work can be sought in Ly α emitting objects found in the early universe (e.g. Yang et al. 2010).

Acknowledgements This work was supported by K-GMT Science Program (PID: 14BK002) funded through Korea GMT Project operated by Korea Astronomy and Space Science Institute. This research was also supported by the Korea Astronomy and Space Science Institute under the R&D program (Project No. 2015-1-320-18) supervised by the Ministry of Science, ICT and Future Planning.

References

- Chandrasekhar, 1960, Radiative Transfer (Reading : New York Dover)
- Chang, S.-J., Heo, J.-E., Di Mille, F., Angeloni, R., Palma, T., Lee, H.-W., 2015, ApJ, 814, 98
- Chang, S.-J., Lee, H.-W., Yang, Y., 2017, MNRAS, 464, 5018
- Isliker, H., Nussbaumer, H., Vogel, M., 1989, A&A, 219, 271
- Miller, J. S., Goodrich, R. W., 1993, PASP, 355, 456
- Netzer, H., 2015, ARA&A, 53, 365
- Yang, Y., Zabludoff, A., Eisenstein, D., & Davé, R. 2010, ApJ, 719, 1654

Participant List

	121 Last Name	First Name	Affiliation	E-mail
1	Akras	Stavros	National Observatory of Rio de Janeiro / MCTI, Brazil	stavrosakras@on.br
2	Angeloni	Rodolfo	Universidad de La Serena & Gemini Observatory, Chile	rangeloni@dfuls.cl
3	Barraza	Jermy	Universidad de La Serena , Chile	jermy212121@hotmail.com
4	Berrios	Camila	Universidad de La Serena , Chile	Camii.sxti@gmail.com
5	Chang	Seok-Jun	Sejong University, Korea	csj607@gmail.com
6	Corradi	Romano	GRANTECAN, Spain	romano.corradi@gtc.iac.es
7	Corral-Santana	Jesus	ESO, Chile	jcorral@eso.org
8	Cubillos	Barbara	Universidad de La Serena , Chile	bcubillospalma@gmail.com
9	de Wit	Willem-Jan	ESO, Chile	wdewit@eso.org
10	Di Mille	Francesco	Las Campanas Observatory, Chile	francescodimille@gmail.com
11	Firpo	Verónica	Universidad de La Serena & Gemini Observatory, Chile	vero@dfuls.cl
12	González	Nicolás	Universidad de La Serena , Chile	N.federicorojas@gmail.com
13	Heo	Jeong-Eun	Sejong University, Korea	jeung6145@gmail.com
14	Jeon	Young-Beom	Korea Astronomy and Space Science Institute, Korea	ybjeon@kasi.re.kr
15	Jones	Matias	Pontificia Universidad Católica de Chile, Chile	mjones@aiuc.puc.cl
16	Kim	Hyosun	ASIAA, Taiwan	hkim@asiaa.sinica.edu.tw
17	Kim	Ho-Il	Korea Astronomy and Space Science Institute, Korea	hikim@kasi.re.kr
18	Lee	Hee-Won	Sejong University, Korea	hglee@kasi.re.kr
19	Lee	Young-Min	Sejong University, Korea	hwlee@sejong.ac.kr
20	Lee	Ho-Gyu	Korea Astronomy and Space Science Institute, Korea	ymlee9211@gmail.com
21	Lee	Jae-Joon	Korea Astronomy and Space Science Institute, Korea	lee.j.joon@gmail.com
22	Lovos	Flavia	Observatorio Astronómico de Córdoba	flovos@oac.unc.edu.ar
23	Lucy	Adrian	Columbia University, USA	lucy@astro.columbia.edu
24	Luna	Gerardo Juan Manuel	IAFE/Conicet, Argentina	gmluna@iafe.uba.ar
25	Margheim	Steve	Gemini Observatory, Chile	smargheim@gemini.edu
26	Milla	Fernanda	Universidad de La Serena , Chile	easymphony@gmail.com
27	Miranda Zarate	Josefa	Universidad de La Serena , Chile	Josefamirandazarate@gmail.com
28	Mondal	Santanu	Universidad de Valparaíso, Chile	santanuicsp@gmail.com
29	Muñoz	Nahir	Universidad de La Serena , Chile	nahir@dfuls.cl
30	Nuñez	Natalia	ICATE-UNSJ, Argentina	nnunez@icate-conicet.gob.ar
31	Phillips	Mark	Las Campanas Observatory , Chile	mmp@lco.cl
32	Quiroga	Luis	Universidad de La Serena , Chile	luisquiroga426@gmail.com
33	RODRIGUES	Claudia	Instituto Nacional de Pesquisas Espaciais, Brazil	claudia.rodrigues@inpe.br
34	Roman-Lopes	Alexandre	Universidad de La Serena , Chile	roman@dfuls.cl
35	Roth	Miguel	Giant Magellan Telescope, Chile	mroth@gmto.org
36	Rutten	Rene	Gemini Observatory, Chile	rutten@gemini.edu
37	Saker	Leila Yamila	Observatorio Astronómico de Córdoba, Argentina	leilasaker88@gmail.com
38	Schmidtobreick	Linda	ESO, Chile	lschmidt@eso.org
39	Sekeras	Matej	Slovak Academy of Sciences, Slovakia	msekeras@ta3.sk
40	Shagatova	Natalia	Slovak Academy of Sciences, Slovakia	nshagatova@ta3.sk
41	Skopal	Augustin	Slovak Academy of Sciences, Slovakia	skopal@ta3.sk
42	Soto King	Piera	Universidad de La Serena , Chile	piera@dfuls.cl
43	Tappert	Claus	Universidad de Valparaíso, Chile	claus.tappert@uv.cl
44	Ulloa	Natalie	Universidad de La Serena , Chile	natalie@dfuls.cl
45	Vera	Pablo	Universidad de La Serena , Chile	pablovera.alfaro@gmail.com
46	Vera	Alex	Universidad de La Serena , Chile	alxdniel@gmail.com
47	Wenderoth	Erich	Universidad de La Serena, Chile	ewb@dfuls.cl
48	Silva	Karleyne	Gemini Observatory, Chile	ksilva@gemini.edu







